



DIPLOMARBEIT

Optimal Control of Collective Dynamics in Cavity-QED with an Inhomogeneously Broadened Spin Ensemble

ausgeführt am

Institut für Theoretische Physik
der Technischen Universität Wien

Institute for Theoretical Physics
Vienna University of Technology

unter der Anleitung von

Univ. Ass. Dr. rer. nat. Dmitry Krimer,

und

Univ.-Prof. Dipl.-Ing. Dr. techn. Stefan Rotter

durch

Benedikt Hartl

Czerningasse 14/17

A-1020 Wien

e1026773@student.tuwien.ac.at

May 9, 2016

Datum

Unterschrift

Acknowledgements

I would like to express my profound gratitude to my advisers Prof. Dr. Stefan Rotter and Dr. Dmitry Krimer for giving me the opportunity to work on such an interesting and fascinating topic as cavity quantum electrodynamics. This thesis would not have been possible without their support and all the encouraging discussions during the last year. I would also like to thank Dr. Florian Mintert with whom I had the privilege to collaborate during my thesis. It was a pleasure visiting him and his group in London and I am grateful for the support regarding information-theoretical issues.

Finally, I would like to take the opportunity to express my sincere thanks to my family, my loved ones, my friends and my colleagues for their friendship and for their patience with me. Especially, I would like to thank my father Sigmund Hartl, who died way too soon, and my mother Martha Hartl, who is the bravest and most warm-hearted person I know. Without their support, without their trust and without their love I would have neither been able to achieve a goal like this nor to become the person that I am today.

Kurzfassung

In den letzten Jahrzehnten gab es erhebliche Fortschritte im Bereich verschiedenster Quantentechnologien. Speziell so-genannte hybride Quantensysteme, die von den Vorteilen ihrer verschiedenen Bestandteile profitieren, sind vielversprechende Kandidaten für zukünftige Anwendungen wie Quanteninformationsverarbeitung in Quanten-Computern. Ein sich rasant entwickelndes Forschungsfeld solcher hybrider Quantensysteme basiert auf Resonator-Quantenelektrodynamik. In den letzten Jahren wurde insbesondere die kollektive Wechselwirkung eines Einmoden-Resonators mit einem inhomogen verbreiterten Spinensemble untersucht, das in einem Festkörper eingeschlossen ist. Wenn Resonator und Spinensemble stark miteinander gekoppelt sind, wird Anregungsenergie kohärent zwischen den beiden Bestandteilen ausgetauscht. Dies ist eine der wichtigsten Voraussetzungen für Quanteninformationsprotokolle. Solche Systeme sind daher erfolgsversprechend für potentielle Realisierungen zukünftiger Festkörper-Quantenspeicher. Deren tatsächliche Verwendbarkeit in skalierbaren Quantenschaltkreisen erfordert allerdings vollständige Kontrolle über die dynamische Entwicklung kollektiver Systemvariablen, damit jede Operation in optimierter und robuster Art und Weise ausgeführt werden kann. In dieser Diplomarbeit entwickeln wir eine Theorie zur optimalen Kontrolle der Resonator-Amplitude und des Zustandes des Spinensembles, wobei wir niedrige Anregungsenergien des Systems im Limes des absoluten Temperaturnullpunktes betrachten. Wir verwenden für diesen Zweck schwache Eingangssignale des Resonators, welche aus einigen wenigen Fourier-Moden bestehen und deren Form wir durch die optimale Wahl der Fourier-Koeffizienten bestimmen. Zur Demonstration der Kontrollmöglichkeiten dieser optimierten Pulse über das hybride Quantensystem schlagen wir ein konkretes Protokoll vor, bei dem mittels zweier Schreimpulse zwei verschiedene logische Zustände in das Spinensemble codiert und für eine gewisse Zeit gespeichert werden können. Der Auslesevorgang erfolgt durch einen optimierten Lsepuls der, abhängig vom zuvor präparierten Zustand, zeitlich getrennten Signale der Resonator-Amplitude innerhalb vorher definierter Zeitfenster erzeugt. Außerdem zeigen wir, dass durch Superposition der Schreimpulse kohärente Superpositionen der logischen Zustände erzeugt und ausgelesen werden können und wir untersuchen, in welchem Maße die entsprechenden kollektiven, niederenergetischen Anregungen vor Dekohärenz bewahrt werden können. Zusammengefasst stellen unsere Ergebnisse einen weiteren Schritt in Richtung eines voll-kontrollierbaren Festkörper-Quantenspeichers dar.

Abstract

Quantum technologies have made considerable progress in the past few decades. Particularly promising candidates for future applications, such as quantum computing and quantum information processing, are hybrid-quantum-systems that benefit from the advantages and strengths of their different constituents. A very actively developing research field of hybrid-quantum-systems is based on cavity quantum electrodynamics. Specifically, the collective interaction of a single-mode cavity with an inhomogeneously broadened spin ensemble embedded in a solid state host material has been studied intensively in the past few years. In the strong coupling regime between the cavity and the whole spin ensemble the energy can be coherently transferred between the different constituents, which is one of the key prerequisite for quantum information protocols. These systems thus hold promise for the realization of future solid state quantum memories. However, their practical applicability in scalable quantum circuits requires full control over the dynamical evolution of collective system variables for any operation to be performed in an optimized and robust fashion. In this diploma thesis we develop an optimal control theory for the dynamics of a single-mode cavity strongly coupled with an inhomogeneously broadened spin ensemble in the low excitation limit at zero temperature. Employing functional pulse shaping we search for smooth, weak cavity input signals consisting of only a few Fourier-modes to control the time evolution of the cavity-amplitude and the state of the spin ensemble. To demonstrate the optimal control capability of this system we suggest a specific protocol to encode and store two different logical states in the inhomogeneously broadened spin ensemble by applying optimized writing pulses to the cavity. In order to distinguish between the two respective states in a predefined subsequent time-window, the readout is performed with a single optimized readout pulse with the goal of generating two time-separated responses of the cavity-amplitude, depending on which state has initially been prepared. Moreover, we demonstrate the possibility to create superpositions of the encoded logical states by superimposing the writing signals and we investigate to which degree the corresponding collective low energy excitations can be preserved from decoherence. Our findings mark a further step towards a fully controllable solid-state quantum memory.

Contents

Acknowledgements	i
Kurzfassung	iii
Abstract	v
1 Introduction	1
2 Model	5
2.1 The Driven Tavis-Cummings Model	5
2.1.1 Equations of Motion for the Expectation Values	6
2.1.2 Continuous Limit of Emitter	8
2.1.3 Volterra Integral Solution for the Cavity-Amplitude	8
2.1.4 Specific Physical System	11
2.1.5 Stationary Transmission Analysis	13
2.1.6 Collective Variables and Dephasing	14
3 Methods	19
3.1 Optimal Control with the Volterra Integral Equation	19
3.1.1 Harmonic Control Field	20
3.1.2 Harmonic Expansion of the Cavity-Amplitude	21
3.1.3 The Cavity-Amplitude in Two Subsequent Intervals	23
3.1.4 Optimal Control over the Cavity-Amplitude	25
3.1.5 Penalty Functional for the Pulse Power	28
4 Results	29
4.1 Time-Binned Cavity-Responses	29
4.1.1 Analysis of Time-Binned Cavity-Responses	31
4.1.2 Numerical Solutions of Time-Binned Cavity-Responses	34
4.1.3 Delayed Time-Binned Cavity-Responses	36
4.2 Superposition of Time-Binned Responses	38
4.2.1 Superimposing the Writing-Pulses	38
4.2.2 Restricted Superposition, Encoding a Real-Bit	39
4.2.3 Retrieval of Two Real-Valued Parameters	41

4.3	Enhanced Storage-Time by Cavity Protection	45
4.3.1	Reduced Decoherence by Increasing the Coupling	46
4.3.2	Micro-Second Storage by Spectral Hole-Burning	48
	Summary	51
	Appendices	53
A	Harmonic Expansion of the Cavity-Amplitude	55
A.1	Two Subsequent Intervals	55
B	Derivations of Time-Binned Objective Functionals	57
B.1	Vector Notation of Variational Coefficients	57
B.2	Vector Notation of Functionals	58
B.3	Equal-Time Products of Cavity-Amplitudes	59
B.4	Time-Integrated Products of Cavity-Amplitudes	61
B.5	Numerical Results of Harmonic Coefficients	62
C	Refocusing of Cavity-Amplitudes and Spin-Waves	65
C.1	Concept, Results and Discussion	65
C.2	Functional Analysis in Storage Interval	67
C.3	Functional Analysis in Delayed Readout Interval	69
C.4	Coupling Strength of Individual Spins	70
C.5	Numerical Results of Storage Coefficients	71
	Bibliography	73

Chapter 1

Introduction

The research field of cavity quantum electrodynamics (QED) has its origin in the early 1980s [1]. Since then cavity QED attracted much attention and until now it is an actively developing area of research with many perspectives in future technologies such as quantum computing and quantum information processing [2–4]. For that purpose different quantum-mechanical elements are brought together to form a hybrid-quantum-system; more precisely, single atoms or whole ensembles of emitters are coupled to the quantized electromagnetic field of a cavity [1–3, 5]. Such hybrid-quantum-systems are designed to benefit from the advantages and strengths of their different constituents [3]. Recently the collective interaction between a single-mode cavity and an inhomogeneously broadened spin ensemble embedded in a solid state host material [6–10] moved into the spotlight in this context. Such systems are promising candidates for the realization of a solid-state quantum memory in scalable quantum circuits [2, 4, 11–15]. The cavity is envisioned to play the role of a quantum bus with which the state of the spin ensemble can be controlled by injecting external control pulses into the cavity. The spin ensemble, in turn, is considered to serve as a memory for quantum information [2, 3]. The individual spins, or equivalently emitters, interact with the cavity via electric or magnetic dipole coupling [5]. However, in realistic ensemble-based systems, every individual spin is coupled with a slightly different strength and transition-frequency with the cavity which is due to a non-negligible interaction of the individual emitters with their surrounding environment [16]. Typically, this inhomogeneous broadening is, in fact, the main source of decoherence in ensemble-based systems and is considered to be the bottleneck for their applicability in quantum-computation protocols [8–10, 16, 17]. The absorption and emission of photons by the ensemble is a collective process provided the whole ensemble is confined within a volume, where all constituents experience the same cavity-field [5, 18–20]. The coupling between the cavity mode and the whole ensemble of N emitters is then collectively enhanced by the factor \sqrt{N} [5]. Consequently, for a large enough ensemble the collective coupling can exceed all decoherence processes of the system and the so-called strong coupling regime can be reached [5, 6, 21]. In this strong coupling regime the exchange of energy between the different constituents of the hybrid-quantum-system takes place in the form

of collective Rabi-oscillations [22]: a cavity photon is coherently converted into a collective excitation of the spin ensemble which is then collectively released back to the cavity before being absorbed again [5, 6, 22]. The strong coupling regime has been successfully observed experimentally for the specific physical system of an inhomogeneously broadened ensemble of negatively charged nitrogen-vacancy defects in diamond (NV-centers), magnetically coupled to a superconducting high-Q single-mode microwave transmission-line resonator [6–8, 23, 24]. In this thesis we present numerical results for this specific physical system, which is sketched in Fig. 1.1. We emphasize, however, that the derivations and protocols we discuss here are valid for any inhomogeneously broadened spin ensemble strongly coupled to a single-mode cavity in the limit of zero temperature and in the low excitation regime.

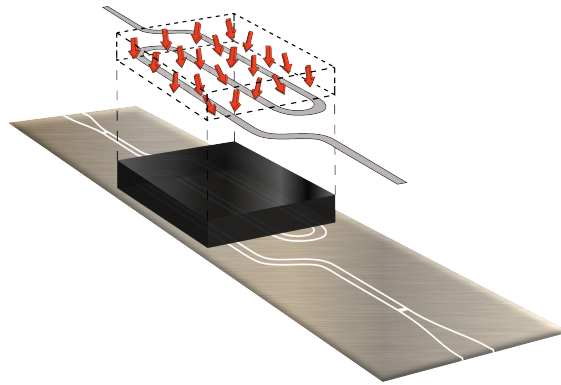


Figure 1.1: Sketch of a high-Q transmission-line resonator (gray line) providing a single cavity mode strongly coupled with an inhomogeneously broadened ensemble of spins (NV-centers, red arrows) embedded in a synthetic diamond (black) [25].

The technological applicability of hybrid-quantum-systems requires full control over the dynamical evolution of collective system variables for any operation to be performed in an optimized and robust fashion [26–28]. An unavoidable prerequisite for a quantum system to be controllable is some kind of communication with an external controllable quantity. Typically such a control is obtained by exposing the hybrid-quantum-system to external control pulses [26]. In cavity-QED these control pulses are simply injected into the cavity and the transmission of the cavity-field is a measure for the physical processes occurring inside the coupled system. Optimal control theories aim to find such control pulses which drive a quantum system towards any desired target state with high accuracy and robustness against experimental perturbations [26–28]. More precisely, optimal control pulses are characterized such that if the transition from an initial state to a desired target state is performed with an optimized pulse, an objective functional obtains an extremum [26–28]. Such an objective functional is typically a quality statement of the transition process like minimal duration, maximal robustness or optimal fidelity [28, 29].

In this thesis we demonstrate how to achieve optimal control over a single-mode cavity strongly coupled to a large, inhomogeneously broadened spin ensemble (in our case $N \approx 10^{12}$) by controlling the evolution of the cavity-amplitude in the low excitation regime [30], a quantity which is experimentally accessible. Specifically, we apply the concept of functional pulse shaping to smooth, weak cavity input-signals which are composed of only a few Fourier modes [28, 29, 31, 32]. In the framework of the semi-classical approach the cavity-amplitude completely characterizes the dynamical evolution of both the cavity-mode and the spin ensemble [23, 24]. Consequently, by controlling the cavity-amplitude of the coupled system we also gain full control over the state of the spin ensemble, which is not directly assessable [33]. The inhomogeneity in the transition-line of the ensemble causes, however, a rather fast dephasing of collective excitations in the spin ensemble. Thus, the main challenge for the optimal control pulses is to excite the spin ensemble in such a way, that the collective emission of photons from an excited ensemble into the cavity is fully controllable.

We further demonstrate the capability of this real-world physical system as a storage device, which we show is very well controllable by smooth-optimal-control pulses. Specifically we suggest a protocol how to write two exclusive states "0" and "1" into the inhomogeneously broadened spin ensemble by injecting weak optimized control pulses into the cavity. Moreover, we show that, depending on which state has initially been prepared, the respective response of the cavity-amplitude to an optimized unique readout pulse (and consequently the transmission through the cavity) can be controlled to be well distinguishable. More precisely, the cavity-responses of state "0" and "1" will be controlled in such a way, that they appear in predefined, well-separable time-bins. Fig. 1.2 depicts a sketch of this protocol.

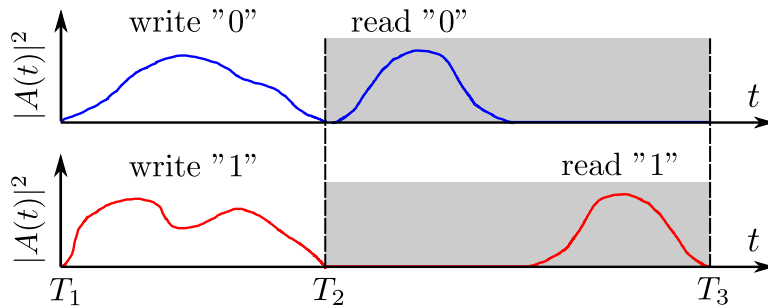


Figure 1.2: Distinguishable, time-binned response of the cavity-amplitude $A(t)$ to a single readout pulse in the time interval $[T_2, T_3]$ (gray region) whether the system was prepared in state "0" or in state "1" in the preliminarily writing interval $[T_1, T_2]$.

The idea of time-binned cavity-responses is very similar to the concept of time-binned quantum-bits (qubits), which have already been shown to be well applicable in quantum-cryptography protocols and quantum-computing [34–39]. However, we avoid the term qubit [40] on purpose, since the time-binned cavity-responses "0"

and "1", which we refer to as logical-states, are solely prepared by optimal control pulses in the semi-classical regime. Nevertheless, the question if our protocol is capable of encoding information into a system, which dynamical evolution is determined by quantum mechanics, seems worth investigating. We therefore address the question how to create coherent superpositions of the two exclusive states "0" and "1" in terms of smooth optimal control pulses. Further we demonstrate that such a superposition can be reconstructed to a very high accuracy solely by measuring the cavity-response in a predefined readout-interval. We also investigate to which degree the concept of smooth optimal control pulses in combination with the cavity protection effect [10, 17, 23–25] can prevent such collective low energy excitations from dephasing. This question is very important since it determines if the information about a superposition of the states "0" and "1" can be stored inside the hybrid-quantum-system before the readout is performed.

To conclude this introduction we want to emphasize that our findings mark a further step towards a fully controllable solid-state quantum memory, applicable in linear quantum networks [2, 3].

Chapter 2

Model

2.1 The Driven Tavis-Cummings Model

The physical system under study consists of a large inhomogeneously broadened ensemble of two level atoms, or equivalently spins, strongly coupled via electric or magnetic dipole coupling to a single-mode cavity with resonance frequency ω_c and a dissipative loss rate κ [6, 41]. Specifically, we will align our choice of parameters with a recent set of experiments [7, 8, 23, 24], which were found to be accurately characterized by these parameters. The individual spins are assumed to be confined within a small volume, where they experience the same cavity field, but at the same time are spatially well separated from each other such that the dipole-dipole interaction between the spins can be neglected. In realistic ensemble-based systems the k^{th} spin is individually coupled to the cavity-mode with a coupling strength g_k and a transition-frequency ω_k , which can be detuned from the mean transition-frequency of the ensemble ω_s [7, 8, 16]. Every individual spin exhibits a dissipative loss rate of γ [41]. The system is schematically presented in Fig. 2.1.

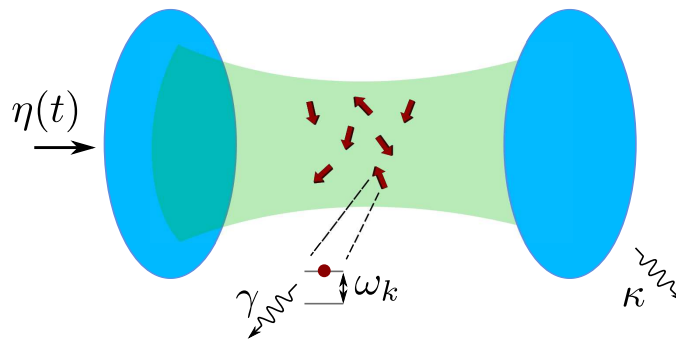


Figure 2.1: Schematics of a cavity (blue mirrors) of resonance frequency ω_c and a loss-rate κ providing a single cavity-mode (light-green) which is coupled to an ensemble of two-level-atoms (red arrows) which obtain an individual transition frequency ω_k and a loss-rate γ . $\eta(t)$ denotes the input-field of the cavity.

It has been shown [8, 10, 20] that such a system can be modeled with the Tavis-Cummings Hamiltonian [42]

$$\mathcal{H} = \omega_c a^\dagger a + \frac{1}{2} \sum_{k=1}^N \omega_k \sigma_k^z + i \sum_{k=1}^N [g_k \sigma_k^- a^\dagger - g_k^* \sigma_k^+ a] - i [\eta(t) a^\dagger e^{-i\omega_p t} - \eta(t)^* a e^{i\omega_p t}] \quad (2.1)$$

where $\hbar = 1$ and the following commutation relations are fulfilled:

$$[a, a^\dagger] = 1, \quad [\sigma_k^+, \sigma_j^-] = \delta_{kj} \sigma_j^z, \quad [\sigma_k^\pm, \sigma_j^z] = \mp \delta_{kj} \sigma_j^\pm. \quad (2.2)$$

The operators a and a^\dagger are the standard creation and annihilation operators of the single cavity-mode with resonance frequency ω_c , respectively. σ_k^z and σ_k^\pm are, respectively, the Pauli- z operator and the Pauli spin-flip operators for the k^{th} spin, which has a transition frequency ω_k and is coupled to the cavity with the coupling strength g_k . The first and the second term in Eq. (2.1) represent the energy of the bare cavity with resonance frequency ω_c and the energy of the N unperturbed spins of the ensemble with mean transition frequency ω_s , respectively. The third term describes the coupling between the cavity and each individual spin within the ensemble: the expression $g_k \sigma_k^- a^\dagger$ converts an excitation of the k^{th} spin into a cavity photon with a rate given by the respective coupling strength g_k , while $g_k^* \sigma_k^+ a$ describes the opposite process. Typically in ensemble-based systems an individual spin is only weakly coupled to the cavity $g_k \ll \kappa, \gamma$ [41]. However, if the whole ensemble interacts collectively with the cavity-mode the effective coupling $\Omega = \sqrt{\sum_{k=1}^N |g_k|^2}$ is collectively enhanced by the factor \sqrt{N} , where N is the number of spins in the ensemble [5, 43]. Provided the ensemble is large enough the collective coupling Ω exceeds all decoherence rates of the system giving rise to the strong coupling regime between the cavity-mode and the inhomogeneously broadened ensemble as a whole [5, 8]. The relevant dynamical processes of the system variables $a(t)$ and $\sigma_k^\pm(t)$ in terms of their expectation values occur at the time-scale $1/\Omega$, where Ω is the aforementioned collective coupling strength [22]. In the strong coupling regime $\Omega \ll \omega_c$ is much smaller than the cavity-resonance frequency [22]. Thus, the Hamiltonian governed by Eq. (2.1) is written in the rotating wave approximation, where fast counter rotating terms $\sigma_k^- a$ and $\sigma_k^+ a^\dagger$ operating at time scales $1/\omega_c \ll 1/\Omega$ are neglected [42]. The last term in Eq. (2.1) specifies the coupling of the cavity-mode a (and a^\dagger) to a classical incoming field with a carrier- or probe-frequency ω_p and an arbitrarily shaped, slowly varying envelope $\eta(t)$ compared to the timescale $1/\omega_p$, which we assume of the same order as $1/\omega_c$ [20].

2.1.1 Equations of Motion for the Expectation Values

Following [8, 24] we start our analysis by deriving the equations of motion for the cavity mode operator $a(t)$, the Pauli-lowering operator $\sigma_k^-(t)$ and the Pauli- z

operator $\sigma_k^z(t)$ in the Heisenberg picture. In general the system under study is an open quantum system and the coupling of the cavity field and the spin ensemble to a thermal environment needs to be taken into account in the description of the system dynamics [20]. At finite temperatures especially thermal photons leak into the cavity and contribute to undesired noise in the system [20]. To correctly describe this situation one would have to derive the corresponding Lindblad master equation [20, 44]. However, we aim to derive the equations of motion for the expectation values of $a(t)$, $\sigma_k^-(t)$ and $\sigma_k^z(t)$ in the semi-classical regime in the limit of zero (or negligible) temperature, where the thermal energy is considered to be much lower than the energy of the unperturbed cavity $k_B T \ll \hbar\omega_c$ [24]. For this purpose it is sufficient to include the dissipative cavity loss-rate κ and individual spin loss-rate γ phenomenologically in the Heisenberg equations of motion [41]

$$\dot{a} = i[\mathcal{H}, a] - \kappa a, \quad \dot{\sigma}_k^- = i[\mathcal{H}, \sigma_k^-] - \gamma \sigma_k^-, \quad \dot{\sigma}_k^z = i[\mathcal{H}, \sigma_k^z], \quad (2.3)$$

where we introduce the short-hand notation $\dot{o}(t) \equiv \frac{do(t)}{dt}$ for the time-derivative for time-dependent quantities $o(t)$. For simplicity we dropped the explicit time dependence of the operators $a(t) \equiv a$, $\sigma_k^-(t) \equiv \sigma_k^-$ and $\sigma_k^z(t) \equiv \sigma_k^z$ in Eq. (2.3). It should be noted that in the case of ensembles of NV-centers, which we consider in this thesis, the spin relaxation time $T_1 \approx 45$ s greatly exceeds current experimental time-scales of 100 ns – 10 μ s and consequently no dissipative term is included in the Heisenberg equation of motion for $\sigma_k^z(t)$ [7]. Inserting the Hamiltonian governed by Eq. (2.1) into Eq. (2.3) and making use of the commutation relations given by Eq. (2.2) yields a set of coupled differential equations for the operators $a(t)$, $\sigma_k^-(t)$ and $\sigma_k^z(t)$. After transforming the cavity-mode operator $a(t) = \tilde{a}(t) e^{-i\omega_p t}$ and the Pauli-lowering operator $\sigma_k^-(t) = \tilde{\sigma}_k^-(t) e^{-i\omega_p t}$ into the frame rotation with the carrier frequency ω_p , we find

$$\dot{\tilde{a}}(t) = -[\kappa + i\Delta_c] \tilde{a}(t) + \sum_{k=1}^N g_k \tilde{\sigma}_k^-(t) - \eta(t), \quad (2.4)$$

$$\dot{\tilde{\sigma}}_k^-(t) = -[\gamma + i\Delta_k] \tilde{\sigma}_k^-(t) + g_k^* \tilde{a}(t) \sigma_k^z(t), \quad (2.5)$$

$$\dot{\sigma}_k^z(t) = -2 [g_k \sigma_k^-(t) a^\dagger(t) + g_k^* \sigma_k^+(t) a(t)], \quad (2.6)$$

where we introduced the detuning factors $\Delta_c = \omega_c - \omega_p$ and $\Delta_k = \omega_k - \omega_p$. Next we treat the problem semi-classically by writing a set of equations for the expectation values of Eq. (2.4), Eq. (2.5) and Eq. (2.6). To keep the number of excitations in the system small compared to the size of the ensemble we only consider weak input fields $\eta(t)$. This restriction allows us to make use of the Holstein-Primakoff approximation $\langle \sigma_k^z(t) \rangle \approx -1$ [30] and directly implies $\dot{\sigma}_k^z(t) = 0$. Further, we assume the correlation function $\langle \tilde{a}(t) \sigma_k^z(t) \rangle$ occurring from Eq. (2.5) to factorize according to $\langle \tilde{a}(t) \sigma_k^z(t) \rangle \approx \langle \tilde{a}(t) \rangle \langle \sigma_k^z(t) \rangle \approx -\langle \tilde{a}(t) \rangle$, where we used $\langle \sigma_k^z(t) \rangle \approx -1$ in the last step. With all these simplifications we arrive at the coupled equations of motion

for the cavity-amplitude $A(t) \equiv \langle \tilde{a}(t) \rangle$ and the amplitude of the k^{th} spin-wave $B_k(t) = \langle \tilde{\sigma}_k^-(t) \rangle$ in the ω_p -rotating frame

$$\dot{A}(t) = -[\kappa + i\Delta_c] A(t) + \sum_{k=1}^N g_k B_k(t) - \eta(t), \quad (2.7)$$

$$\dot{B}_k(t) = -[\gamma + i\Delta_k] B_k(t) - g_k^* A(t). \quad (2.8)$$

Eq. (2.7) and Eq. (2.8) provide a very accurate description of the system dynamics in the low excitation regime [41, 44, 45] for which case a very good agreement between theory and experiment has meanwhile been demonstrated [23, 24].

2.1.2 Continuous Limit of Emitter

The spins of the ensemble exhibit individual transition frequencies ω_k and individual coupling strengths g_k to the single-mode cavity. In the limit of a large number N of emitters we assume the individual spin transition frequencies ω_k to be continuously distributed around the mean transition frequency of the ensemble ω_s . It turns out that such an inhomogeneously broadened transition line of the ensemble can be described by a continuous spectral spin distribution [8]

$$\rho(\omega) = \frac{1}{\Omega^2} \sum_{k=1}^N |g_k|^2 \delta(\omega - \omega_k), \quad (2.9)$$

which is normalized $\int_0^\infty d\omega \rho(\omega) = 1$. The normalization constant $\Omega = \sqrt{\sum_{k=1}^N |g_k|^2}$ denotes the collectively enhanced effective coupling strength. With Eq. (2.9) the transition to the continuous limit of frequencies can be performed for the following class of frequency dependent functions

$$\sum_{k=1}^N |g_k|^2 F(\omega_k) \rightarrow \Omega^2 \int_0^\infty d\omega \rho(\omega) F(\omega). \quad (2.10)$$

The explicit functional profile of $\rho(\omega)$ encounters the frequency dependent coupling g_k of the individual spins, which, in addition to the spectral width of the ensemble, highly affects the system's coherence properties [6, 17]. The derivations in this thesis are not restricted to a particular shape or width of the spectral spin density $\rho(\omega)$, they enter phenomenologically in our formalism.

2.1.3 Volterra Integral Solution for the Cavity-Amplitude

The individual spin-amplitude $B_k(t) = \langle \tilde{\sigma}_k^-(t) \rangle$ can immediately be solved by first transforming Eq. (2.8) into the frame $B_k(t) = \tilde{B}_k(t) e^{-[\gamma + i\Delta_k] \cdot (t - T_1)}$, integrating in

time and transforming back [24]

$$B_k(t) = B_k(T_1) e^{-[\gamma+i\Delta_k]\cdot(t-T_1)} - g_k^* \int_{T_1}^t d\tau A(\tau) e^{-[\gamma+i\Delta_k]\cdot(t-\tau)}, \quad (2.11)$$

where $B_k(T_1)$ denotes the initial conditions for the state of the spin ensemble. Once the cavity-amplitude $A(t)$ is known, the evolution of every individual spin-amplitude in the ensemble is fully determined by Eq. (2.11). To derive the time evolution of the cavity-amplitude $A(t)$ we follow [24] and start with eliminating $B_k(t)$ in Eq. (2.7) by substituting Eq. (2.11). The equation of motion for the cavity-amplitude becomes a linear integro-differential equation and after going to the continuous limit of frequencies with Eq. (2.10) we find

$$\begin{aligned} \dot{A}(t) = & -[\kappa + i\Delta_c] A(t) - \Omega^2 \int_0^\infty d\omega \rho(\omega) \int_{T_1}^t d\tau A(\tau) e^{-[\gamma+i\Delta(\omega)]\cdot(t-\tau)} - \eta(t) \\ & + \sum_k^N g_k B_k(T_1) e^{-[\gamma+i\Delta_k]\cdot(t-T_1)}, \end{aligned} \quad (2.12)$$

where we used the continuous detuning factor $\Delta_k = \omega_k - \omega_p \rightarrow \omega - \omega_p = \Delta(\omega)$. Still following [24] we can solve Eq. (2.12) in terms of a Volterra integral equation, which is separable in different time intervals $[T_n, T_{n+1}]$. In this thesis we will always use the notation of indicating the respective interval $[T_n, T_{n+1}]$ by a superscript (n) in the time dependent quantities, see Fig. 2.2. To solve Eq. (2.12) for an initially completely unexcited spin ensemble $B_k(T_1) = 0$, we first transform into the frame $A(t) = \tilde{A}(t) e^{-[\kappa+i\Delta_c]\cdot(t-T_1)}$, then we integrate in time and finally transform back. After some algebra this procedure yields the solution of the cavity-amplitude $A^{(n)}(t)$, which takes the form of a Volterra integral equation

$$A^{(n)}(t) = \int_{T_n}^t d\tau \mathcal{K}(t-\tau) A^{(n)}(\tau) + \mathcal{D}^{(n)}(t) + \mathcal{F}^{(n)}(t), \quad (2.13)$$

where $A^{(n)}(t)$ depends on all its previous values $A^{(n)}(T_n \leq \tau \leq t)$ [24]. This non-Markovian feedback is established by the kernel function $\mathcal{K}(t-\tau)$

$$\mathcal{K}(t-\tau) = \Omega^2 \int_0^\infty d\omega \rho(\omega) \frac{e^{-[\gamma+i\Delta(\omega)]\cdot(t-\tau)} - e^{-[\kappa+i\Delta_c]\cdot(t-\tau)}}{[\gamma+i\omega] - [\kappa+i\omega_c]}, \quad (2.14)$$

which does only depend on time-differences $t-\tau$ and can thus be efficiently evaluated numerically. The driving term $\mathcal{D}^{(n)}(t)$

$$\mathcal{D}^{(n)}(t) = - \int_{T_n}^t d\tau \eta^{(n)}(\tau) e^{-[\kappa+i\Delta_c]\cdot(t-\tau)}, \quad (2.15)$$

includes an arbitrarily shaped, weak incoming-pulse $\eta^{(n)}(t)$, defined in the time interval $[T_n, T_{n+1}]$. The memory function $\mathcal{F}^{(n)}(t)$

$$\mathcal{F}^{(n)}(t) = \left\{ \begin{aligned} & A^{(n-1)}(T_n) e^{-[\kappa+i\Delta_c]\cdot(t-T_n)} \\ & + \Omega^2 \int_0^\infty d\omega \rho(\omega) \frac{e^{-[\gamma+i\Delta(\omega)]\cdot(t-T_n)} - e^{-[\kappa+i\Delta_c]\cdot(t-T_n)}}{[\gamma+i\omega] - [\kappa+i\omega_c]} \cdot \mathcal{I}^{(n)}(\omega) \end{aligned} \right\} \quad (2.16)$$

takes care of the non-Markovian feedback to the cavity-mode $A^{(n)}(t)$ from the former time interval $[T_{n-1}, T_n]$ with the recursive expression

$$\mathcal{I}^{(n)}(\omega) = \mathcal{I}^{(n-1)}(\omega) e^{-[\gamma+i\Delta(\omega)]\cdot(T_n-T_{n-1})} + \int_{T_{n-1}}^{T_n} d\tau A^{(n-1)}(\tau) e^{-[\gamma+i\Delta(\omega)]\cdot(T_n-\tau)}, \quad (2.17)$$

and the initial conditions $\mathcal{I}^{(0)}(\omega) = \mathcal{I}^{(1)}(\omega) = 0 \leftrightarrow B_k(T_1) = 0$ and $A^{(0)}(t < T_1) = 0$.

As schematically depicted in Fig. 2.2 the cavity-amplitude $A^{(n)}(t)$ of the n^{th} interval can be evaluated solely from the corresponding input pulse $\eta^{(n)}(t)$ and the cavity-amplitude of the previous interval $A^{(n-1)}(t)$. This will allow us to perform numerical calculations for arbitrarily long time-scales while keeping the time-steps small enough. Moreover, the separation of the cavity-amplitude in different time-intervals enables us to treat the dynamical evolution of the cavity-amplitude separately for successive, subsequent input pulses.

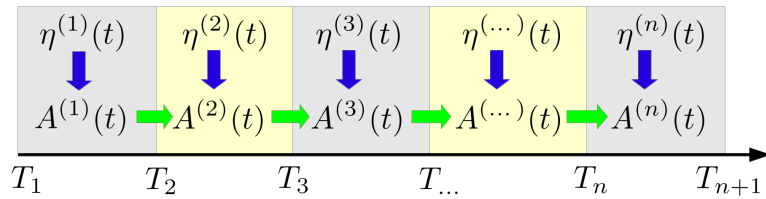


Figure 2.2: Schematics of the time-divisions of the cavity-amplitude $A^{(n)}(t)$ defined by Eq. (2.13). The input field $\eta^{(n)}(t)$ is applied to the system in the time interval $[T_n, T_{n+1}]$ and drives the corresponding cavity-amplitude $A^{(n)}(t)$ (indicated by vertical blue arrows). The non-Markovian feedback from former time intervals $[T_{n-1}, T_n]$ is indicated by horizontal green arrows and enters the formalism via Eq. (2.16).

2.1.4 Specific Physical System

Throughout this thesis we present numerical results considering one specific physical realization based on an inhomogeneously broadened ensemble of negatively charged nitrogen-vacancy defects (NV-centers) in diamond, magnetically coupled to a high-Q superconducting single-mode microwave transmission-line resonator (see Fig. 1.1) [6–8, 23, 24]. However, the derivations and protocols suggested in this thesis are not restricted to this particular choice.

The ground state of an individual NV-center is a spin one triplet ($S = 1$) where the degenerate $m = \pm 1$ states are vacuum shifted from the $m = 0$ state by 2.88 GHz [16, 46]. One of the two $m = \pm 1$ states is Zeeman-tuned into resonance with the cavity resonance frequency ω_c , while the other one is far off-resonance giving rise to a small dispersive contribution only. Therefore, the individual NV-center can effectively be described by a two-level-system coupled to the single-mode cavity [8].

Specifically we consider a microwave cavity with resonance frequency $\omega_c = 2.6915$ GHz and a dissipative damping rate of $\kappa = 2\pi \cdot 0.8$ MHz. The individual dissipative spin loss-rate $\gamma \ll \kappa$ is much smaller than the cavity dissipation so that the effect of spin dissipation can be neglected on the time scales of present experiments $\Delta t \approx 100$ ns – 10 μ s. The coupling strength of an individual NV-center to the single-mode cavity $g_k \approx 2\pi \cdot 12$ Hz $\ll \kappa$ is rather weak but by coupling a large ensemble of $N \approx 10^{12}$ NV-centers to the cavity, the collectively enhanced effective coupling strength $\Omega \approx g \cdot \sqrt{N} \approx 2\pi \cdot 10$ MHz gives rise to the strong coupling regime [8]. In fact, an effective coupling strength of $\Omega = 2\pi \cdot 8.56$ MHz has been achieved in the experiment [7, 8, 23, 24]. However, the transition-line of a whole ensemble of NV-centers is inhomogeneously broadened around the mean transition frequency ω_s because individual spins experience different local environments [7, 8, 16]. This inhomogeneously broadened transition-line, which is the main source of decoherence in ensemble based systems [10, 17, 23], is modeled by a spectral density distribution $\rho(\omega)$ of finite width by Eq. (2.9) [8]. Almost perfect agreement of theory and experiment has been achieved by modeling $\rho(\omega)$ by a q-Gaussian distribution [8, 23, 24]

$$\rho(\omega) = \mathcal{N} \cdot \left[1 - (1 - q) \frac{(\omega - \omega_s)^2}{\Delta^2} \right]^{\frac{1}{(1-q)}}, \quad (2.18)$$

where the factor $q = 1.39$ defines the shape of the distribution, $\gamma_q = 2\Delta \sqrt{\frac{2^q - 2}{2q - 2}}$ is the full width at half maximum and the constant \mathcal{N} ensures the normalization of the spin density distribution. Fig. 2.3 depicts the q-Gaussian spin distribution with a full width at half maximum $\gamma_q = 2\pi \cdot 9.4$ MHz, which we use in this thesis. We further only consider the resonance case $\omega_c = \omega_s = \omega_p$ of the cavity resonance frequency, the ensemble mean frequency and the carrier frequency.

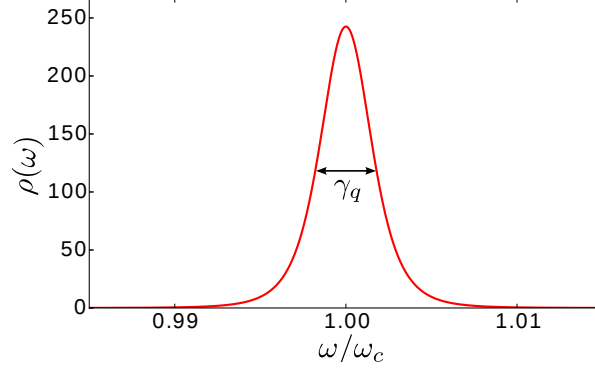


Figure 2.3: The normalized spectral spin distribution $\rho(\omega)$ defined by Eq. (2.9) of an inhomogeneously broadened spin ensemble modeled by a q-Gaussian distribution Eq. (2.18) of full width at half maximum γ_q .

In Fig. 2.4 we show the time-evolution of the cavity-amplitude given by Eq. (2.13) for an initially completely relaxed system $A^{(1)}(0) = 0$ and $B_k^{(1)}(0) = 0$ probed with a constant driving pulse $\eta^{(1)}(t) = \eta_0$ in the interval $[T_1, T_2] = [0 \mu\text{s}, 0.9 \mu\text{s}]$, which is switched off $\eta^{(2)}(t) = 0$ in the subsequently interval $[T_2, T_3] = [0.9 \mu\text{s}, 1.2 \mu\text{s}]$. We consider the parameters from above.

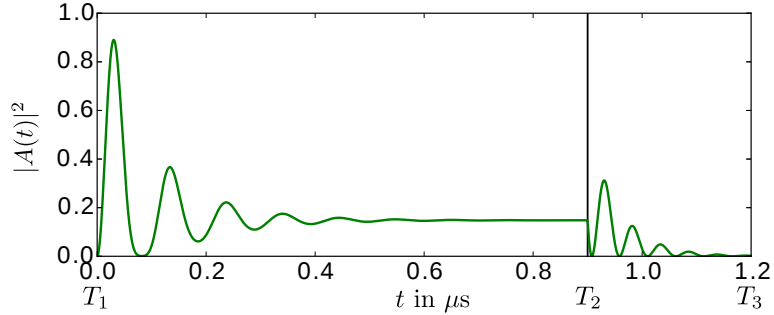


Figure 2.4: The evolution of the cavity-amplitude $A(t)$ (green) defined by Eq. (2.13) in the resonance case $\omega_s = \omega_c = \omega_p$ for an initially completely relaxed system $A(0) = 0$ and $B_k(0) = 0$. The vertical cut separates the first interval $[T_1, T_2] = [0 \mu\text{s}, 0.9 \mu\text{s}]$, where a constant pulse $\eta(t) = \eta_0$ is applied, from the second interval $[T_2, T_3] = [0.9 \mu\text{s}, 1.2 \mu\text{s}]$, where the pulse is switched off.

After an initial oscillatory behavior in the interval $[0 \mu\text{s}, \approx 0.5 \mu\text{s}]$ the cavity-amplitude depicted in Fig. 2.4 settles at a stationary plateau of $|A_{st}^{(1)}(t)|^2 \approx 0.2$. As soon as the driving field is turned off at $T_2 = 0.9 \mu\text{s}$ we observe damped Rabi-oscillations of the cavity-amplitude, where the first peak is larger than the stationary amplitude before the switch off. This overshoot stems from the energy, which

is transferred into the spin ensemble during the interval $[T_1, T_2]$. After the driving field is switched off this energy is collectively released back into the cavity such that the cavity-amplitude obtains a maximum. Subsequently the cavity-photons are reabsorbed again by the ensemble, which is denoted by the successive minimum of the cavity-amplitude. This process repeats itself but without the driving field, the cavity-amplitude in the undriven, second interval $[T_2, T_3]$ experiences a rather fast decay with the decoherence rate $\Gamma \approx 2\pi \cdot 3 \text{ MHz}$, which is mainly caused by the inhomogeneous broadening of the spin ensemble [24].

2.1.5 Stationary Transmission Analysis

When the cavity is driven with a constant pulse $\eta(t) = \eta_0$ for long enough the cavity-amplitude will settle at a stationary value due to simultaneous gain (by the driving pulse) and loss (by different decoherence processes). This steady state solution can be evaluated by setting $\dot{A}(t) = 0$ and $\dot{B}_k(t) = 0$ in Eq. (2.7) and Eq. (2.8), respectively. The stationary cavity-amplitude as a function of the driving field carrier frequency ω_p reads

$$A_{st}(\omega_p) = \frac{i\eta_0}{\omega_c - \omega_p - i\kappa - \Omega^2 \int_0^\infty d\omega \frac{\rho(\omega)}{\omega - \omega_p - i\gamma}}. \quad (2.19)$$

The stationary transmitted probe field $\eta_T(\omega_p) = \kappa A_{st}(\omega_p)$ is directly proportional to the cavity-amplitude [8, 10, 17]. The complex valued transmission function $T(\omega_p) = \eta_T(\omega_p)/\eta_0$, normalized to the input pulse amplitude η_0 , thus takes the form

$$T(\omega_p) = \frac{i\kappa}{\omega_c - \omega_p - i\kappa - \Omega^2 \int_0^\infty d\omega \frac{\rho(\omega)}{\omega - \omega_p - i\gamma}}. \quad (2.20)$$

Fig. 2.5 depicts the stationary transmission through the cavity $T(\omega_p)$ for our spin-cavity system depicted in Fig. 1.1. The transmission spectrum shows two well separated resonance peaks of characteristic width Γ located at $\omega_c \pm \Omega_R$, where Ω_R is the Rabi-frequency of the system. In a simplified picture the cavity-mode and the spin ensemble can be thought of as two resonantly coupled harmonic oscillators of resonance frequencies $\omega_c = \omega_s$ [5, 30]. If there was no coupling $g_k = 0$ between the spins and the cavity, only one peak of width 2κ would be visible at ω_c , that is the bare transmission through the cavity. In the strong coupling regime, however, the eigenstates of the cavity-mode and the inhomogeneously broadened spin ensemble hybridize into so-called polaritonic-states, which obey an avoided crossing of their eigen-energies $\omega_c \pm \Omega_R$ at resonance [22]. The two resonance peaks depicted in Fig. 2.5 exactly resemble this level splitting and are consequently referred to as

polaritonic peaks [7, 8]. The broadening Γ of the resonance peaks denotes the total decoherence rate of the system, which is mainly caused by the spectral width γ_q of the inhomogeneously broadened spin ensemble but also by the cavity losses κ and the individual spin losses γ [8, 10, 17]. Thus, in realistic systems the inhomogeneously broadened transition line of the ensemble affects the ability to reach the strong coupling regime [9, 10, 17, 21]. We can see, however, that in our case the level-splitting exceeds the peaks' broadening giving rise to Rabi-oscillations of the cavity-amplitude of frequency Ω_R which are damped by the decoherence rate Γ as can be seen in Fig. 2.4 after the switch-off of the constant driving field at T_2 [5, 17, 24]. With the current set of parameters we have $\Gamma \approx 2\pi \cdot 3.3$ MHz and $\Omega_R = 2\pi \cdot 9.73$ MHz [24].

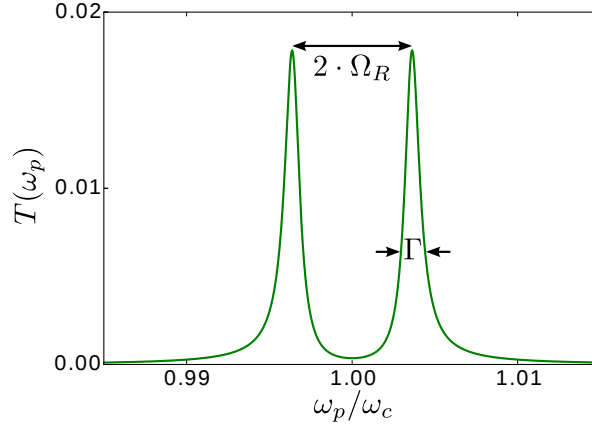


Figure 2.5: Stationary transmission $T(\omega_p)$ defined by Eq. (2.20) of a constant probe field transmitted through a single-mode cavity strongly coupled to an inhomogeneously broadened ensemble of NV-centers. The two resonance peaks are separated by $2 \cdot \Omega_R$, where Ω_R is the Rabi-frequency, and their characteristic width is denoted by Γ . The system-parameters are the same as in Fig. 2.4.

2.1.6 Collective Variables and Dephasing

The cavity-amplitude $A(t)$ described by Eq. (2.13) is a complete description of the dynamical evolution of the system under study in the low excitation regime [23, 24]. Once $A(t)$ is known we can in principle evaluate the evolution of every individual spin-wave amplitude with Eq. (2.11). Assuming an initially fully relaxed spin ensemble $B_k(T_1) = 0$ we find the relation

$$B_k(t) = -g_k^* \int_{T_1}^t d\tau A(\tau) e^{-[\gamma+i\Delta_k] \cdot (t-\tau)}, \quad (2.21)$$

where g_k^* and $\Delta_k = \omega_k - \omega_p$ are the respective individual spin coupling strength and the detuning from the carrier frequency ω_p . The collective counter-parts to the cavity-amplitude $A(t)$ are, however, the collective Dicke-modes defined by $\hat{S}^+ \approx \frac{1}{\Omega} \sum_{k=1}^N g_k^* \sigma_k^+$ and $\hat{S}^- \approx \frac{1}{\Omega} \sum_{k=1}^N g_k \sigma_k^-$ [5, 10, 20, 43]. Following [24] we can evaluate the expectation value of the collective downward ladder operator in the ω_p -rotating frame. For an initially fully relaxed spin ensemble $B_k(T_1) = 0$ we find

$$\begin{aligned} S^-(t) &= \frac{1}{\Omega} \sum_k^N g_k B_k(t), \\ &= -\frac{1}{\Omega} \sum_k^N |g_k|^2 \int_{T_1}^t d\tau A(\tau) e^{-[\gamma+i\Delta_k]\cdot(t-\tau)}, \\ &= -\Omega \int_0^\infty d\omega \rho(\omega) \int_{T_1}^t d\tau A(\tau) e^{-[\gamma+i\Delta(\omega)]\cdot(t-\tau)}, \end{aligned} \quad (2.22)$$

where we first identify $B_k(t) \equiv \langle \tilde{\sigma}_k^-(t) \rangle$, substitute Eq. (2.21) and finally apply the transition to the continuous limit with Eq. (2.10). Within the Holstein-Primakoff approximation $\langle \sigma_k^z \rangle \approx -1$ [30], which we used in our derivations, the collective inversion $S_z = \frac{1}{2} \sum_{k=1}^N \langle \sigma_k^z \rangle \approx -\frac{N}{2}$ is a constant of motion and the collective spin is restricted to the vicinity of the south pole of the Bloch-sphere [43]. For the case of a purely real-valued driving-pulse $\eta(t)$ the cavity-amplitude $A(t)$ is also purely real-valued if the resonance condition $\omega_p = \omega_c = \omega_s$ is satisfied and the spin-distribution $\rho(\omega)$ is symmetrical around ω_s . Consequently, the collective spin-wave amplitude $S^-(t) = S_x(t)$ defined by Eq. (2.22) is purely real, since the imaginary part is an odd function with respect to ω_s and thus cancels by the ω -integration [24]. In Fig. 2.6 we present the collective spin-wave amplitude $S_x(t)$ together with the cavity-amplitude $A(t)$, taken from the reference case Fig. 2.4.

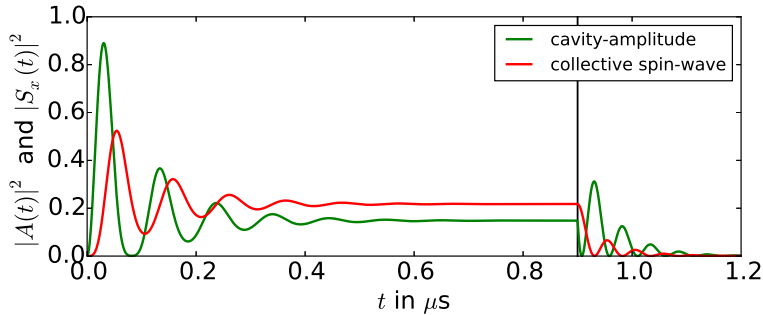


Figure 2.6: The same as Fig. 2.4 except for the additionally presented spin-wave amplitude $S_x(t) = S^-(t)$ (red) defined by Eq. (2.22).

The cavity-amplitude and the collective spin-wave amplitude undergo collective but phase-shifted Rabi-oscillations after the driving field is switched off at $T_2 = 0.9 \mu\text{s}$. The energy is coherently exchanged between the cavity-amplitude and the collective spin-wave amplitude and, moreover, an excitation can solely be present in the cavity (maxima of $A(t)$) or in a collectively excited state of the spin ensemble (maxima of $S_x(t)$). These oscillations illustrate the collective absorption and emission processes of a cavity photon by the ensemble [5, 24]. However, the inhomogeneity in the transition-line of the ensemble causes a rather fast dephasing of the collective quantities $A(t)$ and $S^\pm(t)$. After four to five oscillations, which last for a time-interval of 200 ns, the collective excitations are completely gone.

This dephasing process can be understood by the dynamics of the individual spin-wave amplitudes $B_k(t)$. From Eq. (2.21) we can learn, that every individual spin-amplitude uniformly depends on $A(t)$ but is weighted by its own coupling strength g_k^* and is modulated with its own oscillatory phase $e^{-i\Delta_k \cdot (t-\tau)}$. For the case of the cavity-amplitude $A(t)$ depicted in Fig. 2.4 we present in Fig. 2.7(a) the evolution of every individual spin-wave amplitude $\langle \sigma_k^x(t) \rangle$.

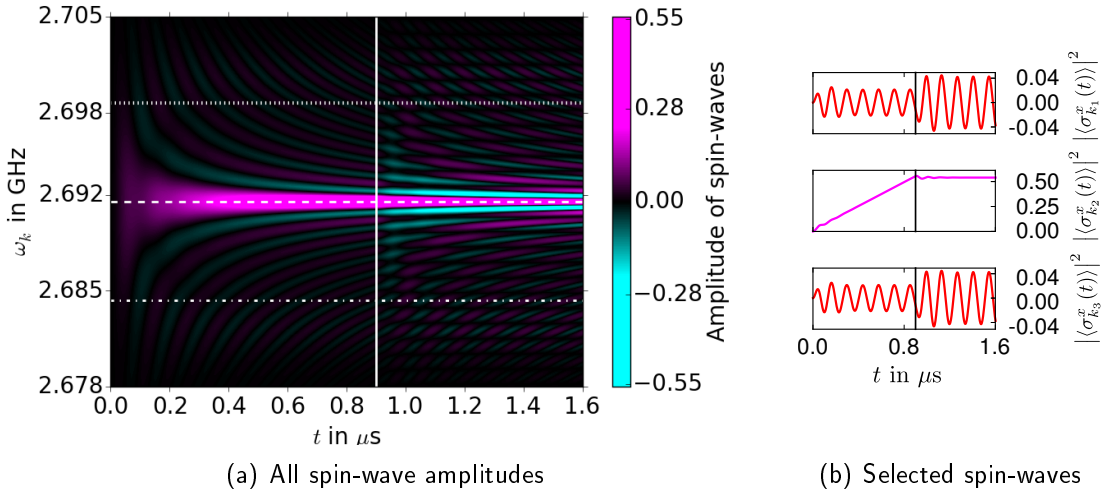


Figure 2.7: (a): The evolution of every individual spin-wave amplitude $\langle \sigma_k^x(t) \rangle = \text{Re}[B_k(t)]$ defined in Eq. (2.21) (surface-color) with transition frequency ω_k (vertical axis) during the time-interval $[0, 1.6 \mu\text{s}]$ (horizontal axis) based on the evolution of the cavity-amplitude $A(t)$ taken from Fig. 2.4. The dotted, dashed and dotted-dashed horizontal cuts correspond to the three selected spin-wave amplitudes depicted in (b) from top to bottom with transition frequencies $\omega_{k_1} \approx 2\pi \cdot 2.7 \text{ GHz}$, $\omega_{k_2} = \omega_c = 2\pi \cdot 2.6915 \text{ GHz}$ and $\omega_{k_3} \approx 2\pi \cdot 2.68 \text{ GHz}$. The vertical cuts denote the end of the constant driving pulse η_0 at $t = 0.9 \mu\text{s}$ in all panels, respectively.

In contrast to the collective quantity $S_x(t) = S^-(t)$, the individual spin-wave amplitudes $B_k(t)$ obtain both, a real-part corresponding to $\langle \sigma_k^x(t) \rangle = \text{Re}[B_k(t)]$ and an imaginary part corresponding to $\langle \sigma_k^y(t) \rangle = -\text{Im}[B_k(t)]$. Fig. 2.7 shows that

the inhomogeneous broadening forces neighboring spins to run out of phase and after the driving field is switched off (after the vertical cut) the collective quantities disappear due to destructive interference. The quasi-continuum of all $N \approx 10^{12}$ inhomogeneously distributed and hence de facto incommensurable transition frequencies $\omega_k \rightarrow \omega$ consequently prevents a rephasing of all the spins (or at least of a significant part of them) and a collective reemission of the stored energy into the cavity will not take place on realistic time-scales. However, even long after the collective quantities have completely vanished, there can still be a huge amount of energy stored inside the spin ensemble as is emphasized in [Fig. 2.7\(b\)](#) for three selected individual spin-wave amplitudes. Remarkably, the system does not lose its energy anymore via the cavity and, as a consequence, the spin-wave excitations are very well preserved from dissipation. In cases where the inhomogeneous broadening can be controlled (which however is not the case for the studied setup with the NV-centers), the dephasing of the spin-wave amplitudes may be reversed, giving rise to controlled revivals of the collective variables $A(t)$ and $S^\pm(t)$. Such a system is also considered to be a promising candidate for the realization of a solid state quantum memory with storage-times limited only by the individual spin loss-rates γ [[4](#), [47](#)].

In this thesis we propose a contrary approach for the realization of a solid state memory device solely based on the coherence properties of the hybrid-quantum-system under study, which we describe linearly by the Volterra integral formalism.

Chapter 3

Methods

3.1 Optimal Control with the Volterra Integral Equation

Coherent control of quantum systems is a very active research field since it paves the way to efficiently make quantum effects available in technological applications [27]. Controllable hybrid-quantum-systems can be used for high precision sensors, are promising candidates for quantum information applications and are used to test the nature of the underlying physics [2–4, 11–15, 29, 34–40, 47–51].

An unavoidable prerequisite for a quantum system to be controllable is some kind of communication with a tunable external quantity [27]. This can be achieved, for instance, by dipole coupling between the electric (or magnetic) dipole operator of a quantum system with a tunable external electric (or magnetic) field [27]. In the case of the driven Tavis-Cummings model [42], which we consider in this thesis, the cavity-mode $a(t)$ can be controlled by the input-field $\eta(t)$, where the interaction is expressed by the term $\eta(t) a^\dagger e^{i\omega_p t} + \eta^*(t) a e^{-i\omega_p t}$ in Eq. (2.1). Further, excitations can be coherently transferred between the cavity-mode and the spin ensemble due to the strong collective coupling between these two quantum systems. This is a key prerequisite for quantum information protocols, which makes these systems very attractive: The cavity plays the role of a quantum bus for the input and output of energy, or information, whereas the ensemble is intended to store the absorbed energy in the form of a collective excitation [11–15].

Optimal control theories enable experimentalists to drive quantum systems into any desired state with high accuracy and robustness against different kinds of perturbations and consequently promote technological advances in the use of quantum systems [26–28]. New technologies, in turn, enable proof of concept experiments for a variety of theories and their results lead to a better understanding of the underlying physical processes, which enables more detailed and sophisticated optimal control schemes. The interplay of scientific research and technological progress in optimal control theory is thus very important [27]. The goal of optimal control theories is to search for control pulses $\eta(t)$ which allow experimentalists to drive controllable quantum systems towards any desired target state in an optimized

and robust fashion [26–28]. More precisely, optimal control pulses are characterized such that if the transition from an initial state to a desired target state is performed with an optimized pulse $\eta_{opt}(t)$, an objective functional $\mathcal{F}[\eta]$ obtains an extremum [26–28]

$$\left. \frac{\delta \mathcal{F}[\eta]}{\delta \eta} \right|_{\eta_{opt}} = 0.$$

Such an objective functional is in general a quality statement of the transition process as for instance minimal duration of the transition, maximal robustness against experimental imperfections or optimal fidelity of the acquired target state [28, 29]. Multiple control pulse in multiple time intervals may contribute to a single functional and multiple constraints may be satisfied simultaneously.

However, considering ensemble-based systems of an enormous size (in our case $N \approx 10^{12}$) existing optimal control procedures reach their limits [27, 32]. Especially the evaluation and the control over the evolution-operator and the full state-vector is difficult to realize [27]. As we will show in the following, the cavity-amplitude $A(t) \equiv \langle a(t) \rangle$ in systems consisting of a single-mode cavity strongly coupled to an inhomogeneously broadened spin ensemble in the low excitation regime can efficiently be controlled by smooth optimal control pulses [28, 29] within the linear Volterra integral framework [23, 24]. Since the cavity-amplitude uniquely determines the evolution of the spin-wave amplitudes of the spin ensemble in this linear regime [23, 24] we consequently achieve control over the entire hybrid-quantum-system under study.

3.1.1 Harmonic Control Field

The capability of optimal control theories is remarkable [26–29, 31, 32]. However, some of the optimal control pulses may obtain a large number of parameters or a complicated structure, which makes it difficult, in addition to possible experimental challenges in the pulse preparation, to determine the essential parts of the pulses [28, 29]. The idea we are putting forward here is to optimally control the time evolution of the cavity-amplitude $A(t)$ with weak cavity input signals $\eta(t)$, which are solely composed of Fourier modes [28, 29, 31, 32]. Despite their analytical functionality such pulses turned out to be very robust against experimental imperfections and, additionally, obtain a simple and smooth shape [28, 29]. Their weak intensities, in turn, have the benefit of resulting in purely linear dynamics of the cavity-amplitude, which can be described with the Volterra integral formalism. This is in contrast to other non-linear control-techniques of spin ensemble-based systems like π -pulses, Hahn-echo or controlled reversible inhomogeneous broadening [4, 33, 39, 47–51].

Since the cavity mode $A^{(n)}(t)$ is defined as a sequential function in time by Eq. (2.13) [23, 24] we can easily construct subsequent control intervals. We especially think of a *writing section* followed by a *readout section*. The superscript

(n) indicates the n^{th} time interval $[T_n, T_{n+1}]$, see Fig. 2.2 for details. With this we define the sequential harmonic optimal control pulses by

$$\eta^{(n)}(t) = \begin{cases} \sum_{k=1}^{N_n} \alpha_k^{(n)} \underbrace{\sin(k \omega_0^{(n)}(t - T_n))}_{\eta_k^{(n)}(t)} & t \in [T_n, T_{n+1}] \\ 0 & \text{otherwise} \end{cases} \quad (3.1)$$

where N_n is the number of harmonic components and $\omega_0^{(n)}$ is the fundamental frequency of the driving field in the n^{th} time interval. The Fourier-coefficients $\alpha_k^{(n)}$ describe the relative amplitude of the k^{th} harmonic component $\eta_k^{(n)}(t)$ of the optimal control pulse, respectively.

It should be noted that, because of the linear regime of the Volterra integral equation, an arbitrarily shaped pulse of the form $\eta^{(n)}(t)$ can be rescaled by a global factor inducing a corresponding rescaling of the cavity-amplitude $A^{(n)}(t)$ [24]. Consequently, all control pulses $\eta^{(n)}(t)$ can be evaluated in arbitrary units and the limit of weak intensities can always be reached by rescaling the solutions afterward.

3.1.2 Harmonic Expansion of the Cavity-Amplitude

The Volterra integral equation Eq. (2.13) in the time interval $[T_1, T_2]$ for an initially empty cavity $A^{(0)}(t \leq T_1) = 0$ and an initially fully unexcited spin ensemble $B_k(t \leq T_1) = 0$ takes the form

$$A^{(1)}(t) = \int_{T_1}^t d\tau \mathcal{K}(t - \tau) A^{(1)}(\tau) + \mathcal{D}^{(1)}(t) \quad (3.2)$$

with the kernel function $\mathcal{K}(t - \tau)$ and the driving term $\mathcal{D}^{(1)}(t)$ given by Eq. (2.14) and Eq. (2.15), respectively. In this section we work out the details of how the harmonic ansatz for the driving field $\eta^{(1)}(t) = \sum_{k=1}^{N_1} \alpha_k^{(1)} \eta_k^{(1)}(t)$ given by Eq. (3.1) affects the description of the cavity-amplitude $A^{(1)}(t)$, if we only consider this single time interval $[T_1, T_2]$. Substituting the harmonic ansatz of the driving field $\eta^{(1)}(t)$ into the driving term $\mathcal{D}^{(1)}(t)$ yields a linear separation in terms of the Fourier coefficients $\alpha_k^{(1)}$

$$\mathcal{D}^{(1)}(t) = \sum_{k=1}^{N_1} \alpha_k^{(1)} d_k^{(1)}(t), \quad (3.3)$$

where the k^{th} component of the driving term $d_k^{(1)}(t)$ is defined similar to Eq. (2.15) but only includes the k^{th} component of the driving field $\eta_k^{(1)}(t)$

$$d_k^{(n)}(t) = - \int_{T_n}^t d\tau \eta_k^{(n)}(\tau) e^{-[\kappa+i\Delta_c]\cdot(t-\tau)}, \quad (3.4)$$

generally presented here for the n^{th} time interval. We then make the ansatz of linearly expanding the cavity-amplitude in terms of the Fourier-coefficients $\alpha_k^{(1)}$

$$A^{(1)}(t) = \sum_{k=1}^{N_1} \alpha_k^{(1)} a_k^{(1)}(t). \quad (3.5)$$

Inserting Eq. (3.3) and Eq. (3.5) into the Volterra integral solution of the cavity-amplitude governed by Eq. (3.2) yields

$$\sum_{k=1}^{N_1} \alpha_k^{(1)} a_k^{(1)}(t) = \int_{T_1}^t d\tau \mathcal{K}(t-\tau) \sum_{k=1}^{N_1} \alpha_k^{(1)} a_k^{(1)}(\tau) + \sum_{k=1}^{N_1} \alpha_k^{(1)} d_k^{(1)}(t), \quad (3.6)$$

which can be rearranged with respect to the coefficients $\alpha_k^{(1)}$

$$0 = \sum_{k=1}^{N_1} \alpha_k^{(1)} \left\{ \int_{T_1}^t d\tau \mathcal{K}(t-\tau) a_k^{(1)}(\tau) + d_k^{(1)}(t) - a_k^{(1)}(t) \right\}. \quad (3.7)$$

Eq. (3.7) has to be satisfied for every (arbitrary) choice of the coefficients $\alpha_k^{(1)}$. This can only be true if the expression in the curly brackets vanishes separately for every k . Hence the k^{th} component of the N_1 cavity-amplitudes $a_k^{(1)}(t)$ must itself be described by the following Volterra integral equation

$$a_k^{(1)}(t) = \int_{T_1}^t d\tau \mathcal{K}(t-\tau) a_k^{(1)}(\tau) + d_k^{(1)}(t), \quad k \in \{1, 2, \dots, N_1\}, \quad (3.8)$$

which, separately for every k , describes the dynamics of an initially empty cavity $a_k^{(1)}(T_1) = 0$ and an initially unexcited spin ensemble, driven only with the k^{th} component $\eta_k^{(1)}(t) = \sin(k\omega_0^{(1)}(t-T_1))$ of the harmonic control field. These N_1 functions $a_k^{(1)}(t)$ can be evaluated for a given time arrangement $[T_1, T_2]$ without specifying the coefficients $\alpha_k^{(1)}$. Consequently, we can evaluate the full time-dependence $a_k^{(1)}(t)$ of the cavity-amplitude $A^{(1)}(t) = \sum_{k=1}^{N_1} \alpha_k^{(1)} a_k^{(1)}(t)$, while the relative weights $\alpha_k^{(1)}$ can be defined later. This provides a very efficient way to functionally evaluate optimal control pulses $\eta^{(1)}(t) = \sum_{k=1}^{N_1} \alpha_k^{(1)} \eta_k^{(1)}(t)$ by simply varying the coefficients $\alpha_k^{(1)}$ in order to establish a certain functional shape of the cavity-amplitude $A^{(1)}(t)$.

3.1.3 The Cavity-Amplitude in Two Subsequent Intervals

Here we study how the previously introduced harmonic ansatz for the cavity-amplitude given by Eq. (3.2) has to be modified, if the cavity is probed with two subsequent optimal control pulses $\eta^{(1)}(t) = \sum_k^{N_1} \alpha_k^{(1)} \eta_k^{(1)}(t)$ and $\eta^{(2)}(t) = \sum_l^{N_2} \alpha_l^{(2)} \eta_l^{(2)}(t)$ defined by Eq. (3.1). We again start from trivial initial conditions $A^{(0)}(t \leq T_1) = 0$ and $B_k(t \leq T_1) = 0$ at the onset of the first time interval $[T_1, T_2]$. The description of the cavity-amplitude $A^{(1)}(t)$ in this section is already given by Eq. (3.5), that is to say by the linearly separable cavity-amplitude $A^{(1)}(t) = \sum_{k=1}^{N_1} \alpha_k^{(1)} a_k^{(1)}(t)$. It is composed of N_1 coefficients $\alpha_k^{(1)}$ and the time-dependent functions $a_k^{(1)}(t)$, which are only defined in the first time interval by Eq. (3.8). Compared to Eq. (3.2) we have to deal with a slightly more complicated form of the Volterra integral equation in the second time interval $[T_2, T_3]$, namely

$$A^{(2)}(t) = \int_{T_2}^t d\tau \mathcal{K}(t - \tau) A^{(2)}(\tau) + \mathcal{D}^{(2)}(t) + \mathcal{F}^{(2)}(t), \quad (3.9)$$

because of the non-Markovian feedback $\mathcal{F}^{(2)}(t)$ from the first to the second time interval defined by Eq. (2.16). With the harmonic pulse $\eta^{(2)}(t) = \sum_{l=1}^{N_2} \alpha_l^{(2)} \eta_l^{(2)}(t)$ the driving term $\mathcal{D}^{(2)}(t) = \sum_{l=1}^{N_2} \alpha_l^{(2)} d_l^{(2)}(t)$ can again be linearly separated in a way similar to Eq. (3.3). However, the correct separation of the memory function $\mathcal{F}^{(2)}(t)$ in terms of the variational coefficients $\alpha_k^{(1)}$ and $\alpha_l^{(2)}$ needs some investigation. The memory function in the second time interval $[T_2, T_3]$ can be evaluated, according to the trivial initial conditions of the first time interval $[T_1, T_2]$, using the recursive relations Eq. (2.16) and Eq. (2.17). We can learn from these relations that $\mathcal{F}^{(2)}(t)$ is linear in the cavity-amplitude of the first time interval $A^{(1)}(t)$. Therefore, we substitute Eq. (3.5) into Eq. (2.16), rearrange the expression with respect to the coefficients $\alpha_k^{(1)}$ and obtain

$$\mathcal{F}^{(2)}(t) = \sum_{k=1}^{N_1} \alpha_k^{(1)} f_k^{(2)}(t), \quad (3.10)$$

where we defined the k^{th} component of the memory function $f_k^{(2)}(t)$ by

$$\begin{aligned} f_k^{(2)}(t) &= \Omega^2 \int_0^\infty d\omega \rho(\omega) \frac{e^{-[\gamma+i\Delta(\omega)] \cdot (t-T_2)} - e^{-[\kappa+i\Delta_c] \cdot (t-T_2)}}{[\gamma+i\omega] - [\kappa+i\omega_c]} \\ &\times \int_{T_1}^{T_2} d\tau a_k^{(1)}(\tau) e^{-[\gamma+i\Delta(\omega)] \cdot (T_2-\tau)} + a_k^{(1)}(T_1) e^{-[\kappa+i\Delta_c] \cdot (t-T_2)}. \end{aligned} \quad (3.11)$$

Eq. (3.11) is linear in the k^{th} component of the cavity-amplitude $a_k^{(1)}(t)$. We therefore need to consider the $N_1 + N_2$ coefficients $\alpha_k^{(1)}$ and $\alpha_l^{(2)}$ of both time intervals for the ansatz of the cavity-amplitude in the second, subsequent time interval $[T_2, T_3]$

$$A^{(2)}(t) = \sum_{k=1}^{N_1} \alpha_k^{(1)} \psi_k^{(2)}(t) + \sum_{l=1}^{N_2} \alpha_l^{(2)} a_l^{(2)}(t), \quad (3.12)$$

where we introduced the corresponding partial cavity-amplitudes $\psi_k^{(2)}(t)$ and $a_l^{(2)}(t)$. These $N_1 + N_2$ functions $\psi_k^{(2)}(t)$ and $a_l^{(2)}(t)$ are defined only in the second time interval and respectively satisfy the following set of Volterra integral equations

$$\psi_k^{(2)}(t) = \int_{T_2}^t d\tau \mathcal{K}(t - \tau) \psi_k^{(2)}(\tau) + f_k^{(2)}(t), \quad k \in \{1, 2, \dots, N_1\}, \quad (3.13)$$

$$a_l^{(2)}(t) = \int_{T_2}^t d\tau \mathcal{K}(t - \tau) a_l^{(2)}(\tau) + d_l^{(2)}(t), \quad l \in \{1, 2, \dots, N_2\}, \quad (3.14)$$

which are derived very similarly to Eq. (3.8) as can be seen in detail in Appendix A.1. The undriven functions $\psi_k^{(2)}(t)$ continue the evolution of the respective k^{th} cavity-amplitude of the former time interval $a_k^{(1)}(t)$ via the memory function $f_k^{(2)}(t)$ defined above by Eq. (3.11). In analogy to Eq. (3.8) the functions $a_l^{(2)}(t)$ describe the dynamics of an initially empty cavity $a_l^{(2)}(t \leq T_2) = 0$ and an initially fully unexcited spin ensemble, driven with the l^{th} component $\eta_l^{(2)}(t)$ of the harmonic driving field $\eta^{(2)}(t)$. The corresponding l^{th} driving term $d_l^{(2)}(t)$ is defined by Eq. (3.4). For fixed time-divisions $[T_1, T_2]$ and $[T_2, T_3]$ we can evaluate all dynamical quantities $a_k^{(1)}(t)$, $\psi_k^{(2)}(t)$ and $a_l^{(2)}(t)$ independently from the coefficients $\alpha_k^{(1)}$ and $\alpha_l^{(2)}$. With this we can efficiently evaluate two subsequent optimal control pulses $\eta^{(1)}(t)$ and $\eta^{(2)}(t)$ by varying the complex valued coefficients for both time intervals simultaneously, such that the cavity-amplitudes $A^{(1)}(t)$ and $A^{(2)}(t)$ satisfy any desired functional behavior. Consequently, the separation approaches Eq. (3.5) and Eq. (3.12) pave the way to control the dynamics of a single-mode cavity strongly coupled to a spin ensemble by manipulating the Fourier-coefficients $\alpha_k^{(1)}$ and $\alpha_l^{(2)}$ of two subsequent harmonic control fields $\eta^{(1)}(t)$ and $\eta^{(2)}(t)$ given by Eq. (3.1). Moreover, we achieve control over the collective spin-wave amplitude $S^-(t)$ defined in Eq. (2.22) and, to a certain degree, over the individual spin-wave amplitudes $B_k(t) \equiv \langle \tilde{\sigma}_k^-(t) \rangle$ given by Eq. (2.11), since their dynamics linearly depend on the cavity-amplitude.

3.1.4 Optimal Control over the Cavity-Amplitude

Above we demonstrate how the structure of the Volterra integral equation describing the cavity-amplitude of the system is modified when control pulses composed of Fourier modes are used. In this section we use this method to present a simple protocol, how the response of the cavity-amplitude to a readout pulse in a second time interval $[T_2, T_3]$ can functionally be controlled, after the cavity was driven with a non-trivial pulse in the first time interval $[T_1, T_2]$. According to Eq. (3.1) we introduce the two subsequent pulses

$$\eta^{(1)}(t) = \sum_{k=1}^{N_1} \alpha_k^{(1)} \sin\left(k \omega_0^{(1)} (t - T_1)\right), \quad (3.15)$$

$$\eta^{(2)}(t) = \sum_{l=1}^{N_2} \alpha_l^{(2)} \sin\left(l \omega_0^{(2)} (t - T_2)\right), \quad (3.16)$$

where $\eta^{(1)}(t)$ and $\eta^{(2)}(t)$ are only defined in their respective intervals (denoted by the superscript (1) and (2)) and are zero elsewhere, respectively. The $N_1 + N_2$ Fourier-coefficients $\alpha_k^{(1)}$ and $\alpha_l^{(2)}$ in the first and second interval will later play the role of variational-coefficients in the optimization procedure. $\omega_0^{(1)}$ and $\omega_0^{(2)}$ are the fundamental frequencies of the two pulses. Because of the linear ansatz Eq. (3.15) and Eq. (3.16) of the driving fields, the cavity-amplitudes in the first and in the second time interval can be written in the form Eq. (3.5) and Eq. (3.12), that is $A^{(1)}(t) = \sum_{k=1}^{N_1} \alpha_k^{(1)} a_k^{(1)}(t)$ and $A^{(2)}(t) = \sum_{k=1}^{N_1} \alpha_k^{(1)} \psi_k^{(2)}(t) + \sum_{l=1}^{N_2} \alpha_l^{(2)} a_l^{(2)}(t)$. We aim to functionally evaluate the best choice of coefficients $\alpha_k^{(1)}$ and $\alpha_l^{(2)}$ such that the cavity-amplitude $|A^{(2)}(t)|^2$ obtains a controlled response during a functional interval $\Delta\tau \equiv [\tau, \tau']$ within the readout section $[T_2, T_3]$. Therefore we introduce the following two objective functionals to be minimized by variations of the control pulses $\eta^{(1)}(t)$ and $\eta^{(2)}(t)$

$$\mathcal{M}_{\mathcal{N}} [\eta^{(1)}, \eta^{(2)}; \tau] = |A^{(2)}(\tau)|^2 - \mathcal{N}, \quad (3.17)$$

$$\mathcal{L}_{\mathcal{A}} [\eta^{(1)}, \eta^{(2)}; \Delta\tau] = \int_{\tau}^{\tau'} dt |A^{(2)}(t)|^2 - \mathcal{A}, \quad (3.18)$$

where we omit the time-dependence of the control pulses in the argument of the objective functionals. Controlling the value of the cavity-amplitude $|A^{(2)}(\tau)|^2 = \mathcal{N}$ with Eq. (3.17) is closely related to controlling the number of photons inside the cavity. If initially a single photon resides in the cavity $|1\rangle$ and, simultaneously, the spin ensemble is in its ground-state $|G\rangle$, this analogy becomes exact $|A(t)|^2 = \langle 1, G | a^\dagger(t) a(t) | 1, G \rangle$ in the case of zero driving [10, 17, 24]. Further, the functional Eq. (3.18) controls the cavity-amplitude during the whole time-interval $\int_{\tau}^{\tau'} dt |A^{(2)}(t)|^2 = \mathcal{A}$.

As a minimal example we define a protocol to completely suppress the cavity-amplitude $A^{(2)}(t)$ in the functional interval $\Delta\tau_0 \equiv [\tau_0, \tau'_0]$, which we define as a subset of the readout section $[T_2, T_3]$, after the cavity was driven with a non-trivial pulse in the first time interval $[T_1, T_2]$. Such a protocol may be used to prevent an excited system from losing photons via the cavity during the interval $\Delta\tau_0$ by coherently feeding back the necessary energy with the pulse $\eta^{(2)}(t)$. For that purpose we use [Eq. \(3.17\)](#) and [Eq. \(3.18\)](#) and set the constants $\mathcal{N} = 0$ and $\mathcal{A} = 0$ to zero. The complete functional to be minimized by a simultaneous variation of the writing and the readout pulse $\eta^{(1)}(t)$ and $\eta^{(2)}(t)$ then takes the form

$$\mathcal{F}_0 [\eta^{(1)}, \eta^{(2)}; \Delta\tau_0] = \int_{\tau_0}^{\tau'_0} dt |A^{(2)}(t)|^2 - \lambda_{\mathcal{T}} |A^{(2)}(\tau_0)|^2. \quad (3.19)$$

The integral objective functional given by [Eq. \(3.18\)](#) plays the role of the functional which is constrained by the penalty function defined by [Eq. \(3.17\)](#) using the method of Lagrange-multiplier $\lambda_{\mathcal{T}}$. The constraint has the purpose of stabilizing the numerical results of the cavity-amplitude at the beginning of the functional interval $|A^{(2)}(\tau_0)|^2 = 0$. We mentioned before that the complete information about the time evolution of the cavity-amplitudes $A^{(1)}(t)$ and $A^{(2)}(t)$ is given by the partial cavity-amplitudes $a_k^{(1)}(t)$, $\psi_k^{(2)}(t)$ and $a_l^{(2)}(t)$ defined by [Eq. \(3.8\)](#), [Eq. \(3.13\)](#) and [Eq. \(3.14\)](#). Moreover, for fixed time-divisions $[T_1, T_2]$ and $[T_2, T_3]$ these functions do not change in the evaluation of $\mathcal{F}_0 [\eta^{(1)}, \eta^{(2)}; \Delta\tau_0]$; they can be evaluated independently of the coefficients $\alpha_k^{(1)}$ and $\alpha_l^{(2)}$ before the optimization procedure has even started. The functional $\mathcal{F}_0 [\eta^{(1)}, \eta^{(2)}; \Delta\tau_0]$ can thus be efficiently minimized simply by varying the $N_1 + N_2$ complex valued coefficients $\alpha_k^{(1)}$ and $\alpha_l^{(2)}$

$$\frac{\delta\mathcal{F}_0 [\eta^{(1)}, \eta^{(2)}; \Delta\tau_0]}{\delta\eta^{(n=1,2)}(t)} \equiv \frac{\delta\mathcal{F}_0 [\eta^{(1)}, \eta^{(2)}; \Delta\tau_0]}{\delta\alpha_k^{(n=1,2)}} \rightarrow 0. \quad (3.20)$$

The optimal set of coefficients $\alpha_k^{(1)}$ and $\alpha_l^{(2)}$ then minimizes $\mathcal{F}_0 [\eta^{(1)}, \eta^{(2)}; \Delta\tau_0]$ and uniquely defines the optimal control pulses $\eta^{(1)}(t)$ and $\eta^{(2)}(t)$ given by [Eq. \(3.15\)](#) and [Eq. \(3.16\)](#).

With the integral functional $\mathcal{L}_{\mathcal{A}} [\eta^{(1)}, \eta^{(2)}; \Delta\tau_0]$ it is easily possible to simultaneously establish a controlled suppression of the cavity-amplitude in the interval $\Delta\tau_0 \equiv [\tau_0, \tau'_0] \subseteq [T_2, T_3]$ followed by a controlled non-zero response to the same reading pulse $\eta^{(2)}(t)$ in a subsequent interval $\Delta\tau_1 \equiv [\tau_1, \tau'_1] \subseteq [T_2, T_3]$. To describe the situation mathematically, the functional $\mathcal{F}_0 [\eta^{(1)}, \eta^{(2)}; \Delta\tau_0]$ has to be extended such that the cavity-amplitude $A^{(2)}(t)$ versus time obtains a certain non-zero area

$\mathcal{A} = \text{const}$ during the interval $\Delta\tau_1$. With this we find

$$\mathcal{F}_{\mathcal{A}} [\eta^{(1)}, \eta^{(2)}; \tau_s, \Delta\tau_0, \Delta\tau_1] = \int_{\tau_0}^{\tau'_0} dt |A^{(2)}(t)|^2 - \lambda_{\mathcal{T}} |A^{(2)}(\tau_s)|^2 - \lambda_{\Delta\mathcal{T}} \left(\int_{\tau_1}^{\tau'_1} dt |A^{(2)}(t)|^2 - \mathcal{A} \right), \quad (3.21)$$

for which we formally introduce the Lagrange-multiplier $\lambda_{\Delta\mathcal{T}}$. This protocol is very important in the following sections about time-binned cavity-responses and thus the situation is presented in detail in [Fig. 3.1](#). Physically such a scheme is possible because of the interference between the cavity-field residing in the system from the preliminarily applied writing pulse $\eta^{(1)}(t)$ and the cavity-field contribution from the subsequent reading pulse $\eta^{(2)}(t)$. Again, the search for the optimal control pulses $\eta^{(1)}(t)$ and $\eta^{(2)}(t)$ is performed by variation of the complex valued coefficients $\alpha_k^{(1)}$ and $\alpha_i^{(2)}$ such that the functional $\mathcal{F}_{\mathcal{A}} [\eta^{(1)}, \eta^{(2)}; \tau_s, \Delta\tau_0, \Delta\tau_1]$ is minimized.

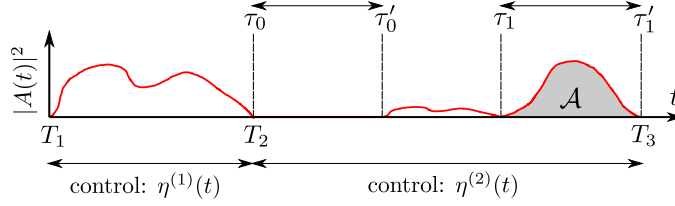


Figure 3.1: Schematics of a functionally suppressed cavity-amplitude $A^{(2)}(t)$ (red) in the time interval $\Delta\tau_0 \equiv [\tau_0, \tau'_0]$ with a simultaneously controlled value \mathcal{A} of the (gray) area of $A^{(2)}(t)$ during the time interval $\Delta\tau_1 \equiv [\tau_1, \tau'_1]$. The goal is to find a combination of optimized control pulses $\eta^{(1)}(t)$ and $\eta^{(2)}(t)$ applied in the time interval $[T_1, T_2]$ and $[T_2, T_3]$, respectively, which minimizes the functional $\mathcal{F}_{\mathcal{A}} [\eta^{(1)}, \eta^{(2)}; \tau_s, \Delta\tau_0, \Delta\tau_1]$ given by [Eq. \(3.21\)](#).

To ensure that the penalty functionals given by [Eq. \(3.17\)](#) and [Eq. \(3.18\)](#) are satisfied after the optimization procedure, the functionals governed by [Eq. \(3.19\)](#) and [Eq. \(3.21\)](#) must exhibit an extremum with respect to variations of the Lagrange-multipliers $\lambda_{\mathcal{T}}$ and $\lambda_{\Delta\mathcal{T}}$. This can formally be written in the following way

$$\frac{\delta\mathcal{F}_0 [\eta^{(1)}, \eta^{(2)}; \Delta\tau_0]}{\lambda_{\mathcal{T}}} \rightarrow 0, \quad \frac{\delta\mathcal{F}_0 [\eta^{(1)}, \eta^{(2)}; \Delta\tau_0]}{\lambda_{\Delta\mathcal{T}}} \rightarrow 0. \quad (3.22)$$

In practice we have used the open-source *python*-library *scipy.optimize* to minimize the constrained functionals $\mathcal{F}_0 [\eta^{(1)}, \eta^{(2)}; \Delta\tau_0]$ and $\mathcal{F}_{\mathcal{A}} [\eta^{(1)}, \eta^{(2)}; \tau_s, \Delta\tau_0, \Delta\tau_1]$. A detailed analytical treatment of the functionals of this section is presented in [Appendix B](#), which also is very instructive for numerically purposes.

3.1.5 Penalty Functional for the Pulse Power

In order to rigorously control the power of the writing and the readout pulse $\eta^{(1)}(t)$ and $\eta^{(2)}(t)$ defined by [Eq. \(3.15\)](#) and [Eq. \(3.16\)](#) to obtain physically meaningful values, we define the average net power per fundamental period $T_0^{(n)} \equiv 2\pi/\omega_0^{(n)}$ as

$$\mathcal{P}^{(n)} = \frac{1}{T_0^{(n)}} \int_0^{T_0^{(n)}} dt |\eta^{(n)}(t)|^2 = \frac{1}{2} \sum_{k=1}^{N_n} |\alpha_k^{(n)}|^2, \quad (3.23)$$

respectively for both time intervals $n = 1$ and $n = 2$, where N_n is the number of coefficients in the n^{th} interval. The sum over the variational coefficients in [Eq. \(3.23\)](#) can be used to define the functionals

$$\mathcal{M}_{\mathcal{P}^{(n)}}[\eta^{(n)}] = \sum_{k=1}^{N_n} |\alpha_k^{(n)}|^2 - 2\mathcal{P}^{(n)} \rightarrow \min, \quad (3.24)$$

$$\mathcal{M}_{\mathcal{U}^{(n)}}[\eta^{(n)}] := \sum_{k=1}^{N_n} |\alpha_k^{(n)}|^2 \leq 2\mathcal{U}^{(n)}. \quad (3.25)$$

Including [Eq. \(3.24\)](#) or [Eq. \(3.25\)](#) in the minimization procedure of the functionals $\mathcal{F}_0[\eta^{(1)}, \eta^{(2)}; \Delta\tau_0]$ and $\mathcal{F}_{\mathcal{A}}[\eta^{(1)}, \eta^{(2)}; \tau_s, \Delta\tau_0, \Delta\tau_1]$ given by [Eq. \(3.19\)](#) and [Eq. \(3.21\)](#) as penalty functions allows us to constrain the power of the pulses $\eta^{(1)}(t)$ and $\eta^{(2)}(t)$ to equal a predefined value of $\mathcal{P}^{(1)}$ and $\mathcal{P}^{(2)}$ or to obtain an upper limit of $\mathcal{U}^{(1)}$ and $\mathcal{U}^{(2)}$, respectively. A very instructive treatment of $\mathcal{M}_{\mathcal{P}^{(n)}}[\eta^{(n)}]$ and $\mathcal{M}_{\mathcal{U}^{(n)}}[\eta^{(n)}]$ is presented in [Appendix B.2](#).

Chapter 4

Results

4.1 Time-Binned Cavity-Responses

In the previous chapter we demonstrate how to achieve optimal control over the amplitude of a single-mode cavity strongly coupled to an inhomogeneously broadened spin ensemble of enormous size by the concept of functional pulse shaping of smooth, low intensity control pulses, which are composed of Fourier modes [28, 29, 31, 32]. Besides being experimentally accessible, the cavity-amplitude also characterizes the dynamical evolution of the spin ensemble in the Volterra integral formalism, which thus is also controllable with our methods [23, 24].

In this part of the thesis we suggest a protocol how to prepare two exclusive (logical) configurations "0" or "1" of the spin ensemble by the use of two different optimal control pulses $\eta_{0^*}^{(1)}(t)$ or $\eta_{1^*}^{(1)}(t)$, respectively. Subsequently, we aim to perform a readout by applying a single optimized readout pulse $\eta_{\mathcal{R}}^{(2)}(t)$, which is the same regardless of the configuration in which the system has been prepared. The superscripts (1) and (2) denote the writing and the readout interval $[T_1, T_2]$ and $[T_2, T_3]$, respectively. The cavity-amplitude is the only quantity, which is accessible

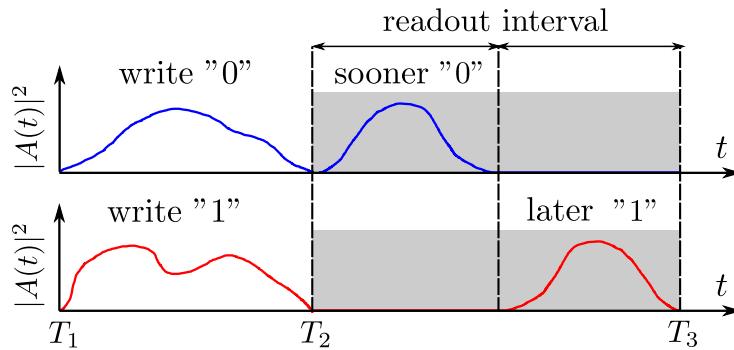


Figure 4.1: Distinguishable sooner "0" (blue, top row) and later "1" (red, bottom row) time-binned responses of the cavity-amplitude $A(t)$ to the readout pulse $\eta_{\mathcal{R}}^{(2)}(t)$ in the time interval $[T_2, T_3]$ (gray region) whether the writing pulse $\eta_{0^*}^{(1)}(t)$ or $\eta_{1^*}^{(1)}(t)$ was applied in the first time interval $[T_1, T_2]$.

in the experiment. We therefore demand for the corresponding state-dependent cavity-amplitudes $A_{„0”}^{(2)}(t)$ and $A_{„1”}^{(2)}(t)$ to be uniquely distinguishable in the readout-section. More precisely, the responses $A_{„0”}^{(2)}(t)$ or $A_{„1”}^{(2)}(t)$ of the cavity-amplitude should appear in a respective *sooner* or in a well-separated *later* time-interval (or time-bin), depending on which state ”0” or ”1” has initially been prepared. The protocol is schematically depicted in Fig. 4.1.

This concept of time-binned cavity-responses is very similar to the idea of time-binned qubits, which has been put forward in [34]. A qubit (quantum-Bit) is a quantum mechanical two-level-system $|\psi\rangle = \alpha |0\rangle + \beta |1\rangle$, which is capable of carrying information about the complex-valued amplitudes α and β with $|\alpha|^2 + |\beta|^2 = 1$ [40]. It is the quantum mechanical generalization of a classical Bit, which can only take one of the two discrete values 0 or 1 [40]. A time-binned qubit is defined as a single photon being de-localized in two well distinguishable time-intervals $|\text{sooner}\rangle$ and $|\text{later}\rangle$ prepared by, for instance, a Mach-Zehnder interferometer as depicted in Fig. 4.2. If the relative amplitude and phase ratio r and ϕ of the time-binned pulses is fully controllable, the state of the photon can be described as a vector in a two-dimensional Hilbert space $|\psi\rangle = r |\text{sooner}\rangle + \sqrt{1 - r^2} e^{i\phi} |\text{later}\rangle$. This is true provided the time-separation between the pulses δt is much larger than the pulse-widths Δt [34]. It should be noted that the time-binned encoding of qubits in telecommunication fiber networks is very robust against decoherence as compared to polarization-encoding. [48, 49]. Further, time-binned qubits are considered to be applicable in linear quantum-computing [38], quantum cryptography and quantum teleportation [48, 49]. It has been demonstrated that the state of time-binned qubits can be stored inside optical materials and retrieved with high fidelity at later times [35, 36, 39].

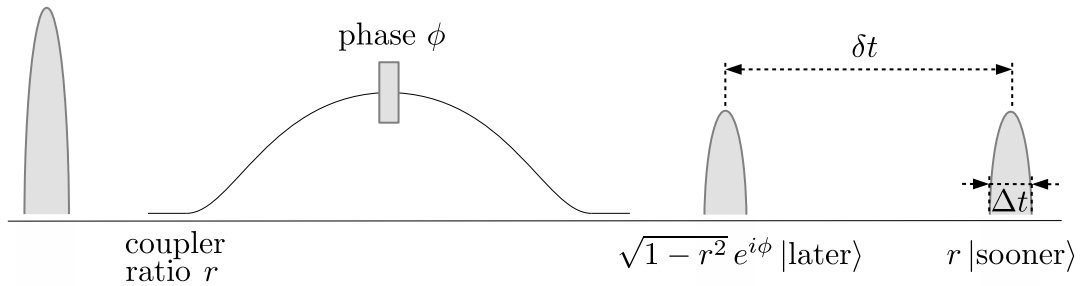


Figure 4.2: A Mach-Zehnder interferometer with a coupling ratio r between the short and the long arm and a phase-shifter ϕ in the long arm for the preparation of a time-binned qubit $|\psi\rangle = r |\text{sooner}\rangle + \sqrt{1 - r^2} e^{i\phi} |\text{later}\rangle$ (right) from a single photon pulse (left). The time-binned pulses (right) are separated by δt and have a width of Δt . The figure is reproduced from [34].

In what follows we demonstrate how to evaluate the optimal control pulses $\eta_{|0\rangle}^{(1)}(t)$, $\eta_{|1\rangle}^{(1)}(t)$ and $\eta_{\mathcal{R}}^{(2)}(t)$ numerically by the methods of [Sec. 3.1.4](#) such that they fulfill the requirements of the time-binned cavity-response protocol described above. We highlight the similarities and the differences between time-binned qubits depicted in [Fig. 4.2](#) and the cavity-responses $A_{|0\rangle}^{(2)}(t)$ and $A_{|1\rangle}^{(2)}(t)$ sketched in [Fig. 4.1](#). For simplicity we equivalently refer to the time-binned cavity-amplitudes $A_{|0\rangle}^{(2)}(t)$ and $A_{|1\rangle}^{(2)}(t)$ as "logical states", "time-binned states" or simply as "states" "0" and "1". However, when speaking of the time-binned states "0" and "1" we simply address the situation if the cavity-response appears in the sooner "0" first half or in the later "1" second half of a predefined functional time-interval, which is denoted by the gray area in [Fig. 4.1](#). This terminology may be a little misleading but we would like to emphasize that the (logical-) states "0" and "1" should neither be confused with quantum states nor are they equivalent to the basis states $|sooner\rangle$ and $|later\rangle$ of a time-binned qubit. It is an open question and is left to further studies to determine if the logical states "0" and "1" follow quantum statistics. However, we demonstrate that our protocol is indeed capable of encoding information into the coupled system by superimposing the two writing pulses $\eta_{|0\rangle}^{(1)}(t)$ and $\eta_{|1\rangle}^{(1)}(t)$. Moreover, we investigate, to which degree this information can be retrieved by solely evaluating the corresponding cavity-responses in the entire functional interval, even if this functional interval is significantly delayed from the end of the writing interval.

4.1.1 Analysis of Time-Binned Cavity-Responses

The two writing pulses $\eta_{|0\rangle}^{(1)}(t)$ and $\eta_{|1\rangle}^{(1)}(t)$, which are injected into the cavity in the writing interval $[T_1, T_2]$ to prepare the system either in the state "0" or "1" are defined by

$$\eta_{|0\rangle}^{(1)}(t) = \sum_{k=1}^{N_1} \alpha_k^{''0''} \sin\left(k \omega_0^{(1)} (t - T_1)\right), \quad (4.1)$$

$$\eta_{|1\rangle}^{(1)}(t) = \sum_{k=1}^{N_1} \alpha_k^{''1''} \sin\left(k \omega_0^{(1)} (t - T_1)\right), \quad (4.2)$$

in analogy to [Eq. \(3.15\)](#), respectively. The $2 \cdot N_1$ harmonic coefficients $\alpha_k^{''0''}$ and $\alpha_k^{''1''}$ correspond to the coefficients $\alpha_k^{(1)}$ of the writing pulse [Eq. \(3.15\)](#) and $\omega_0^{(1)}$ is the fundamental frequency of the pulses. The respective cavity-amplitudes in the

writing interval can be separated into harmonic components according to Eq. (3.5)

$$A_{\text{"0"}}^{(1)}(t) = \sum_{k=1}^{N_1} \alpha_k^{\text{"0"}} a_k^{(1)}(t), \quad (4.3)$$

$$A_{\text{"1"}}^{(1)}(t) = \sum_{k=1}^{N_1} \alpha_k^{\text{"1"}} a_k^{(1)}(t), \quad (4.4)$$

where the coefficients $\alpha_k^{\text{"0"}}$ and $\alpha_k^{\text{"1"}}$ are the same as for $\eta_{\text{"0"}}^{(1)}(t)$ and $\eta_{\text{"1"}}^{(1)}(t)$, respectively. The N_1 time dependent functions $a_k^{(1)}(t)$ are the same for both cavity-amplitudes $A_{\text{"0"}}^{(1)}(t)$ and $A_{\text{"1"}}^{(1)}(t)$ and are determined by Eq. (3.8) independently of the variational coefficients $\alpha_k^{\text{"0"}}$ and $\alpha_k^{\text{"1"}}$. The subsequent unique readout pulse

$$\eta_{\mathcal{R}}^{(2)}(t) = \sum_{l=1}^{N_2} \alpha_l^{\mathcal{R}} \sin\left(l\omega_0^{(2)}(t - T_2)\right) \quad (4.5)$$

is defined in analogy to Eq. (3.16) and is applied in the readout interval $[T_2, T_3]$. The N_2 coefficients $\alpha_l^{\mathcal{R}}$ correspond to the harmonic coefficients $\alpha_l^{(2)}$ of the readout pulse governed by Eq. (3.16) and $\omega_0^{(2)}$ is the fundamental frequency. Because of the linear ansatz of the control pulses the cavity-amplitudes in the second time interval can be written in the form Eq. (3.12), that is

$$A_{\text{"0"}}^{(2)}(t) = \underbrace{\sum_{l=0}^{N_1} \alpha_l^{\text{"0"}} \cdot \psi_l^{(2)}(t)}_{\tilde{A}_{\text{"0"}}^{(2)}(t)} + \underbrace{\sum_{k=0}^{N_2} \alpha_k^{\mathcal{R}} \cdot a_k^{(2)}(t)}_{\tilde{A}_{\mathcal{R}}^{(2)}(t)}, \quad (4.6)$$

$$A_{\text{"1"}}^{(2)}(t) = \underbrace{\sum_{l=0}^{N_1} \alpha_l^{\text{"1"}} \cdot \psi_l^{(2)}(t)}_{\tilde{A}_{\text{"1"}}^{(2)}(t)} + \underbrace{\sum_{k=0}^{N_2} \alpha_k^{\mathcal{R}} \cdot a_k^{(2)}(t)}_{\tilde{A}_{\mathcal{R}}^{(2)}(t)}. \quad (4.7)$$

The $N_1 + N_2$ time dependent functions $\psi_k^{(2)}(t)$ and $a_k^{(2)}(t)$ are defined by Eq. (3.13) and Eq. (3.14), again, independently of the variational coefficients $\alpha_k^{\text{"0"}}$, $\alpha_k^{\text{"1"}}$ and $\alpha_l^{\mathcal{R}}$. The partial amplitudes $\tilde{A}_{\text{"0"}}^{(2)}(t)$ and $\tilde{A}_{\text{"1"}}^{(2)}(t)$ contain the information about which state "0" and "1" has been prepared in the writing interval $[T_1, T_2]$, whereas the readout pulse of the second interval $[T_2, T_3]$ gives rise to the partial readout amplitude $\tilde{A}_{\mathcal{R}}^{(2)}(t)$, which is the same for $A_{\text{"0"}}^{(2)}(t)$ and $A_{\text{"1"}}^{(2)}(t)$.

We now define the functional time-interval $\Delta T_{\mathcal{F}} \equiv [T_{\mathcal{F}}, T'_{\mathcal{F}}]$, which may also be a subset of the entire readout interval $\Delta T_{\mathcal{F}} \subseteq [T_2, T_3]$. The cavity-amplitudes $A_{\text{"0"}}^{(2)}(t)$ and $A_{\text{"1"}}^{(2)}(t)$ of the states "0" and "1" have to be uniquely separable in exactly this functional interval in terms of time-binned cavity-responses. Therefore we define

the corresponding *sooner* time-bin by the first half $\Delta\tau_0$ and the *later* time-bin by the second half $\Delta\tau_1$ of the functional interval $[T_{\mathcal{F}}, T'_{\mathcal{F}}]$, respectively. A detailed sketch of all relevant time-divisions is presented in Fig. 4.3.

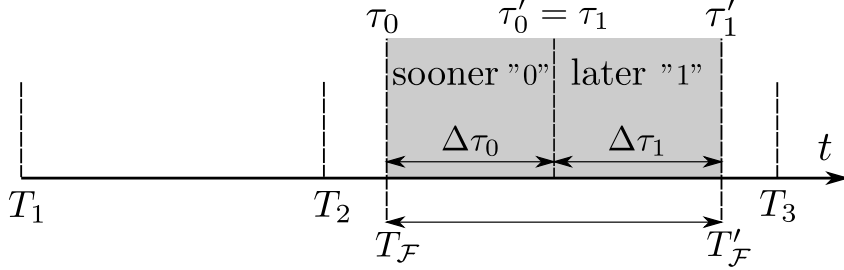


Figure 4.3: Time-divisions of the optimization scheme for the time-binned cavity-responses sketched in Fig. 4.1. The writing interval $[T_1, T_2]$ is followed by the readout interval $[T_2, T_3]$ which contains the functional interval $[T_{\mathcal{F}}, T'_{\mathcal{F}}]$ (gray area). The first half $\Delta\tau_0 \equiv [\tau_0, \tau'_0]$ and the second half $\Delta\tau_1 \equiv [\tau_1, \tau'_1]$ of the functional interval define the *sooner* and the *later* time-bin of the states "0" and "1", respectively.

It should be noted that this definition of the functional interval allows to implement a storage protocol for the states "0" and "1" simply by delaying the functional interval (and consequently the time-binned cavity-responses) from the end of the writing interval $T_2 < T_{\mathcal{F}}$.

In order to meet the time-binned behavior, we demand for the cavity-amplitudes $A_{|0\rangle}^{(2)}(t)$ and $A_{|1\rangle}^{(2)}(t)$ to obtain a controllable, finite value during their corresponding time-interval $\Delta\tau_0$ and $\Delta\tau_1$ while being fully suppressed in the other time-bin $\Delta\tau_1$ and $\Delta\tau_0$, respectively. Consequently, $A_{|0\rangle}^{(2)}(t)$ and $A_{|1\rangle}^{(2)}(t)$ are well separated and, moreover, orthogonal functions in the functional interval $\Delta T_{\mathcal{F}}$ if they exhibit this property. To evaluate the optimal control pulses $\eta_{|0\rangle}^{(1)}(t)$, $\eta_{|1\rangle}^{(1)}(t)$ and $\eta_{\mathcal{R}}^{(2)}(t)$, which cause the desired time-evolution of the cavity-amplitudes $A_{|0\rangle}^{(2)}(t)$ and $A_{|1\rangle}^{(2)}(t)$ when being applied to the cavity, we can directly use Eq. (3.21) for our purposes. In fact, the functional $\mathcal{F}_{\mathcal{A}}[\eta_{|1\rangle}^{(1)}, \eta_{\mathcal{R}}^{(2)}; T_{\mathcal{F}}, \Delta\tau_0, \Delta\tau_1]$ defined by Eq. (3.21) exactly corresponds to the desired behavior of $A_{|1\rangle}^{(2)}(t)$ using the time-divisions sketched in Fig. 4.3 (compare Fig. 3.1 with the bottom row of Fig. 4.1). The cavity-amplitude $A_{|0\rangle}^{(2)}(t)$ should show a finite response in the first interval $\Delta\tau_0$ followed by a completely suppressed response in the interval $\Delta\tau_1$. This situation can also be described by Eq. (3.21), more precisely by $\mathcal{F}_{\mathcal{A}}[\eta_{|0\rangle}^{(1)}, \eta_{\mathcal{R}}^{(2)}; T_{\mathcal{F}}, \Delta\tau_1, \Delta\tau_0]$, where we simply exchanged the time-intervals $\Delta\tau_0 \leftrightarrow \Delta\tau_1$. It should be noted that both cavity-amplitudes $A_{|1\rangle}^{(2)}(T_{\mathcal{F}}) = 0$ and $A_{|1\rangle}^{(2)}(T_{\mathcal{F}}) = 0$ are forced to be zero at the beginning of the functional interval $T_{\mathcal{F}}$ with the implicit usage of Eq. (3.17) in Eq. (3.21). This, in turn, implies that the entire information about the state of the system "0" or "1" is encoded in the spin ensemble at $t = T_{\mathcal{F}}$. Because of the common readout pulse $\eta_{\mathcal{R}}^{(2)}$ the two writing pulses $\eta_{|0\rangle}^{(1)}(t)$ and $\eta_{|1\rangle}^{(1)}(t)$ will not be independent of each other. Therefore we

minimize the combined constrained functional

$$\begin{aligned} \mathcal{F}_A^{0,1} \left[\eta_{0''}^{(1)}, \eta_{1''}^{(1)}, \eta_{\mathcal{R}}^{(2)}; \Delta T_{\mathcal{F}} \right] &= \mathcal{F}_A[\eta_{0''}^{(1)}, \eta_{\mathcal{R}}^{(2)}; T_{\mathcal{F}}, \Delta\tau_1, \Delta\tau_0] \\ &+ \mathcal{F}_A[\eta_{1''}^{(1)}, \eta_{\mathcal{R}}^{(2)}; T_{\mathcal{F}}, \Delta\tau_0, \Delta\tau_1], \end{aligned} \quad (4.8)$$

by a simultaneous variation of all three control pulses. In reality the power $\mathcal{P}^{(1)}$ and $\mathcal{P}^{(2)}$ of the control pulses $\eta_{0''}^{(1)}(t)$, $\eta_{1''}^{(1)}(t)$ and $\eta_{\mathcal{R}}^{(2)}(t)$ has to be finite. Consequently, we have to introduce constraints to ensure this physically motivated requirement and following [Sec. 3.1.5](#) we constrain $\mathcal{F}_A^{0,1}[\eta_{0''}^{(1)}, \eta_{1''}^{(1)}, \eta_{\mathcal{R}}^{(2)}; \Delta T_{\mathcal{F}}]$ with the following two penalty functionals

$$\mathcal{M}_{\mathcal{P}^{(1)}} \left[\eta_{i''}^{(1)} \right] = \sum_{k=1}^{N_1} |\alpha_k^{i''}|^2 - 2\mathcal{P}^{(1)}, \quad (4.9)$$

$$\mathcal{M}_{\mathcal{P}^{(2)}} \left[\eta_{\mathcal{R}}^{(2)} \right] = \sum_{l=1}^{N_2} |\alpha_l^{\mathcal{R}}|^2 - 2\mathcal{P}^{(2)}, \quad (4.10)$$

for $i'' = 0'', 1''$. The task of finding the optimal writing and reading pulses $\eta_{0''}^{(1)}(t)$, $\eta_{1''}^{(1)}(t)$ and $\eta_{\mathcal{R}}^{(2)}(t)$ for this protocol is to find the best set of $2 \cdot N_1 + N_2$ complex valued harmonic coefficients $\alpha_k^{0''}$, $\alpha_k^{1''}$ and $\alpha_l^{\mathcal{R}}$ which minimize the functional $\mathcal{F}_A^{0,1}[\eta_{0''}^{(1)}, \eta_{1''}^{(1)}, \eta_{\mathcal{R}}^{(2)}; \Delta T_{\mathcal{F}}]$ under the constraints $\mathcal{M}_{\mathcal{P}^{(1)}}[\eta_{0''}^{(1)}]$, $\mathcal{M}_{\mathcal{P}^{(1)}}[\eta_{1''}^{(1)}]$ and $\mathcal{M}_{\mathcal{P}^{(2)}}[\eta_{\mathcal{R}}^{(2)}]$. The complete constrained functional can be evaluated and minimized very efficiently with the methods presented in [Appendix B](#). In practice the minimization was performed by numerical variation of the harmonic coefficients by using the *python* library *scipy.optimize*.

4.1.2 Numerical Solutions of Time-Binned Cavity-Responses

In this section we present numerical results for the optimal control pulses $\eta_{0''}^{(1)}(t)$, $\eta_{1''}^{(1)}(t)$ and $\eta_{\mathcal{R}}^{(2)}(t)$, given by [Eq. \(4.1\)](#), [Eq. \(4.2\)](#) and [Eq. \(4.5\)](#), and the corresponding time-binned cavity-amplitudes $A_{0''}^{(n)}(t)$ and $A_{1''}^{(n)}(t)$, given by [Eq. \(4.3\)](#) and [Eq. \(4.4\)](#) in the writing region $n = 1$ and by [Eq. \(4.6\)](#) and [Eq. \(4.7\)](#) in the readout region $n = 2$. The optimized coefficients $\alpha_k^{0''}$, $\alpha_k^{1''}$ and $\alpha_l^{\mathcal{R}}$ for all numerically evaluated writing and readout pulses in the document are listed in [Tbl. B.1](#) and [Tbl. B.2](#). From here on we use the system-parameters which are listed in [Sec. 2.1.4](#) with the collective coupling strength $\Omega = 8.56$ MHz (as used in [Fig. 2.4](#)). The natural frequency of the system under study is the Rabi-frequency $\Omega_R = 2\pi \cdot 9.73$ MHz with a period of $T_R = 2\pi/\Omega_R \approx 102.8$ ns [[23](#), [24](#)]. In [Fig. 4.4](#) we chose the length of the writing sequence to be half a Rabi-period $[T_1, T_2] = [0, T_R/2] \approx [0, 51.4$ ns] and we present the numerical results for two different time-divisions of the subsequent reading section, that is half a Rabi-period $[T_2, T_3] = [T_R/2, T_R] \approx [51.4$ ns, 102.8 ns] in [Fig. 4.4\(a\)](#) and a full

Rabi-period $[T_2, T_3] = [T_R/2, 3 \cdot T_R/2] \approx [51.4 \text{ ns}, 154.2 \text{ ns}]$ in Fig. 4.4(b). Here the functional interval and the readout section coincide $[T_{\mathcal{F}}, T'_{\mathcal{F}}] = [T_2, T_3]$, respectively. In both cases one indeed observes a sooner cavity-response $A_{n,0}^{(2)}(t)$ which is well separated from the later one $A_{n,1}^{(2)}(t)$. In Fig. 4.4(a) the contribution of state "1" in the first half (and of state "0" in the second half) of the functional interval $[T_{\mathcal{F}}, T'_{\mathcal{F}}]$ is almost completely suppressed except for the small overlap at the center $(T_{\mathcal{F}} + T'_{\mathcal{F}})/2 \approx 77.1 \text{ ns}$. For the longer functional interval depicted in Fig. 4.4(b) we find a small but finite amplitude of state "0" in the second half of $[T_{\mathcal{F}}, T'_{\mathcal{F}}]$, which is caused by decoherence effects in the readout section. It should be noted that this longer functional interval already significantly exceeds the decoherence time of the system $1/\Gamma \approx 50 \text{ ns}$ [23, 24] but still the results look very good. In fact, the time-binned separation of the respective cavity-amplitudes seems best pronounced for this larger functional interval depicted in Fig. 4.4(b) as compared to Fig. 4.4(a).

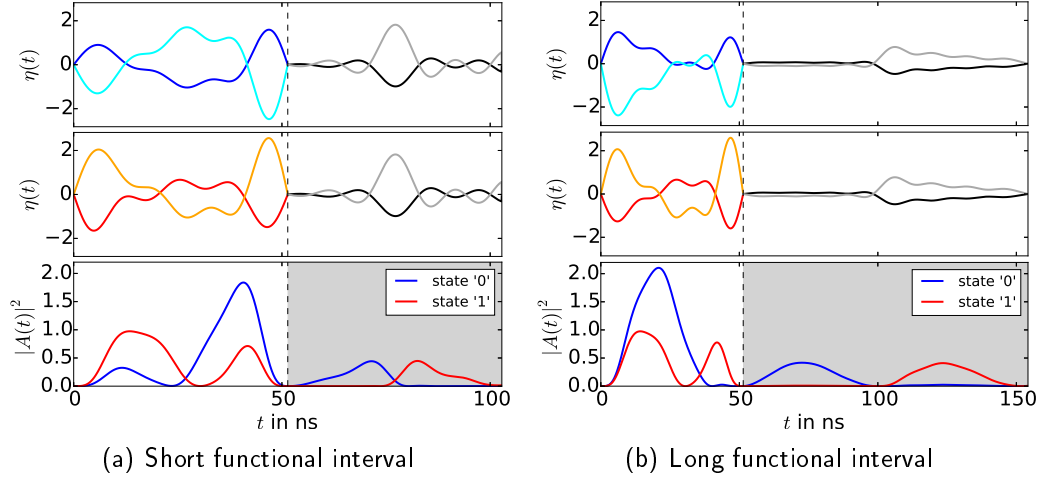


Figure 4.4: First and Second row: The smooth optimal writing pulses $\eta_{n,0}^{(1)}(t)$ (real part: blue, imaginary part: cyan) and $\eta_{n,1}^{(1)}(t)$ (real part: red, imaginary part: orange) followed by the same optimal readout pulse $\eta_{\mathcal{R}}^{(2)}(t)$ (real part: black, imaginary part: gray) defined by Eq. (4.1), Eq. (4.2) and Eq. (4.5). Third row: The corresponding cavity-amplitudes $A_{n,0}^{(n=1,2)}(t)$ (blue) and $A_{n,1}^{(n=1,2)}(t)$ (red) given by Eq. (4.3) and Eq. (4.4) in the writing region ($n = 1$) and by Eq. (4.6) and Eq. (4.7) in the readout region ($n = 2$). The dashed vertical cut separates the writing interval $[0, 51.4 \text{ ns}]$ in column (a) from a shorter readout interval $[51.4 \text{ ns}, 102.8 \text{ ns}]$ and in column (b) from a longer readout interval $[51.4 \text{ ns}, 154.2 \text{ ns}]$, respectively. The functional interval (gray area in last row) and the readout interval coincide, respectively.

To generate the numerical results depicted in Fig. 4.4, we chose the following configuration for the optimal control pulses: The writing pulses consist of $N_1 = 8$ and the readout pulses consist of $N_2 = 16$ components, respectively. (In fact, we use

this configuration for every pulse combination in the entire thesis.) The respective fundamental frequencies of the first and the second time interval are $\omega_0^{(1)} = \Omega_R$ and $\omega_0^{(2)} = \Omega_R/2$. Consequently, the even frequency components $2k \cdot \omega_0^{(2)}$ of the readout-pulse correspond to the frequency components $k \cdot \omega_0^{(1)}$ of the writing pulses, whereas the odd components $(2k-1) \cdot \omega_0^{(2)}$ only appear in the readout section. $\omega_0^{(1)}$ and $\omega_0^{(2)}$ are defined such that the lowest frequency component of the respective pulses cover the entire writing and readout region in Fig. 4.4(b) without a node, respectively. The respective amplitudes of the writing pulses are chosen to be twice as large as the amplitude of the readout pulse, which we achieve by setting $\mathcal{P}^{(2)} = \mathcal{P}^{(1)}/4$ in the net-power constraints Eq. (4.9) and Eq. (4.10). The writing pulses then correspond to short but "strong" initial kicks of the system with the purpose of providing enough energy during the writing interval. Due to the linearity of the Volterra description the pulse-amplitudes as well as the cavity-amplitudes can always be rescaled, therefore we normalize all powers to the writing-pulse power $\mathcal{P}^{(1)}$. Additionally, it is sufficient for our purposes to soften the constraint Eq. (4.10) for the readout-pulse such that $\mathcal{P}^{(2)} < \mathcal{U}^{(2)} = \mathcal{P}^{(1)}/4$ describes an upper limit for the readout-pulse power as described by Eq. (3.25).

4.1.3 Delayed Time-Binned Cavity-Responses

Above we demonstrate the possibility to create time-binned cavity-responses. We distinguish between the states "0" and "1" by means of the time-binned cavity-responses in the functional interval $[T_{\mathcal{F}}, T'_{\mathcal{F}}]$. However, this functional interval is defined as a subset of the readout region $[T_2, T_3]$ and can therefore be shifted such that there is a gap between the end of the writing section $[T_1, T_2]$ and the beginning of the functional interval $T_2 < T_{\mathcal{F}}$, see Fig. 4.3. After the end of the writing interval solely the readout pulse $\eta_{\mathcal{R}}^{(2)}(t)$ is applied during the whole second time-region $[T_2, T_3]$. This pulse, in turn, contains no information about which writing pulse $\eta_{0''}^{(1)}(t)$ or $\eta_{1''}^{(1)}(t)$ has been applied in the first interval $[T_1, T_2]$. Consequently, retrieving the time-binned cavity-amplitudes in a delayed functional interval denotes a storage protocol for the information, which was written into the system in the first interval. The functional tools of Sec. 4.1.1 can hence be used in the state of the art to describe a storage protocol.

Fig. 4.5 depicts numerical results for the time-binned responses and the corresponding preparation and readout pulses with the same parameters as those which are used in Fig. 4.4 except for a delayed functional interval by one Rabi-period $T_{\mathcal{F}} = T_2 + T_R$. The corresponding coefficients of the writing pulses and the readout pulses are listed in Tbl. B.1. The delayed time-binned cavity-responses depicted in Fig. 4.5(a) for a short functional interval look very similar to the corresponding solutions presented in Fig. 4.4(a). For the longer functional interval, delayed by the same amount of time, depicted in Fig. 4.5(b) we obtain qualitatively the same

behavior as for the reference case without delay, which is shown in Fig. 4.4(b). However, there is an emerging overlap of the time-binned cavity-responses $A_{|0\rangle}^{(2)}(t)$ and $A_{|1\rangle}^{(2)}(t)$ in Fig. 4.5(b) caused by the decoherence processes after the end of the writing interval. In fact, solely the two partial cavity-amplitudes $\tilde{A}_{|0\rangle}^{(2)}(t)$ and $\tilde{A}_{|1\rangle}^{(2)}(t)$, defined in Eq. (4.6) and Eq. (4.7), carry the information about the writing region. In contrast to photon-echo protocols [33, 35, 39], the weak intensity readout pulses $\eta_{\mathcal{R}}^{(2)}(t)$ we use in this thesis do not induce an echo of an excitation stored in the spin ensemble. They induce a partial readout amplitude $\tilde{A}_{\mathcal{R}}^{(2)}(t)$, also defined in Eq. (4.6) and Eq. (4.7), which is designed to interfere with the memory contributions $\tilde{A}_{|0\rangle}^{(2)}(t)$ and $\tilde{A}_{|1\rangle}^{(2)}(t)$ such that the complete cavity-responses $A_{|0\rangle}^{(2)}(t)$ and $A_{|1\rangle}^{(2)}(t)$ obtain a time-binned behavior in the functional interval. Since $\tilde{A}_{|0\rangle}^{(2)}(t)$ and $\tilde{A}_{|1\rangle}^{(2)}(t)$ evolve freely in the interval $[T_2, T_3]$ they are exponentially damped with the rate Γ . By increasing the delay or the length of the functional interval it becomes harder to find proper solutions for the time-binned cavity-amplitudes with reasonable magnitude. However, the phase relation of $\tilde{A}_{|0\rangle}^{(2)}(t)$ and $\tilde{A}_{|1\rangle}^{(2)}(t)$ does not suffer from these decoherence effects. Therefore, we can choose the magnitude of the time-binned responses to be sufficiently low by adjusting the parameter \mathcal{A} in Eq. (4.8) such that the damping of the amplitude is taken care of. The relative overlap of the time-binned cavity-responses shown in Fig. 4.5(b) can hence be reduced by the expense of reducing their intensity. Another way to circumvent this problem is presented in Sec. 4.1.3, where we make use of the cavity protection effect [10, 17, 23–25] to significantly reduce the total damping rate Γ of the system.

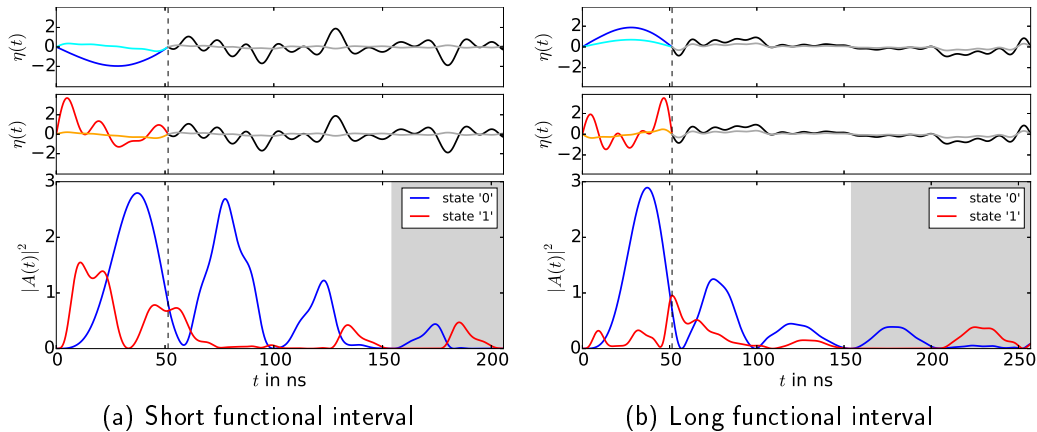


Figure 4.5: The same as Fig. 4.4(a) and Fig. 4.4(b) but with a delayed functional interval by one Rabi-period $T_R \approx 102.8$ ns in (a) [154.2 ns, 205.6 ns] and (b) [154.2 ns, 257.0 ns] (respective gray area in last row). The writing interval $[0, 51.4$ ns] and the total readout section in (a) [51.4 ns, 205.6 ns] and in (b) [51.4 ns, 257.0 ns] are separated by the vertical dashed cut, respectively.

This storage protocol is, however, rather implicit regarding the control pulses: for every different storage time a specific set of optimal control pulses has to be evaluated. We therefore investigate in [Appendix C](#) the capability of an independent single storage pulse $\eta_S^{(2)}(t)$ of duration ΔT_S being applied in between the writing interval and the readout interval (which is then delayed by ΔT_S). This protocol aims to store a snapshot of the entire configuration of the coupled system (cavity-mode and spin-waves) at the end of the writing interval T_2 to reestablish it at the end of the storage interval $T_2 + \Delta T_S$, independently of which pulse $\eta_{|0\rangle}^{(1)}(t)$ or $\eta_{|1\rangle}^{(1)}(t)$ was initially used. Subsequently, the delayed but predefined readout pulse $\eta_{\mathcal{R}}^{(2)}(t - \Delta T_S)$ is applied. The cavity-response to this delayed readout pulse should be equivalent to the time-binned cavity-response as if the readout pulse $\eta_{\mathcal{R}}^{(2)}(t)$ is directly applied after the writing interval. We show in [Appendix C](#) that, besides a considerable decrease in the amplitude of the restored time-binned responses compared to their original shape, the time-binned nature and the relative amplitudes and phases are restored with good accuracy. However, owing to decoherence processes the two restored time-binned cavity-responses slightly begin to overlap. We can already learn from [Eq. \(4.6\)](#) and [Eq. \(4.7\)](#), that the respective information-carrying part of the cavity-amplitudes $\tilde{A}_{|0\rangle}^{(2)}(t)$ and $\tilde{A}_{|1\rangle}^{(2)}(t)$ after the writing interval evolve independently of any cavity-field contribution arising from the readout-pulse or from a storage pulse. Thus we can not manipulate or enhance $\tilde{A}_{|0\rangle}^{(2)}(t)$ and $\tilde{A}_{|1\rangle}^{(2)}(t)$ by such a storage pulse in the linear regime. The delayed readout technique put forward in this section gives better results with respect to the conservation of the amplitudes and we therefore focus on this approach in the rest of the thesis.

4.2 Superposition of Time-Binned Responses

With our optimization procedure we are able to create two distinguishable time-binned cavity-responses $A_{|0\rangle}^{(2)}(t)$ and $A_{|1\rangle}^{(2)}(t)$, which carry information about the preliminarily applied writing pulses $\eta_{|0\rangle}^{(1)}(t)$ and $\eta_{|1\rangle}^{(1)}(t)$. A very important question regarding quantum-information protocols is, if it is possible to encode coherent superpositions of these writing pulses into the time-binned cavity-responses. The cavity-amplitudes in the reading region $A_{|0\rangle}^{(2)}(t) = \tilde{A}_{|0\rangle}^{(2)}(t) + \tilde{A}_{\mathcal{R}}^{(2)}(t)$ and $A_{|1\rangle}^{(2)}(t) = \tilde{A}_{|1\rangle}^{(2)}(t) + \tilde{A}_{\mathcal{R}}^{(2)}(t)$ are solved by [Eq. \(4.6\)](#) and [Eq. \(4.7\)](#). We identify $A_{|0\rangle}^{(2)}(t)$ and $A_{|1\rangle}^{(2)}(t)$ in the functional interval as basis functions (or logical states) "0" and "1".

4.2.1 Superimposing the Writing-Pulses

Since we prepared the states "0" and "1" by probing the system with the respective pulses $\eta_{|0\rangle}^{(1)}(t)$ and $\eta_{|1\rangle}^{(1)}(t)$ in the first place, we assume to create coherent superpositions of the cavity-responses by simply superimposing the two writing pulses defined

by Eq. (4.1) and Eq. (4.2) according to

$$\begin{aligned}\eta^{(1)}(t; \gamma, \delta) &= \gamma \eta_{\text{"0"}}^{(1)}(t) + \delta \eta_{\text{"1"}}^{(1)}(t) \\ &= \sum_{k=1}^{N_1} \alpha_k(\gamma, \delta) \sin\left(k \omega_0^{(1)}(t - T_1)\right),\end{aligned}\quad (4.11)$$

where we define the k -th superimposed harmonic coefficient $\alpha_k(\gamma, \delta) = \gamma \alpha_k^{\text{"0"}} + \delta \alpha_k^{\text{"1"}}$. Because of the linear appearance of the harmonic coefficients in the derivations of Sec. 3.1.2 and Sec. 3.1.3, we can write the resulting cavity-amplitude in the writing and reading section analogously to Eq. (3.5) and Eq. (3.12) as

$$\begin{aligned}A^{(1)}(t; \gamma, \delta) &= \sum_{k=1}^{N_1} \alpha_k(\gamma, \delta) a_k^{(1)}(t) \\ &= \gamma A_{\text{"0"}}^{(1)}(t) + \delta A_{\text{"1"}}^{(1)}(t)\end{aligned}\quad (4.12)$$

$$\begin{aligned}A^{(2)}(t; \gamma, \delta) &= \sum_{k=1}^{N_1} \alpha_k(\gamma, \delta) \psi_k^{(2)}(t) + \sum_{l=1}^{N_2} \alpha_l^{\mathcal{R}} a_l^{(2)}(t) \\ &= \left(\gamma \tilde{A}_{\text{"0"}}^{(2)}(t) + \delta \tilde{A}_{\text{"1"}}^{(2)}(t)\right) + \tilde{A}_{\mathcal{R}}^{(2)}(t),\end{aligned}\quad (4.13)$$

using the superimposed coefficients $\alpha_k(\gamma, \delta)$. With $A_{\text{"0"}}^{(1)}(t)$ and $A_{\text{"1"}}^{(1)}(t)$ given by Eq. (4.3) and Eq. (4.4) the cavity-amplitude in the first time interval $A^{(1)}(t; \gamma, \delta)$ resembles the linear superposition of the respective writing pulse $\eta^{(1)}(t; \gamma, \delta)$. To describe $A^{(2)}(t; \gamma, \delta)$ we used the partial cavity-amplitudes $\tilde{A}_{\text{"0"}}^{(2)}(t)$, $\tilde{A}_{\text{"1"}}^{(2)}(t)$ and $\tilde{A}_{\mathcal{R}}^{(2)}(t)$. With the preparation pulse $\eta^{(1)}(t; \gamma, \delta)$ all possible combinations of the superposition amplitudes γ and δ can be written into the system. The challenge is now to identify the amplitudes γ and δ from the superimposed cavity-amplitude $A^{(2)}(t; \gamma, \delta)$ in the functional interval.

4.2.2 Restricted Superposition, Encoding a Real-Bit

A problem we encounter in our analysis is that the cavity-amplitude in the reading section $A^{(2)}(t; \gamma, \delta)$ is no longer a linear superposition of "0" and "1" with the relative amplitudes γ and δ . Since our protocol was designed to use an optimized unique readout-pulse $\eta_{\mathcal{R}}^{(2)}(t)$ such as to distinguish between the system configurations "0" and "1", the readout part $\tilde{A}_{\mathcal{R}}^{(2)}(t)$ in Eq. (4.13) does not change. Therefore, only the part $\gamma \tilde{A}_{\text{"0"}}^{(2)}(t) + \delta \tilde{A}_{\text{"1"}}^{(2)}(t)$ is superimposed in a proper way. A coherent superposition of the total cavity-responses $A_{\text{"0"}}^{(2)}(t)$ and $A_{\text{"1"}}^{(2)}(t)$ in the functional interval

$$\begin{aligned}A_{sup}^{(2)}(t; \gamma, \delta) &= \gamma A_{\text{"0"}}^{(2)}(t) + \delta A_{\text{"1"}}^{(2)}(t) \\ &= \left(\gamma \tilde{A}_{\text{"0"}}^{(2)}(t) + \delta \tilde{A}_{\text{"1"}}^{(2)}(t)\right) + (\gamma + \delta) \tilde{A}_{\mathcal{R}}^{(2)}(t)\end{aligned}\quad (4.14)$$

would also require to correspondingly alter the readout pulse $\eta_{\mathcal{R}}^{(2)}(t) \rightarrow (\gamma + \delta) \eta_{\mathcal{R}}^{(2)}(t)$. Consequently we would always have to know in which state the system has initially been prepared, to correctly readout the information. This protocol may be used for the generation of time-binned responses similar to [51] but it falls short of the demands one has on a memory protocol. However, for the following restricted parametrization

$$\gamma + \delta = 1, \quad (4.15)$$

which preserves the relative power and the relative phase between the writing pulse and the reading pulse, the superposition of the solutions governed by Eq. (4.14) is equal to the cavity-response $A^{(2)}(t; \gamma, \delta)$ defined by Eq. (4.13), more precisely we find $A_{sup}^{(2)}(t; \gamma = 1 - \delta, \delta) = A^{(2)}(t; \gamma = 1 - \delta, \delta)$. In the case of a qubit the superposition amplitudes γ and δ have to be located on the complex unit-sphere $|\gamma|^2 + |\delta|^2 = 1$ [40]. With our protocol we are able to encode one real-bit into the time-binned cavity-responses, that is one real valued coefficient δ , while $\gamma(\delta) = 1 - \delta$ is fixed. The results of superimposing the two sets of basis states depicted in Fig. 4.5(a) and Fig. 4.5(b) with this real-bit parametrization are presented in Fig. 4.6(a) and Fig. 4.6(b), respectively. A smooth transition from state "0" to state "1" can be performed by varying δ from 0 to 1.

Having prepared the system in a superposition state $A^{(1)}(t; \gamma, \delta)$, we aim to extract the relative amplitudes γ and δ of the writing pulse $\gamma \eta_{|0\rangle}^{(1)}(t) + \delta \eta_{|1\rangle}^{(1)}(t)$ solely from the cavity-amplitude $A^{(2)}(t; \gamma, \delta)$ in the functional interval $[T_{\mathcal{F}}, T'_{\mathcal{F}}]$. The superimposed cavity-response depends on γ and δ but in general we do not know these two parameters in the readout section. To reevaluate the corresponding parameters, we make use of the orthogonality of the time-binned basis functions $A_{|0\rangle}^{(2)}(t)$ and $A_{|1\rangle}^{(2)}(t)$ in the functional interval $[T_{\mathcal{F}}, T'_{\mathcal{F}}]$. More precisely, we define the overlap of $A^{(2)}(t; \gamma, \delta)$ with the cavity-responses $A_{|i\rangle}^{(2)}(t)$ as

$$\mathcal{O}_i = \frac{\left| \int_{T_{\mathcal{F}}}^{T'_{\mathcal{F}}} dt A^{(2)}(t; \gamma, \delta) \cdot \left(A_{|i\rangle}^{(2)}(t) \right)^* \right|}{\int_{T_{\mathcal{F}}}^{T'_{\mathcal{F}}} dt |A_{|i\rangle}^{(2)}(t)|^2}, \quad (4.16)$$

for $i = 1, 0$, respectively. \mathcal{O}_i can be identified as a projection measure of $A^{(2)}(t; \gamma, \delta)$ onto $A_{|i\rangle}^{(2)}(t)$ with an implicit dependence on the amplitudes γ and δ , which we dropped on the left hand side of Eq. (4.16). Moreover, for perfectly orthogonal basis functions and for $\gamma + \delta = 1$ we find that

$$\gamma_{\mathcal{R}} = \mathcal{O}_0, \quad \delta_{\mathcal{R}} = \mathcal{O}_1 \quad (4.17)$$

uniquely defines the relative amplitudes $\gamma_{\mathcal{R}} = \gamma$ and $\delta_{\mathcal{R}} = \delta$ of the writing pulse $\gamma \eta_{|0\rangle}^{(1)}(t) + \delta \eta_{|1\rangle}^{(1)}(t)$. Fig. 4.6(c) and Fig. 4.6(d) show the retrieved parameters

$\gamma_{\mathcal{R}} = \mathcal{O}_0$ and $\delta_{\mathcal{R}} = \mathcal{O}_1$ as a function of the initial parameter $\delta \in [0, 1]$, evaluated from the cavity-amplitudes depicted in Fig. 4.6(a) and Fig. 4.6(b), respectively. Especially for the short functional interval shown in Fig. 4.6(c) the accuracy of the retrieved parameters is (almost) perfect. For the longer functional interval we find in Fig. 4.6(d) a significant bias of $\gamma_{\mathcal{R}}$ and $\delta_{\mathcal{R}}$ from their initial values γ and δ due to the finite overlap of the basis functions $A_{\mathcal{R},0}^{(2)}(t)$ and $A_{\mathcal{R},1}^{(2)}(t)$, which are depicted in Fig. 4.4(b). However, the retrieved parameters still show a strictly linear behavior, which allows a unique mapping to the initial ones.

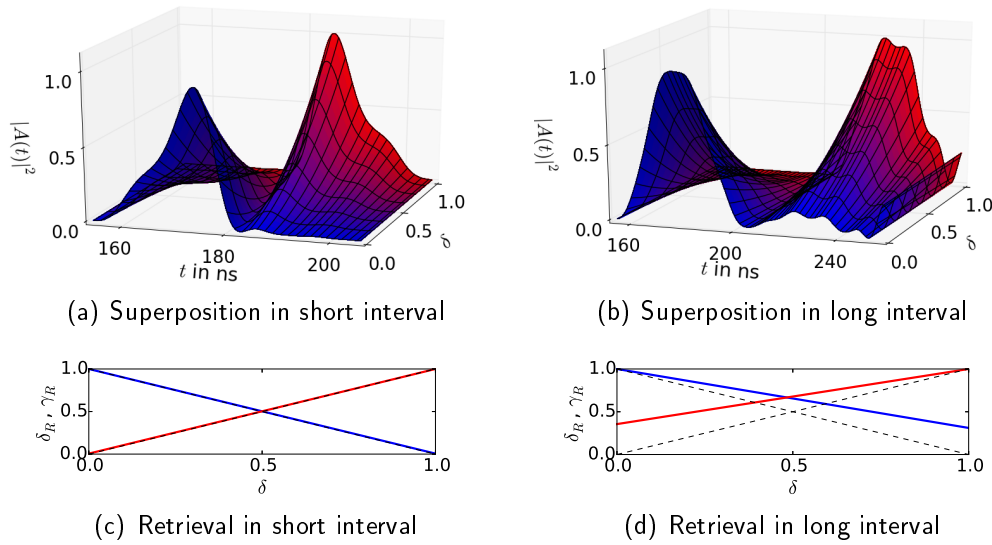


Figure 4.6: (a) and (b) depict the normalized, superimposed cavity-amplitude $A^{(2)}(t; \gamma, \delta) / \max[A^{(2)}(t; \gamma, \delta)]$ defined in Eq. (4.13) (z-axis) in the functional interval (x-axis) as a function of the real-bit parameter δ according to Eq. (4.15) (y-axis) for two sets of reference states "0" and "1" and optimal control pulses $\eta_{\mathcal{R},0}^{(1)}(t)$, $\eta_{\mathcal{R},1}^{(1)}(t)$ and $\eta_{\mathcal{R}}^{(2)}(t)$ taken from Fig. 4.5(a) and Fig. 4.5(b), respectively. Varying δ from $0 \rightarrow 1$ yields a continuous transition from state "0" to "1" (indicated by the surface-color blue \rightarrow red). The blue and the red lines in (c) and (d) depict the retrieved amplitudes $\gamma_{\mathcal{R}}$ and $\delta_{\mathcal{R}}$, given by Eq. (4.17), from the cavity-amplitudes depicted in (a) and (b) as a function of the parameter $\delta \in [0, 1]$, respectively. The initial parameters δ and $\gamma = 1 - \delta$ are denoted by the black dashed lines in (c) and (d).

4.2.3 Retrieval of Two Real-Valued Parameters

As we pointed out above, the purpose of the readout-pulse is to generate time-binned cavity-responses by interference of the partial readout contribution $\tilde{A}_{\mathcal{R}}^{(2)}(t)$ with the partial cavity-amplitudes $\tilde{A}_{\mathcal{R},0}^{(2)}(t)$ and $\tilde{A}_{\mathcal{R},1}^{(2)}(t)$ such that $A_{\mathcal{R},0}^{(2)}(t)$ and $A_{\mathcal{R},1}^{(2)}(t)$

are orthogonal in a predefined functional interval in terms of a time-binned separation. An arbitrary superposition of the writing pulses $\eta^{(1)}(t; \gamma, \delta) = \gamma \eta_{|0\rangle}^{(1)}(t) + \delta \eta_{|1\rangle}^{(1)}(t)$ does, however, not prepare a corresponding superposition of the full time-binned cavity-amplitudes $\gamma A_{|0\rangle}^{(2)}(t) + \delta A_{|1\rangle}^{(2)}(t)$, since the readout part $\tilde{A}_{\mathcal{R}}^{(2)}(t)$ is fixed. The corresponding cavity-response acquires the form $A^{(2)}(t; \gamma, \delta) = \gamma \tilde{A}_{|0\rangle}^{(2)}(t) + \delta \tilde{A}_{|1\rangle}^{(2)}(t) + \tilde{A}_{\mathcal{R}}^{(2)}(t)$. Consequently, the projection measure governed by [Eq. \(4.16\)](#) does in general obtain non-vanishing cross terms of the different partial cavity-amplitudes. Despite this drawback, the relative amplitudes of an arbitrarily superimposed writing pulse $\eta^{(1)}(t; \gamma, \delta)$ can, however, be rigorously extracted from the evolution of the cavity-amplitude $A^{(2)}(t; \gamma, \delta)$ during the entire functional interval $[T_{\mathcal{F}}, T'_{\mathcal{F}}]$ such that a qubit of information can be stored in the ensemble. (Although the strict picture of superimposed time-binned cavity-amplitudes does no longer hold in general.)

To see this we explicitly project $A^{(2)}(t; \gamma, \delta)$ onto the two known cavity-amplitudes $A_{|0\rangle}^{(2)}(t)$ and $A_{|1\rangle}^{(2)}(t)$ similar to [Eq. \(4.16\)](#) and we get

$$\tilde{\mathcal{O}}_i = \int_{T_{\mathcal{F}}}^{T'_{\mathcal{F}}} dt A^{(2)}(t; \gamma, \delta) \cdot \left(A_{|i\rangle}^{(2)}(t) \right)^* \quad (4.18)$$

$$= \gamma \cdot \mathcal{F}_{i,0} + \delta \cdot \mathcal{F}_{i,1} + \mathcal{F}_{i,\mathcal{R}}, \quad (4.19)$$

where we introduced the overlap integrals

$$\mathcal{F}_{i,q} = \int_{T_{\mathcal{F}}}^{T'_{\mathcal{F}}} dt \tilde{A}_q^{(2)}(t) \cdot \left(A_{|i\rangle}^{(2)}(t) \right)^* \quad (4.20)$$

for $i = 0, 1$ and $q \in \{|0\rangle, |1\rangle, \mathcal{R}\}$. Every integral $\mathcal{F}_{i,q}$ can be evaluated solely from the partial cavity-amplitudes $\tilde{A}_{|0\rangle}^{(2)}(t)$, $\tilde{A}_{|1\rangle}^{(2)}(t)$ and $\tilde{A}_{\mathcal{R}}^{(2)}(t)$ for a specific solution of time-binned cavity-responses. Further, given a corresponding cavity-amplitude $A^{(2)}(t; \gamma, \delta)$ with unknown parameters γ and δ , the quantities $\tilde{\mathcal{O}}_0$ and $\tilde{\mathcal{O}}_1$ can be evaluated with [Eq. \(4.18\)](#). $\tilde{\mathcal{O}}_0$ and $\tilde{\mathcal{O}}_1$ implicitly depend on γ and δ but we do not indicate them as arguments to emphasize that [Eq. \(4.18\)](#) describes a projection-measure of an arbitrarily superimposed cavity-amplitude $A^{(2)}(t; \gamma, \delta)$. Using [Eq. \(4.19\)](#) then yields two algebraic equations featuring the two unknown parameters γ and δ , which can be uniquely determined by

$$\gamma_{\mathcal{R}} = \frac{(\tilde{\mathcal{O}}_0 - \mathcal{F}_{0,\mathcal{R}})\mathcal{F}_{1,1} - (\tilde{\mathcal{O}}_1 - \mathcal{F}_{1,\mathcal{R}})\mathcal{F}_{0,1}}{\mathcal{F}_{0,0}\mathcal{F}_{1,1} - \mathcal{F}_{0,1}\mathcal{F}_{1,0}}, \quad (4.21)$$

$$\delta_{\mathcal{R}} = \frac{(\tilde{\mathcal{O}}_1 - \mathcal{F}_{1,\mathcal{R}})\mathcal{F}_{0,0} - (\tilde{\mathcal{O}}_0 - \mathcal{F}_{0,\mathcal{R}})\mathcal{F}_{1,0}}{\mathcal{F}_{0,0}\mathcal{F}_{1,1} - \mathcal{F}_{0,1}\mathcal{F}_{1,0}}. \quad (4.22)$$

The subscript R denotes that γ_R and δ_R are retrieved parameters which are a measure for the original contribution of γ and δ to the writing pulse $\eta^{(1)}(t; \gamma, \delta)$.

In order to demonstrate the capability of our approach to retrieve any superposition of the writing pulses $\eta_{0,0}^{(1)}(t)$ and $\eta_{1,1}^{(1)}(t)$ from the corresponding superimposed cavity-amplitudes $A^{(2)}(t; \gamma, \delta)$, we parametrize $\gamma = \cos(\vartheta/2)$ and $\delta = \sin(\vartheta/2) e^{i\varphi}$ with $\vartheta \in [0, \pi]$ and $\varphi \in [0, 2\pi]$ satisfying $|\gamma|^2 + |\delta|^2 = 1$ [22]. By the use of Eq. (4.21) and Eq. (4.22) we then retrieve γ_R and δ_R as a function of the initial parameters ϑ and φ . The results of this procedure are presented in Fig. 4.7 and Fig. 4.8 with reference data taken from Fig. 4.5(a) and Fig. 4.5(b), respectively.

To address the reliability of the retrieved quantities we introduce the absolute error $\epsilon_\gamma = |\gamma - \gamma_R|$ and $\epsilon_\delta = |\delta - \delta_R|$ between the initial parameters γ and δ and the retrieved amplitudes γ_R and δ_R . This error is shown in the last row of Fig. 4.7 and Fig. 4.8, respectively.

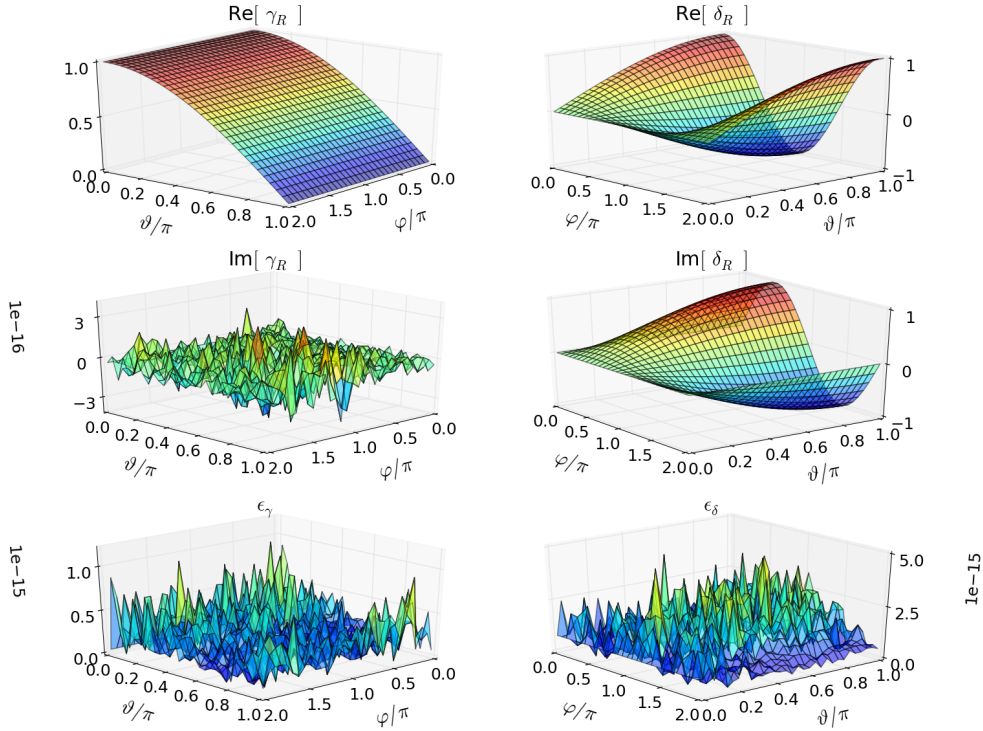


Figure 4.7: Retrieved parameters γ_R (left column) and δ_R (right column) obtained by Eq. (4.21) and Eq. (4.22) from the superimposed cavity-amplitude $A^{(2)}(t; \gamma, \delta)$ given by Eq. (4.13) with the parametrization $\gamma = \cos(\vartheta/2)$ and $\delta = \sin(\vartheta/2) e^{i\varphi}$ for $\vartheta \in [0, \pi]$ and $\varphi \in [0, 2\pi]$. The last row depicts the absolute error $\epsilon_\gamma = |\gamma - \gamma_R|$ and $\epsilon_\delta = |\delta - \delta_R|$ between the initial parameters γ and δ and the reconstructed amplitudes γ_R and δ_R as a function of ϑ and φ , respectively, which is of the order $5 \cdot 10^{-15}$ and resembles the numerical machine error. The reference data to generate $A^{(2)}(t; \gamma, \delta)$ are taken from Fig. 4.5(a).

Remarkably, with our method the superposition parameters $\gamma = \gamma_R$ and $\delta = \delta_R$, which here describe one qubit of information, can be perfectly restored (up to the machine error of the order $5 \cdot 10^{-15}$). As can be seen in Fig. 4.8 this is even true for the reference data taken from Fig. 4.6(b), where decoherence effects already cause a significant overlap of the two basis functions $A_{|0\rangle}^{(2)}(t)$ and $A_{|1\rangle}^{(2)}(t)$. Our reconstruction procedure is only limited if the cavity-amplitudes are very small in magnitude such that they are comparable to the level of noise. In a further study one can think of phenomenologically including noise to the cavity-amplitude in the optimization procedure of the control pulses such that the retrieval fidelity of arbitrary superpositions is maximal.

It should be noted that, by making use of the Pauli-matrices $\vec{\sigma} = (\sigma_x, \sigma_y, \sigma_z)^T$, the respective tuples of the initial and the reconstructed superposition parameters $|\chi\rangle \hat{=} (\gamma, \delta)^T$ and $|\chi_R\rangle \hat{=} (\gamma_R, \delta_R)^T$ depicted in Fig. 4.7 and Fig. 4.8 can be mapped to a three-dimensional real-valued vector $\vec{r} = \langle \chi | \vec{\sigma} | \chi \rangle$ and $\vec{r}_R = \langle \chi_R | \vec{\sigma} | \chi_R \rangle$. This is the so-called Bloch-vector $\vec{r} = (\cos(\varphi) \sin(\vartheta), \sin(\varphi) \sin(\vartheta), \cos(\vartheta))^T$ [22].

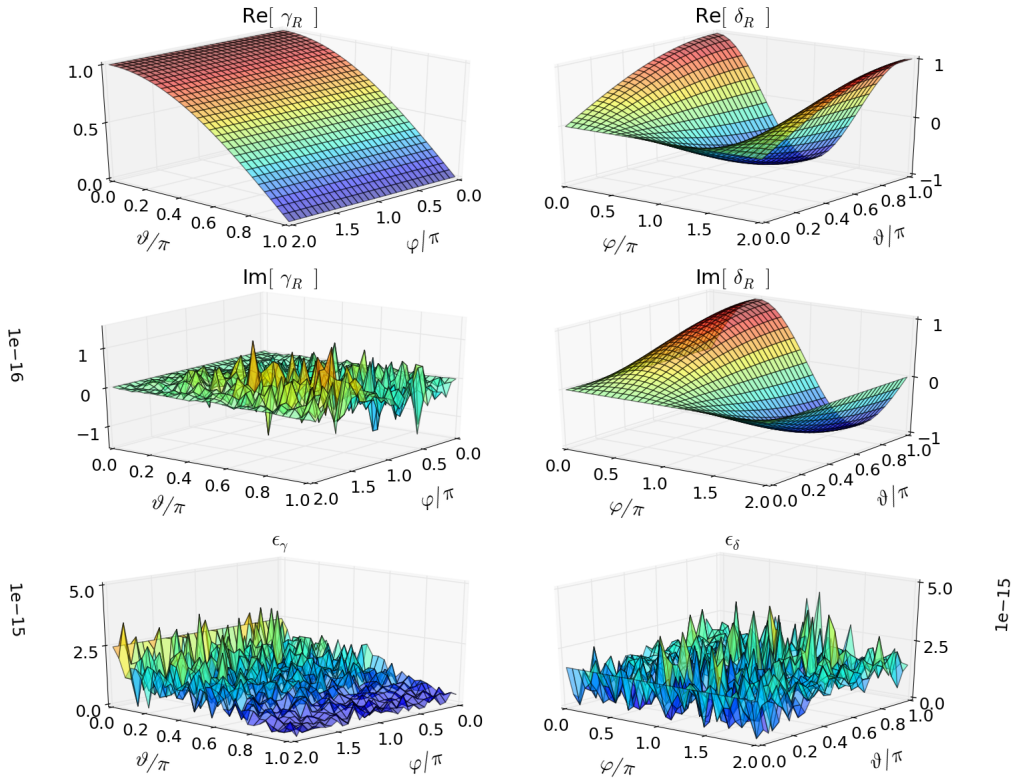


Figure 4.8: The same as Fig. 4.7 but with reference data taken from Fig. 4.5(b).

In the retrieval of the parameters γ_R and δ_R by Eq. (4.21) and Eq. (4.22), the contribution of the partial readout amplitude $\tilde{A}_{\mathcal{R}}^{(2)}(t)$ is always eliminated and hence one can think of completely omitting the readout pulse in this encoding scheme. However, the readout-pulse is very well justified in terms of a time-delayed retrieval of the information, as we show later in Sec. 4.3.2. Its purpose is to suppress the cavity-response between the end of the writing section and the beginning of the functional interval by destructive interference. An interesting approach, which can be achieved with our optimal control tools, would be to functionally minimize to readout contribution $\tilde{A}_{\mathcal{R}}^{(2)}(t)$ in the retrieval interval (but only in this interval). Consequently there will be no interference terms between the readout part $\tilde{A}_{\mathcal{R}}^{(2)}(t)$ and the partial cavity-amplitudes $\tilde{A}_{\nu_0}^{(2)}(t)$ and $\tilde{A}_{\nu_1}^{(2)}(t)$ in this interval. In order to be well distinguishable regarding their overlap, we suggest the partial cavity-amplitudes $\tilde{A}_{\nu_0}^{(2)}(t)$ and $\tilde{A}_{\nu_1}^{(2)}(t)$ to be orthogonal functions in functional interval (not necessarily in a time-binned fashion). This protocol would then have the advantage that two arbitrary superposition parameters could be determined directly (without cross terms) in a similar way as with Eq. (4.17). A generalization to more than two orthogonal cavity-amplitudes (or basis-functions) seems accessible with our techniques leading to a multi-dimensional encoding scheme. This, in turn, is closely related to the concept of continuous variable quantum information processing [52].

4.3 Enhanced Storage-Time by Cavity Protection

In the strong coupling regime the stationary transmission spectrum shows two resonance peaks, which are split by the Rabi-frequency Ω_R and have a width of Γ , as can be seen in Fig. 2.5. These resonance- or polaritonic peaks resemble the level structure of the polaritonic eigenstates of the system, which are a hybridization of the cavity-mode and the superradiant spin-wave modes [10, 24]. Due to this hybridization the superradiant spin-wave modes are visible in transmission experiments, which is why they are also called bright-states [10, 24]. The stronger the coupling Ω the broader the level-splitting $2 \cdot \Omega_R$ and the gap $2 \cdot \Omega_R$ between the resonance peaks in the transmission spectrum. In the presence of inhomogeneous broadening, however, the polaritonic states (and peaks) spectrally overlap with the inhomogeneously broadened ensemble $\rho(\omega)$ inducing a coupling of the polaritonic states to a bath of subradiant spin-wave modes, which do not hybridize with the cavity-mode and thus are referred to as dark-states [6, 10, 24]. This process, which manifests itself in the broadening of the resonance peaks, acts as the main source of decoherence in ensemble based systems [10]. In the limit of large values of the coupling strength $\Omega \gg \Gamma$ the total decoherence rate of the coupled system under study can be estimated by

$$\Gamma \approx \kappa + \pi \Omega^2 \rho(\omega_s \pm \Omega) \quad (4.23)$$

either from the width of the polaritonic peaks in the stationary transmission spectrum [10, 17] or by Laplace-transform of the Volterra integral equation [23, 25]. In fact, we can see that the inhomogeneously broadened transition line of the ensemble, modeled by the spin density distribution $\rho(\omega)$, contributes to the total decoherence rate via the second term $\pi \Omega^2 \rho(\omega_s \pm \Omega)$ [7, 8]. However, if the spectral tails of the spin-distribution $\rho(\omega_s \pm \Omega)$ fall off faster than $1/\Omega^2$ the product $\Omega^2 \rho(\omega_s \pm \Omega)$ vanishes, provided the collective coupling strength Ω is sufficiently large [10, 17, 23]. The spectral density of the considered NV-center-ensemble, which is depicted in Fig. 2.3, exhibits a q-Gaussian shape and thus satisfies this prerequisite [7, 8]. Physically, this can be explained as follows: By increasing the coupling strength, the level-splitting grows and the transmission peaks get shifted apart from each other while $\rho(\omega)$ remains unchanged. Therefore, the polaritonic states get energetically decoupled from the bath of dark-states and become protected from decoherence [10, 17]. Intuitively, we can think of the inhomogeneously broadened ensemble to become spectrally decoupled from the polaritonic peaks by increasing the collective coupling such that $\rho(\omega)$ effectively becomes a sharp transition line (provided the spectral tails drop faster than $1/\omega^2$). The system then is naturally protected against decoherence and this effect is known as "cavity protection" [10, 17].

It should be noted that the lowest possible value for the decoherence rate $\Gamma = \kappa$ lies below the total loss rate of the bare cavity, which is 2κ . This is a consequence of the periodic exchange of energy between the cavity and the spin ensemble in the form of collective Rabi-oscillations as depicted in Fig. 2.6: Only half of the time the energy is present in the cavity, where it decays with the rate 2κ [24].

4.3.1 Reduced Decoherence by Increasing the Coupling

Due to the cavity protection effect the total decoherence rate of the system can be reduced by going to large values of the collective coupling strength. Consequently, the quality of the time-binned cavity-responses with a delayed readout can significantly be increased. In Fig. 4.9(a) we present the results for delayed time-binned responses similar to Fig. 4.5(a) but with a collective coupling strength $\Omega = 2\pi \cdot 17.12$ MHz, which is twice as large as before. Fig. 4.9(b) shows the real-bit superposition of the cavity-responses $\gamma A_{s_0}^{(2)}(t) + \delta A_{s_1}^{(2)}(t)$ with the restriction $\gamma + \delta = 1$. The enhanced coupling affects the Rabi-frequency of the system $\Omega_R \approx 18.08$ MHz (or the Rabi-period $T'_R = 55.32$ ns). Therefore we adjust the fundamental frequencies of the writing-pulses and the readout-pulse by $\omega_0^{(1)} = \Omega_R/2$ and $\omega_0^{(2)} = \Omega_R/4$ to get a similar structure of the control pulses as before. The other system-parameters are the same as in Fig. 4.4. The harmonic pulse-coefficients are listed in Tbl. B.2 and the corresponding time-divisions can be found in the caption of Fig. 4.9. The time-binned responses $A_{s_0}^{(2)}(t)$ and $A_{s_1}^{(2)}(t)$ are almost perfectly orthogonal regarding their overlap in the functional interval and, although the

functional interval is delayed by approximately 170 ns, the retrieval of the real-bit parameters governed by Eq. (4.17) is almost perfect as can be seen in Fig. 4.9(c). Also the retrieval of two arbitrary parameters put forward in Sec. 4.2.3, which we do not explicitly present here, can be performed with an equivalent accuracy as presented in Fig. 4.7 and Fig. 4.8. In Fig. 4.9(a) we see that at the end of the writing section both cavity-amplitudes are exactly zero. Thus the information about the preliminarily applied writing pulse is solely stored inside the spin ensemble at this moment of time.

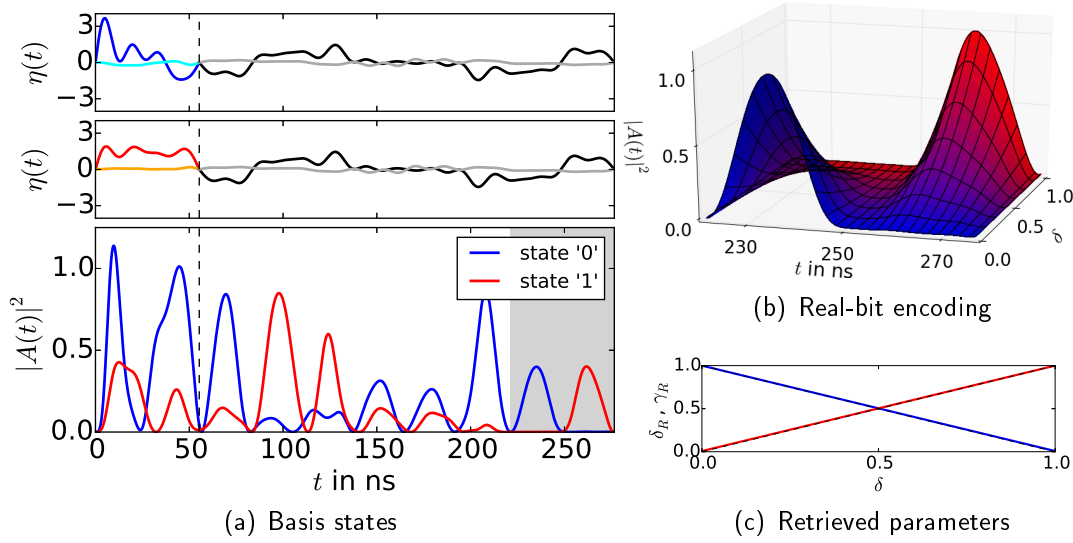


Figure 4.9: Numerical results for (a) the delayed time-binned cavity-responses, (b) for the real-bit encoding and (c) the retrieved real-bit parameters γ_R (blue) and δ_R (red) similar to Fig. 4.5(a), Fig. 4.6(a) and Fig. 4.6(c) except for a doubled collective coupling strength $\Omega = 2\pi \cdot 17.12$ MHz and the adjusted time-divisions of the writing interval $[0, 55.3$ ns], the readout interval $[55.3$ ns, 276.6 ns] and the functional interval $[221.2$ ns, 276.6 ns] ((b) and gray area in (a)).

The value of the collective coupling strength is close to the limit of what is experimentally reachable today and, moreover, the corresponding total decoherence rate Γ of the system approaches its limiting value κ [24]. Due to this reduced damping of the cavity-amplitude it takes longer until the cavity-amplitude is comparable to the noise-level as for previous results. By making use of the cavity protection effect the method of a delayed functional interval of Sec. 4.1.3 is therefore much better suited to store information about the writing pulses as compared to the refocusing technique of Appendix C.

4.3.2 Micro-Second Storage by Spectral Hole-Burning

An alternative way to suppress the decoherence rate of the system at modest values of the coupling strength $\Omega = 2\pi \cdot 8.56$ MHz is to modify the spectral spin-density at judiciously chosen frequencies by spectral hole burning [25]. Taking the expression for the total decoherence rate Γ literal, that is Eq. (4.23), one can eliminate the second term $\pi \Omega^2 \rho(\omega_s \pm \Omega)$ by assuming a spin-density, which is zero in the vicinity of $\omega_s \pm \Omega$ (and remains unchanged elsewhere) [25].

Remarkably, a decoherence rate of the entire system of $\Gamma = 0.42 \kappa$ has numerically been evaluated in [25] for Gaussian holes with a width of $2\pi \cdot 1.4$ MHz. This is all the more surprising, since this value even lies significantly below κ , which was identified as the limiting lowest value attainable for the total decoherence rate in recent studies [10, 17, 23, 25]. However, recent experimental results confirm this behavior [53]. The presence of holes at $\omega_s \pm \Omega$ in the spin distribution give rise to very sharp and very high resonance peaks in the stationary transmission analysis, which lie on top of the polaritonic peaks depicted in Fig. 2.5 [25]. Moreover, these additional sharp resonances in the stationary transmission spectrum can be explained, similar to the discussion in Sec. 4.3, with the concept of polaritonic states, which are spectrally located in the vicinity of the hole-center-frequencies $\omega_s \pm \Omega$ [53]. If the width of the holes exceeds the width of the sharp polaritonic peaks, the corresponding polaritonic states decouple (almost) completely from the bath of subradiant (dark) states [25, 53], which gives rise to a slow asymptotic behavior in the dynamical regime [25]. From the mathematical point of view this drastically decreased decoherence rate Γ and the corresponding slow asymptotic behavior is associated with the contribution of two poles in the Laplace transform of Eq. (2.7) [24], which appear when the holes in $\rho(\omega)$ reach a certain depth [25]. The holes in the spin-density have been experimentally realized by applying a strong microwave pulse, modulated with spectral components at $\omega_s \pm \Omega$ and the life-time of the holes has been estimated to be approximately given by $20 \mu\text{s}$ in [53].

The spin-density $\rho(\omega)$ enters the Volterra integral equation phenomenologically. Therefore we use a modified spin-density $\rho_h(\omega)$ in our calculations, featuring two Gaussian holes of width $\Delta_h = 2\pi \cdot 0.7$ MHz located at the frequencies $\omega_s \pm \Omega$, which is assumed to be prepared before the writing pulses are applied to the cavity. Since the life-time of the holes greatly exceeds all time-intervals we consider above, which are of the order of 100 ns, we further assume the holes in the spin-density to remain unchanged during our protocol.

To demonstrate the efficiency of the hole burning effect, we redefine the writing interval $[T_1, T_2] = [0, 102.8 \text{ ns}]$, the readout interval $[T_2, T_3] = [102.8 \text{ ns}, 1.33 \mu\text{s}]$ and the functional interval $[T_{\mathcal{F}}, T'_{\mathcal{F}}] = [1.22 \mu\text{s}, 1.33 \mu\text{s}]$, which is delayed from the end of the writing sequence by $1.12 \mu\text{s}$, compared to all former results. Due to this long delay, we functionally suppress the cavity-amplitude in the interval $[T_2, T_{\mathcal{F}}]$ for both states "*i*" = "0", "1" by additionally including the constraint $\int_{T_2}^{T_{\mathcal{F}}} dt |A_{i''}^{(2)}(t)|^2 \rightarrow 0$

in the minimization of Eq. (4.8). Otherwise large values of the cavity-amplitude (and consequently of the transmission) in this interval would drastically reduce the efficiency for the readout of the time-binned responses in the functional interval. The corresponding optimal control pulses and the time-binned cavity-responses are depicted in Fig. 4.10, where we further present the modified spin-distribution $\rho_h(\omega)$ as an inset.

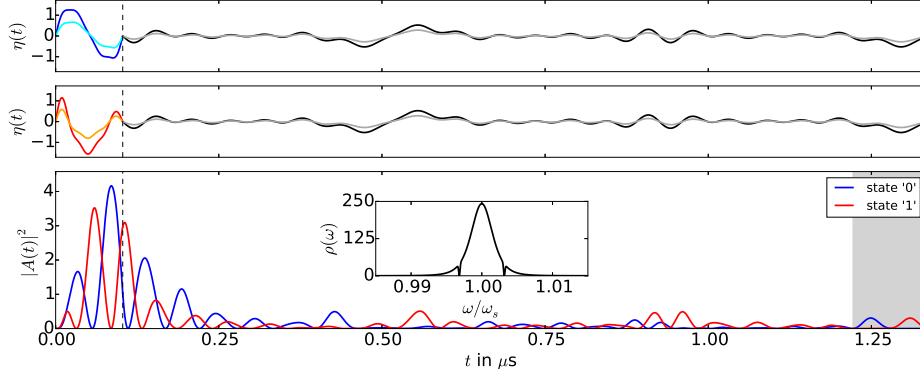


Figure 4.10: Numerical results for the time-binned cavity-responses similar to Fig. 4.5(a) but with a modified spin-density $\rho_h(\omega)$ with two holes of width $\Delta_h = 2\pi \cdot 0.7$ MHz at $\omega_s \pm \Omega$ (inset of the lower panel) and adjusted time-divisions of the writing interval $[0, 102.8$ ns], the readout interval $[102.8$ ns, 1.33 μ s] and the functional interval $[1.22$ μ s, 1.33 μ s] (gray area). The gap between the end of the writing section (vertical dashed cut) and the functional interval (gray area) is approximately 1.12 μ s.

The time-binned cavity-responses are separated almost perfectly as can be seen in Fig. 4.11(a) and the retrieved parameters γ_R and δ_R of the real-bit encoding depicted in Fig. 4.11(b) excellently agree with the initial values of γ and δ .

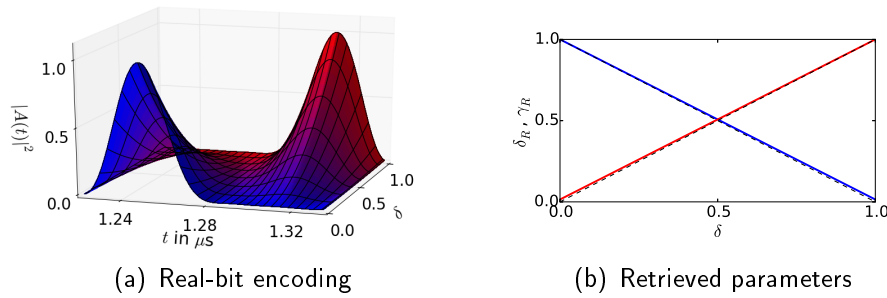


Figure 4.11: Numerical results for (a) the real-bit encoding and (b) the retrieval of the real-bit parameters γ_R (blue) and δ_R (red) similar to Fig. 4.6(b) and Fig. 4.6(d) but with reference data taken from Fig. 4.10, respectively.

Similar to Fig. 4.7 and Fig. 4.8 the retrieval of two complex-valued parameters is depicted in Fig. 4.12 and the accuracy of this retrieval-procedure, again, is only limited by the level of noise. The increased coherence properties greatly improve the storage-time of both encoding schemes due to the drastically reduced damping of the cavity-amplitude.

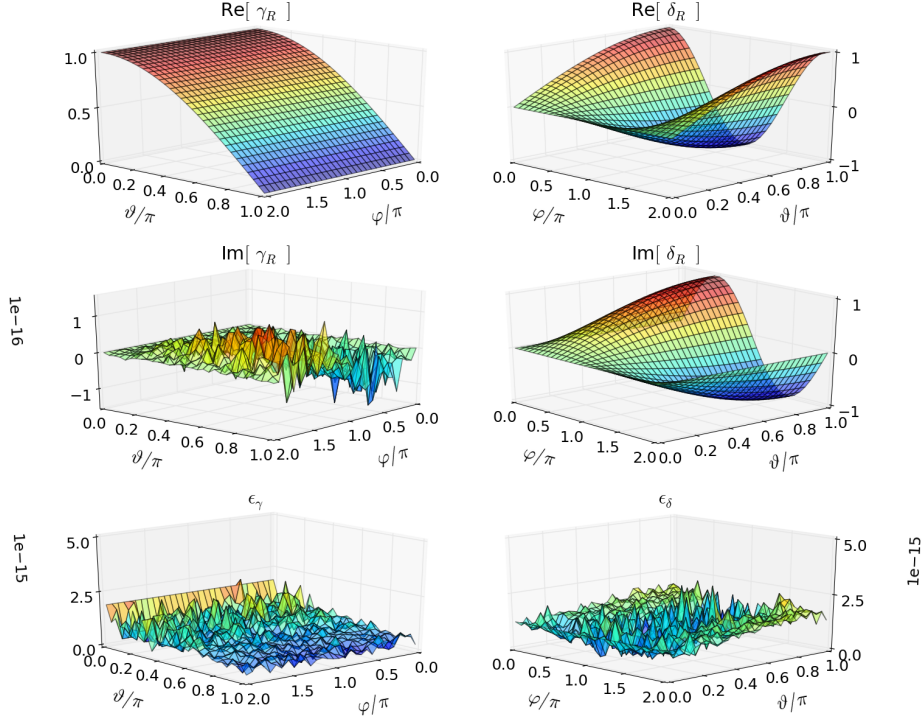


Figure 4.12: The same as Fig. 4.7 but with reference data taken from Fig. 4.10.

The harmonic pulse-coefficients are listed in Tbl. B.2 and the fundamental frequencies of the writing and the readout pulses are given by $\omega_0^{(1)} = \Omega_R/2$ and $\omega_0^{(2)} = \Omega_R/4$. The power of the reading pulse relative to the writing pulse power is adjusted to $\mathcal{P}^{(2)} < \mathcal{P}^{(1)}/2$ according to the modified time divisions compared to Sec. 4.1.2. All the other parameters used here are the same as in Fig. 4.4.

We would like to emphasize that the parameters γ_R and δ_R in Fig. 4.11 and Fig. 4.12 are retrieved solely from the cavity-amplitude in the functional interval (gray area in Fig. 4.10), which is delayed by $1.12\mu\text{s}$ from the end of the writing section (dashed cut in Fig. 4.10). In this sense we believe that we have developed a protocol to store real- and complex-valued parameters for a significant time-interval into the cavity-responses $A_{n,0}^{(2)}(t)$ and $A_{n,1}^{(2)}(t)$. Moreover the information can be reconstructed with a very high precision. In the experiment storage times of several μs should be achievable since the only limits for this encoding scheme are the level of noise and the life-time of the holes of approximately $20\mu\text{s}$.

Summary

In this thesis we start with the Volterra integral equation to describe the dynamical evolution of the amplitude of a single-mode cavity strongly coupled to an inhomogeneously broadened spin ensemble at low temperatures and in the low excitation regime [24]. We then introduce a novel way to optimally control the dynamical evolution of the cavity-amplitude of such a hybrid-quantum-system using the concept of pulse shaping [28]. More precisely we use weak control pulses, which are composed of no more than 16 Fourier modes and numerically optimize the relative amplitudes of these different harmonic components [31, 32].

Employing the Volterra integral equation we suggest a protocol, solely based on optimal control pulses, which allows us to write complex-valued parameters into the spin-cavity system and to retrieve this information at predetermined later times. Specifically, we design two optimized writing pulses, which drive the system either into the configuration "0" or "1" such that they are well-separable in time in the subsequent readout section under the action of the same optimized readout pulse.

In a next step we create coherent superpositions of the two system configurations simply by superimposing the two optimized writing pulses and applying the combined pulse to the cavity. In this sense our approach is capable of encoding information into the spin ensemble while the readout is performed with the same optimized pulse as before. Specifically, we suggest two different protocols: The first one can be used to encode one real-valued parameter into the system such that the corresponding cavity-responses in the readout section are very similar to the concept of time-binned qubits [34]. The second protocol slightly deviates from the picture of the time-binned cavity-responses but, although relying on the same optimized control pulses as before, it allows us to encode and retrieve two arbitrary complex-valued parameters, which is one qubit of information, with a precision only limited by the level of noise. Moreover, we show that the time of retrieval for both protocols can be significantly varied such that we can use the hybrid-quantum-system as a memory device for the information, which was initially written into the system.

We would like to emphasize that our description is purely linear and is based on interference effects of the field residing in the spin-cavity system with the weak optimal control pulses in contrast to other techniques based on stimulated photon echoes [35], where a combination of high-intensity and low-intensity pulses is used to store information in an optical memory and to retrieve it later on.

The applicability of our protocols can be further improved by enhancing the coherence properties of the system. This can be achieved for the hybrid-quantum-system under study by means of the cavity protection effect [10, 17], which states that certain systems can naturally be protected against decoherence if the collective coupling strength of the cavity to the whole ensemble is sufficiently large. An alternative way to drastically suppress the total decoherence rate of the system at modest values of the collective coupling strength is to modify the spectral spin-density at judiciously chosen frequencies by spectral hole burning [25]. This effect gives rise to a slow asymptotic behavior with a total decoherence rate, which is even below the fundamental lowest limit attainable by the cavity protection effect. In particular, we demonstrate that with this concept of spectral hole burning [25] storage times of $\geq 1 \mu\text{s}$ can easily be reached.

To conclude we have developed a novel protocol to optimally control a hybrid-quantum-system in the framework of linear cavity-QED, featuring a single-mode cavity strongly coupled to a large, inhomogeneously broadened spin ensemble. We especially demonstrate the applicability of such systems as a solid-state memory-devices in linear quantum circuits [2] and we believe that our approach paves the way for future applications.

Appendices

Appendix A

Harmonic Expansion of the Cavity-Amplitude

A.1 Two Subsequent Intervals

With [Eq. \(3.3\)](#) and [Eq. \(3.10\)](#) the Volterra integral equation [Eq. \(3.9\)](#) of the cavity-amplitude in the second time-interval $[T_2, T_3]$ yields

$$A^{(2)}(t) = \int_{T_2}^t d\tau \mathcal{K}(t - \tau) A^{(2)}(\tau) + \sum_{l=1}^{N_2} \alpha_l^{(2)}(t) d_l^{(2)}(t) + \sum_{k=1}^{N_1} \alpha_k^{(1)} f_k^{(2)}(t). \quad (\text{A.1})$$

Substituting the ansatz [Eq. \(3.12\)](#) for $A^{(2)}(t)$ and $A^{(2)}(\tau)$ on the left- and right hand side of [Eq. \(A.1\)](#), respectively, and rearranging everything with respect to the harmonic coefficients $\alpha_k^{(1)}$ and $\alpha_l^{(2)}$ yields

$$\sum_{k=1}^{N_1} \alpha_k^{(1)} \left\{ \psi_k^{(2)}(t) - \int_{T_2}^t d\tau \mathcal{K}(t - \tau) \psi_k^{(2)}(\tau) - f_k^{(2)}(t) \right\} = - \sum_{l=1}^{N_2} \alpha_l^{(2)} \left\{ a_l^{(2)}(t) - \int_{T_2}^t d\tau \mathcal{K}(t - \tau) a_l^{(2)}(\tau) - d_l^{(2)}(t) \right\}. \quad (\text{A.2})$$

[Eq. \(A.2\)](#) can only be satisfied for every (arbitrary) choice of the coefficients $\alpha_k^{(1)}$ and $\alpha_l^{(2)}$ if both sides are equal to zero. Moreover, this can only be true if both expressions in the curly brackets vanish separately for every $k \in \{1, 2, \dots, N_1\}$ and $l \in \{1, 2, \dots, N_2\}$. This leads to the Volterra integral description of the harmonic components of the cavity-amplitudes $\psi_k^{(2)}(t)$ and $a_l^{(2)}(t)$ introduced earlier by [Eq. \(3.13\)](#) and [Eq. \(3.14\)](#).

Appendix B

Derivations of Time-Binned Objective Functionals

B.1 Vector Notation of Variational Coefficients

Here we introduce a shorthand vector notation for the sets of complex valued coefficients $\alpha_k^{(1)}$ and $\alpha_l^{(2)}$ defined in [Eq. \(3.15\)](#) and [Eq. \(3.16\)](#) as

$$\langle \alpha^{(n)} | = \left(\alpha_1^{(n)}, \alpha_2^{(n)}, \dots, \alpha_{N_n}^{(n)} \right), \quad (\text{B.1})$$

with whom the different functionals in [Sec. 3.1.4](#) and [Sec. 3.1.5](#) can be written very instructively. The complex valued Fourier-coefficients $\alpha_k^{(n)}$ play the role of variational coefficients in the optimization procedures, which is why we also refer to $\langle \alpha^{(n)} |$ as the coefficient- or variational-vector. Analogous we introduce the amplitude-vectors for the sets of complex valued harmonic cavity-amplitudes $a_k^{(n)}(t)$ and $\psi_k^{(n)}(t)$ given by [Eq. \(3.8\)](#), [Eq. \(3.13\)](#) and [Eq. \(3.14\)](#), respectively, as

$$|a^{(n)}(t)\rangle = \left(a_1^{(n)}(t), a_2^{(n)}(t), \dots, a_{N_n}^{(n)}(t) \right)^T, \quad (\text{B.2})$$

$$|\psi^{(n)}(t)\rangle = \left(\psi_1^{(n)}(t), \psi_2^{(n)}(t), \dots, \psi_{N_n}^{(n)}(t) \right)^T, \quad (\text{B.3})$$

where $(.)^T$ is the transposed vector. We use the Dirac-bracket notation to conveniently express the hermitian conjugate of the coefficient- and amplitude-vectors $\langle . | \equiv | . \rangle^\dagger$. With this the cavity-amplitudes $A^{(1)}(t)$ and $A^{(2)}(t)$ of the form [Eq. \(3.5\)](#) and [Eq. \(3.12\)](#) can be expressed as a scalar product of the form

$$A^{(1)}(t) = \langle \alpha^{(1)} | a^{(1)}(t) \rangle, \quad (\text{B.4})$$

$$A^{(2)}(t) = \langle \alpha^{(1)} | \psi^{(2)}(t) \rangle + \langle \alpha^{(2)} | a^{(2)}(t) \rangle, \quad (\text{B.5})$$

which will be very useful to express the essential structure of the functionals introduced above.

B.2 Vector Notation of Functionals

In this section we summarize the short-hand vector notations of all functionals in [Sec. 3.1.4](#) and [Sec. 3.1.5](#). The net-power penalty functions governed by [Eq. \(3.24\)](#) and [Eq. \(3.25\)](#) can be rewritten in the following way with the vector notation given by [Eq. \(B.1\)](#)

$$\mathcal{M}_{\mathcal{P},1} [\eta^{(n)}] = \langle \alpha^{(n)} | \alpha^{(n)} \rangle - 2\mathcal{P}^{(n)} \rightarrow \min, \quad (\text{B.6})$$

$$\mathcal{M}_{\mathcal{U},2} [\eta^{(n)}] := \langle \alpha^{(n)} | \alpha^{(n)} \rangle \leq 2\mathcal{U}^{(n)}, \quad (\text{B.7})$$

which is equivalent to constraining the length of the coefficient vector $\langle \alpha^{(n)} |$, which components are the Fourier-coefficients of the control pulse $\eta^{(n)}(t)$. We can also rewrite the two basic functionals defined by [Eq. \(3.17\)](#) and [Eq. \(3.18\)](#) very instructively

$$\mathcal{M}_{\mathcal{N}} [\eta^{(1)}, \eta^{(2)}; \tau] = \langle \alpha | \mathcal{H}_{\mathcal{T}}[\tau] | \alpha \rangle - \mathcal{N}, \quad (\text{B.8})$$

$$\mathcal{L}_{\mathcal{A}} [\eta^{(1)}, \eta^{(2)}; \Delta\tau] = \langle \alpha | \mathcal{H}_{\Delta\mathcal{T}}[\Delta\tau] | \alpha \rangle - \mathcal{A}, \quad (\text{B.9})$$

with the extended, complex valued coefficient-vector $|\alpha\rangle$ defined by [Eq. \(B.23\)](#) and the two hermitian matrices $\mathcal{H}_{\mathcal{T}}[\tau]$ and $\mathcal{H}_{\Delta\mathcal{T}}[\Delta\tau]$ of dimension $N_1 + N_2 \times N_1 + N_2$ given by [Eq. \(B.22\)](#) and [Eq. \(B.27\)](#), which contain the entire information about the time-evolution of the system. Details of the derivation of [Eq. \(B.8\)](#) and [Eq. \(B.9\)](#) from [Eq. \(3.17\)](#) and [Eq. \(3.18\)](#) can be found in [Sec. B.3](#) and [Sec. B.4](#). With [Eq. \(B.8\)](#) and [Eq. \(B.9\)](#) the suppression-functional given by [Eq. \(B.10\)](#) takes the form

$$\mathcal{F}_0 [\eta^{(1)}, \eta^{(2)}; \Delta\tau_0] = \langle \alpha | \mathcal{H}_{\Delta\mathcal{T}}[\Delta\tau_0] | \alpha \rangle - \lambda_{\mathcal{T}} \langle \alpha | \mathcal{H}_{\mathcal{T}}[\tau_0] | \alpha \rangle. \quad (\text{B.10})$$

and the non-zero response functional given by [Eq. \(3.21\)](#) becomes

$$\begin{aligned} \mathcal{F}_{\mathcal{A}} [\eta^{(1)}, \eta^{(2)}; \tau_s, \Delta\tau_0, \Delta\tau_1] &= \langle \alpha | \mathcal{H}_{\Delta\mathcal{T}}[\Delta\tau_0] | \alpha \rangle - \lambda_{\mathcal{T}} \langle \alpha | \mathcal{H}_{\mathcal{T}}[\tau_s] | \alpha \rangle \\ &\quad - \lambda_{\Delta\mathcal{T}} (\langle \alpha | \mathcal{H}_{\Delta\mathcal{T}}[\Delta\tau_1] | \alpha \rangle - \mathcal{A}), \end{aligned} \quad (\text{B.11})$$

where, again, the extended coefficient vector $\langle \alpha |$ is defined by [Eq. \(B.23\)](#) and the matrices $\mathcal{H}_{\mathcal{T}}[\tau_0]$, $\mathcal{H}_{\Delta\mathcal{T}}[\Delta\tau_0]$ and $\mathcal{H}_{\Delta\mathcal{T}}[\Delta\tau_1]$ are given by [Eq. \(B.22\)](#) and [Eq. \(B.27\)](#), respectively.

The essential argument we want to emphasize by writing [Eq. \(B.6\)](#) - [Eq. \(B.11\)](#) in this vector notation is, that the complete information about the time evolution of the system for fixed time divisions $[T_1, T_2]$ and $[T_2, T_3]$ is determined by the matrices $\mathcal{H}_{\mathcal{T}}[\tau]$ and $\mathcal{H}_{\Delta\mathcal{T}}[\Delta\tau]$. They are, in turn, completely independent of the variational coefficients $\langle \alpha |$. Even the integration in [Eq. \(3.18\)](#) can be performed without specifying the coefficients. All functionals are reduced to simple vector-matrix-vector multiplications, where the matrices $\mathcal{H}_{\mathcal{T}}[\tau]$ and $\mathcal{H}_{\Delta\mathcal{T}}[\Delta\tau]$ are solely composed of complex numbers. This procedure is numerically very efficient, since a variation of the complex valued coefficient vector $\langle \alpha | = (\alpha_1^{(1)}, \dots, \alpha_{N_1}^{(1)}, \alpha_1^{(2)}, \dots, \alpha_{N_2}^{(2)})$ does not change the matrices $\mathcal{H}_{\mathcal{T}}[\tau]$ and $\mathcal{H}_{\Delta\mathcal{T}}[\Delta\tau]$, once they have been evaluated.

B.3 Equal-Time Products of Cavity-Amplitudes

To express Eq. (3.17) in terms of the variational coefficients $\alpha_k^{(n)}$ of the control pulses $\eta^{(n)}(t)$ defined by Eq. (3.1) and to provide a convenient basis for the considerations below, we here present the equal time product

$$\begin{aligned} A_i^{(1)}(t) \left(A_j^{(1)}(t) \right)^* &= \sum_{k=1}^{N_1} \alpha_k^{(1,i)} a_k^{(1)}(t) \left(\sum_{k'=1}^{N_1} \alpha_{k'}^{(1,j)} a_{k'}^{(1)}(t) \right)^*, \\ &= \sum_{k=1}^{N_1} \sum_{k'=1}^{N_1} \alpha_k^{(1,i)} \left(a_k^{(1)}(t) \left(a_{k'}^{(1)}(t) \right)^* \right) \left(\alpha_{k'}^{(1,j)} \right)^*, \end{aligned} \quad (\text{B.12})$$

of the two cavity-amplitudes

$$A_i^{(1)}(t) = \sum_{k=1}^{N_1} \alpha_k^{(1,i)} a_k^{(1)}(t), \quad A_j^{(1)}(t) = \sum_{k'=1}^{N_1} \alpha_{k'}^{(1,j)} a_{k'}^{(1)}(t), \quad (\text{B.13})$$

where the evolution of $a_k^{(1)}(t)$ is defined by Eq. (3.8). $A_i^{(1)}(t)$ and $A_j^{(1)}(t)$ are controlled by the two independent pulses $\eta_i^{(1)}(t)$ and $\eta_j^{(1)}(t)$ with N_1 coefficients $\alpha_k^{(1,i)}$ and $\alpha_{k'}^{(1,j)}$ each, which correspond to those of Eq. (3.15). In the last line of Eq. (B.12) we can see that the product $A_i^{(1)}(t)(A_j^{(1)}(t))^*$ can be treated as a matrix with elements $a_k^{(1)}(t)(a_{k'}^{(1)}(t))^*$ sandwiched by the coefficient vectors $(\langle \alpha^{(1,i)} |)_k$ and $(| \alpha^{(1,j)} \rangle)_{k'}$ defined by Eq. (B.1). With the Dirac notation Eq. (B.1)–Eq. (B.3) we define the equal time matrix

$$\mathcal{T} [b^{(n)}, c^{(m)}; t] = \begin{pmatrix} b_1^{(n)}(t) \left(c_1^{(m)}(t) \right)^* & \dots & b_1^{(n)}(t) \left(c_{N_m}^{(m)}(t) \right)^* \\ b_2^{(n)}(t) \left(c_1^{(m)}(t) \right)^* & \dots & b_2^{(n)}(t) \left(c_{N_m}^{(m)}(t) \right)^* \\ \vdots & \ddots & \vdots \\ b_{N_n}^{(n)}(t) \left(c_1^{(m)}(t) \right)^* & \dots & b_{N_n}^{(n)}(t) \left(c_{N_m}^{(m)}(t) \right)^* \end{pmatrix} \quad (\text{B.14})$$

$$\equiv |b^{(n)}(t)\rangle \langle c^{(m)}(t)|. \quad (\text{B.15})$$

as the dyadic-product of two sets of cavity-amplitudes $|b^{(n)}(t)\rangle$ and $\langle c^{(m)}(t)| = |c^{(m)}(t)\rangle^\dagger$ defined in the time interval n and m , respectively. Depending on the actual problem the cavity-amplitudes $b_k^{(n)}(t)$ and $c_i^{(m)}(t)$, which form the matrix elements, are determined by any of the harmonic cavity-amplitudes $a_k^{(1)}(t)$, $\psi_k^{(2)}(t)$ or $a_l^{(2)}(t)$ governed by Eq. (3.8), Eq. (3.13) or Eq. (3.14), respectively. With Eq. (B.1) and Eq. (B.14) we can bring Eq. (B.12) to the very instructive form

$$A_i^{(1)}(t) \left(A_j^{(1)}(t) \right)^* = \langle \alpha^{(1,i)} | \underbrace{\mathcal{T} [a^{(1)}, a^{(1)}; t]}_{|a^{(1)}(t)\rangle \langle a^{(1)}(t)|} | \alpha^{(1,j)} \rangle. \quad (\text{B.16})$$

Evaluating the equal time product in a second, subsequent time interval, regarding Eq. (3.17), is slightly more complicated. Using two independently controllable cavity-amplitudes determined analogous to Eq. (3.12) by

$$\begin{aligned} A_i^{(2)}(t) &= \sum_{k=1}^{N_1} \alpha_k^{(1,i)} \psi_k^{(2)}(t) + \sum_{l=1}^{N_2} \alpha_l^{(2,i)} a_l^{(2)}(t), \\ A_j^{(2)}(t) &= \sum_{k'=1}^{N_1} \alpha_{k'}^{(1,j)} \psi_{k'}^{(2)}(t) + \sum_{l'=1}^{N_2} \alpha_{l'}^{(2,j)} a_{l'}^{(2)}(t), \end{aligned} \quad (\text{B.17})$$

we need to consider four control pulses $\eta_i^{(1)}(t)$, $\eta_i^{(2)}(t)$, $\eta_j^{(1)}(t)$ and $\eta_j^{(2)}(t)$ of the type of Eq. (3.1) with $2 \cdot (N_1 + N_2)$ corresponding variational coefficients $\alpha_k^{(1,i)}$, $\alpha_l^{(2,i)}$, $\alpha_{k'}^{(1,j)}$ and $\alpha_{l'}^{(2,j)}$ in general. The functions $\psi_k^{(2)}(t)$ and $a_l^{(2)}(t)$ are determined by Eq. (3.13) and Eq. (3.14) and are the same for both cavity-amplitudes $A_i^{(2)}(t)$ and $A_j^{(2)}(t)$. For the product of $A_i^{(2)}(t)$ and $A_j^{(2)}(t)$ we get

$$\begin{aligned} A_i^{(2)}(t) \left(A_j^{(2)}(t) \right)^* &= \\ & \underbrace{\left(\sum_{k=1}^{N_1} \alpha_k^{(1,i)} \psi_k^{(2)}(t) + \sum_{l=1}^{N_2} \alpha_l^{(2,i)} a_l^{(2)}(t) \right)}_{A_i^{(2)}(t) \equiv \langle \alpha^{(1,i)} | \psi^{(2)}(t) \rangle + \langle \alpha^{(2,i)} | a^{(2)}(t) \rangle} \underbrace{\left(\sum_{k'=1}^{N_1} \alpha_{k'}^{(1,j)} \psi_{k'}^{(2)}(t) + \sum_{l'=1}^{N_2} \alpha_{l'}^{(2,j)} a_{l'}^{(2)}(t) \right)^*}_{\left(A_i^{(2)}(t) \right)^* \equiv \langle \psi^{(2)}(t) | \alpha^{(1,j)} \rangle + \langle a^{(2)}(t) | \alpha^{(2,j)} \rangle}. \end{aligned} \quad (\text{B.18})$$

With the Dirac notation for $A_i^{(2)}(t)$ and $A_j^{(2)}(t)$ given by Eq. (B.5) (which is indicated in Eq. (B.18)) and after rearranging everything with respect to the variational coefficients, Eq. (B.18) yields

$$\begin{aligned} A_i^{(2)}(t) \left(A_j^{(2)}(t) \right)^* &= \langle \alpha^{(1,i)} | \psi^{(2)}(t) \rangle \langle \psi^{(2)}(t) | \alpha^{(1,j)} \rangle \\ &+ \langle \alpha^{(1,i)} | \psi^{(2)}(t) \rangle \langle a^{(2)}(t) | \alpha^{(2,j)} \rangle \\ &+ \langle \alpha^{(2,i)} | a^{(2)}(t) \rangle \langle \psi^{(2)}(t) | \alpha^{(1,j)} \rangle \\ &+ \langle \alpha^{(2,i)} | a^{(2)}(t) \rangle \langle a^{(2)}(t) | \alpha^{(2,j)} \rangle, \end{aligned} \quad (\text{B.19})$$

which can also be written with the equal-time matrix notation defined by Eq. (B.14). For $i = j$ we consider two subsequent pulses $\eta^{(1)}(t)$ and $\eta^{(2)}(t)$ with $N_1 + N_2$ coefficients $\alpha_k^{(1)} = \alpha_k^{(1,i)} = \alpha_k^{(1,j)}$ and $\alpha_l^{(2)} = \alpha_l^{(2,i)} = \alpha_l^{(2,j)}$. Consequently Eq. (3.17) can be written in the form

$$\mathcal{M}_{\mathcal{N}} [\eta^{(1)}, \eta^{(2)}; t] = \langle \alpha^{(1)} | \mathcal{T} [\psi^{(2)}, \psi^{(2)}; t] | \alpha^{(1)} \rangle \quad (\text{B.20})$$

$$\begin{aligned} &+ \langle \alpha^{(1)} | \mathcal{T} [\psi^{(2)}, a^{(2)}; t] | \alpha^{(2)} \rangle \\ &+ \langle \alpha^{(2)} | \mathcal{T} [a^{(2)}, \psi^{(2)}; t] | \alpha^{(1)} \rangle \\ &+ \langle \alpha^{(2)} | \mathcal{T} [a^{(2)}, a^{(2)}; t] | \alpha^{(2)} \rangle - \mathcal{N}. \end{aligned} \quad (\text{B.21})$$

where all time dependencies $\mathcal{T}[\dots; t]$ can be evaluated without specification of the variational vectors $\langle \alpha^{(1)} |$ and $\langle \alpha^{(2)} |$. Eq. (B.21) can even be written in a more sophisticated way, that is

$$\mathcal{M}_{\mathcal{N}} [\eta^{(1)}, \eta^{(2)}; t] = \langle \alpha^{(1)} |, \langle \alpha^{(2)} | \underbrace{\left(\begin{array}{cc} \mathcal{T} [\psi^{(2)}, \psi^{(2)}; t] & \mathcal{T} [\psi^{(2)}, a^{(2)}; t] \\ \mathcal{T} [a^{(2)}, \psi^{(2)}; t] & \mathcal{T} [a^{(2)}, a^{(2)}; t] \end{array} \right)}_{\mathcal{H}_{\mathcal{T}}[t]} \begin{pmatrix} |\alpha^{(1)}\rangle \\ |\alpha^{(2)}\rangle \end{pmatrix} - \mathcal{N} \quad (\text{B.22})$$

where we introduce the extended coefficient vector

$$\langle \alpha | = (\langle \alpha^{(1)} |, \langle \alpha^{(2)} |) = (\alpha_1^{(1)}, \dots, \alpha_{N_1}^{(1)}, \alpha_1^{(2)}, \dots, \alpha_{N_2}^{(2)}) \quad (\text{B.23})$$

and the extended equal-time matrix $\mathcal{H}_{\mathcal{T}}[t]$. The variation of the two pulses $\eta^{(1)}(t)$ and $\eta^{(2)}(t)$ are performed very efficiently by varying the coefficients $\alpha_k^{(1)}$ and $\alpha_l^{(2)}$.

B.4 Time-Integrated Products of Cavity-Amplitudes

Regarding Eq. (3.18) we integrate the equal time products defined by Eq. (B.12) and Eq. (B.18) of two cavity-amplitudes $A_i^{(n)}(t)$ and $A_j^{(n)}(t)$ given by Eq. (B.13) and Eq. (B.17) in the time interval $n = 1$ and $n = 2$, respectively. With Eq. (B.16) and Eq. (B.19) we immediately find

$$\int_{\tau}^{\tau'} dt A_i^{(1)}(t) \left(A_j^{(1)}(t) \right)^* = \langle \alpha^{(1,i)} | \left(\int_{\tau}^{\tau'} dt \mathcal{T} [a^{(1)}, a^{(1)}; t] \right) |\alpha^{(1,j)}\rangle, \quad (\text{B.24})$$

$$\begin{aligned} \int_{\tau}^{\tau'} dt A_i^{(2)}(t) \left(A_j^{(2)}(t) \right)^* &= \langle \alpha^{(1,i)} | \left(\int_{\tau}^{\tau'} dt \mathcal{T} [\psi^{(2)}, \psi^{(2)}; t] \right) |\alpha^{(1,j)}\rangle \\ &+ \langle \alpha^{(1,i)} | \left(\int_{\tau}^{\tau'} dt \mathcal{T} [\psi^{(2)}, a^{(2)}; t] \right) |\alpha^{(2,j)}\rangle \\ &+ \langle \alpha^{(2,i)} | \left(\int_{\tau}^{\tau'} dt \mathcal{T} [a^{(2)}, \psi^{(2)}; t] \right) |\alpha^{(1,j)}\rangle \\ &+ \langle \alpha^{(2,i)} | \left(\int_{\tau}^{\tau'} dt \mathcal{T} [a^{(2)}, a^{(2)}; t] \right) |\alpha^{(2,j)}\rangle. \quad (\text{B.25}) \end{aligned}$$

The matrix elements of $\mathcal{T}[\cdot, \cdot; t]$ defined in Eq. (B.14) are uniquely defined by the evolution of $a_k^{(1)}(t)$, $\psi_k^{(2)}(t)$ and $a_l^{(2)}(t)$. Thus every single matrix element of $\mathcal{T}[\cdot, \cdot; t]$ can be evaluated and moreover can be integrated before evaluating the full expressions Eq. (B.24) and Eq. (B.25) by specifying the coefficient $\alpha_k^{(n,i)}$ and $\alpha_{k'}^{(n,j)}$. We therefore define the following matrix, where all integrations in the interval $\Delta\tau \equiv [\tau, \tau']$ of the equal-time matrix are carried out

$$\begin{aligned} \mathcal{I}[b^{(n)}, c^{(m)}; \Delta\tau] &= \int_{\tau}^{\tau'} dt \mathcal{T}[b^{(n)}, c^{(m)}; t] \\ &= \begin{pmatrix} \int_{\tau}^{\tau'} dt b_1^{(n)}(t) (c_1^{(m)}(t))^* & \dots & \int_{\tau}^{\tau'} dt b_1^{(n)}(t) (c_{N_m}^{(m)}(t))^* \\ \int_{\tau}^{\tau'} dt b_2^{(n)}(t) (c_1^{(m)}(t))^* & \dots & \int_{\tau}^{\tau'} dt b_2^{(n)}(t) (c_{N_m}^{(m)}(t))^* \\ \vdots & \ddots & \vdots \\ \int_{\tau}^{\tau'} dt b_{N_n}^{(n)}(t) (c_1^{(m)}(t))^* & \dots & \int_{\tau}^{\tau'} dt b_{N_n}^{(n)}(t) (c_{N_m}^{(m)}(t))^* \end{pmatrix}. \end{aligned} \quad (\text{B.26})$$

The dummy cavity-amplitudes $b_k^{(n)}(t)$ and $c_l^{(m)}(t)$ in Eq. (B.26) can be any of the harmonic cavity-amplitudes $a_k^{(1)}(t)$, $\psi_k^{(2)}(t)$ or $a_l^{(2)}(t)$, respectively, depending on the actual problem. Analogous to the functional $\mathcal{M}_{\mathcal{N}}[\eta^{(1)}, \eta^{(2)}; t]$ above the functional $\mathcal{L}_{\mathcal{A}}[\eta^{(1)}, \eta^{(2)}; \Delta\tau]$ given by Eq. (3.18) can be rewritten with Eq. (B.26) as

$$\mathcal{L}_{\mathcal{A}}[\eta^{(1)}, \eta^{(2)}; \Delta\tau] = \langle \alpha | \underbrace{\begin{pmatrix} \mathcal{I}[\psi^{(2)}, \psi^{(2)}; \Delta\tau] & \mathcal{I}[\psi^{(2)}, a^{(2)}; \Delta\tau] \\ \mathcal{I}[a^{(2)}, \psi^{(2)}; \Delta\tau] & \mathcal{I}[a^{(2)}, a^{(2)}; \Delta\tau] \end{pmatrix}}_{\mathcal{H}_{\Delta\tau}[\Delta\tau]} | \alpha \rangle - \mathcal{A}, \quad (\text{B.27})$$

where we use the extended coefficient vector $\langle \alpha |$ defined by Eq. (B.23) and we define the matrix $\mathcal{H}_{\Delta\tau}[\Delta\tau]$. Optimization procedures involving Eq. (B.27) can thus be performed very efficiently by variation of the coefficient vector $\langle \alpha |$.

B.5 Numerical Results of Harmonic Coefficients

Tbl. B.1 and Tbl. B.2 list all coefficients of the optimal control pulses $\eta_{0''}^{(1)}(t)$, $\eta_{1''}^{(1)}(t)$ and $\eta_{\mathcal{R}}^{(2)}(t)$ defined by Eq. (4.1), Eq. (4.2) and Eq. (4.5), which are presented in this thesis.

	Fig. 4.4(a)	Fig. 4.4(b)	Fig. 4.5(a)	Fig. 4.5(b)
$\alpha_1^{0''}$	$-0.386 + 0.718 i$	$0.509 - 0.832 i$	$-1.964 + 0.055 i$	$1.869 + 0.698 i$
$\alpha_2^{0''}$	$0.184 - 0.229 i$	$0.435 - 0.711 i$	$0.149 + 0.300 i$	$-0.126 - 0.047 i$
$\alpha_3^{0''}$	$0.724 - 1.095 i$	$0.600 - 0.981 i$	$-0.022 - 0.037 i$	$0.011 + 0.005 i$
$\alpha_4^{0''}$	$-0.208 + 0.329 i$	$-0.053 + 0.086 i$	$0.015 + 0.120 i$	$-0.001 - 0.001 i$
$\alpha_5^{0''}$	$0.477 - 0.745 i$	$0.417 - 0.681 i$	$-0.009 - 0.020 i$	$0.003 + 0.000 i$
$\alpha_6^{0''}$	$-0.176 + 0.272 i$	$-0.069 + 0.113 i$	$0.006 + 0.077 i$	$0.003 + 0.001 i$
$\alpha_7^{0''}$	$0.347 - 0.550 i$	$0.309 - 0.506 i$	$-0.007 - 0.014 i$	$0.002 + 0.000 i$
$\alpha_8^{0''}$	$-0.134 + 0.218 i$	$-0.061 + 0.099 i$	$0.003 + 0.057 i$	$0.003 + 0.001 i$
$\alpha_1^{1''}$	$-0.010 + 0.028 i$	$-0.007 + 0.011 i$	$0.174 - 0.148 i$	$-0.107 - 0.042 i$
$\alpha_2^{1''}$	$-0.229 + 0.504 i$	$-0.322 + 0.527 i$	$1.043 + 0.238 i$	$-0.627 - 0.309 i$
$\alpha_3^{1''}$	$-0.764 + 1.182 i$	$-0.730 + 1.194 i$	$0.970 - 0.030 i$	$1.122 + 0.041 i$
$\alpha_4^{1''}$	$0.068 - 0.247 i$	$0.155 - 0.253 i$	$0.096 + 0.089 i$	$-0.381 - 0.128 i$
$\alpha_5^{1''}$	$-0.560 + 0.810 i$	$-0.504 + 0.824 i$	$0.837 - 0.016 i$	$1.019 + 0.023 i$
$\alpha_6^{1''}$	$0.042 - 0.225 i$	$0.142 - 0.232 i$	$0.721 + 0.057 i$	$0.112 - 0.083 i$
$\alpha_7^{1''}$	$-0.473 + 0.600 i$	$-0.374 + 0.611 i$	$0.786 - 0.011 i$	$0.967 + 0.016 i$
$\alpha_8^{1''}$	$-0.083 - 0.185 i$	$0.117 - 0.191 i$	$0.022 + 0.042 i$	$-0.282 - 0.061 i$
$\alpha_1^{\mathcal{R}}$	$-0.063 + 0.106 i$	$-0.159 + 0.259 i$	$-0.178 - 0.032 i$	$0.475 + 0.177 i$
$\alpha_2^{\mathcal{R}}$	$-0.112 + 0.207 i$	$0.170 - 0.278 i$	$-0.166 - 0.002 i$	$0.209 + 0.078 i$
$\alpha_3^{\mathcal{R}}$	$-0.098 + 0.179 i$	$0.043 - 0.071 i$	$0.321 + 0.059 i$	$0.018 + 0.007 i$
$\alpha_4^{\mathcal{R}}$	$0.004 + 0.001 i$	$-0.045 + 0.074 i$	$0.312 + 0.064 i$	$-0.175 - 0.065 i$
$\alpha_5^{\mathcal{R}}$	$0.079 - 0.151 i$	$-0.032 + 0.053 i$	$-0.099 + 0.042 i$	$0.030 + 0.011 i$
$\alpha_6^{\mathcal{R}}$	$0.098 - 0.184 i$	$0.060 - 0.098 i$	$0.259 - 0.040 i$	$0.037 + 0.014 i$
$\alpha_7^{\mathcal{R}}$	$0.089 - 0.162 i$	$0.022 - 0.036 i$	$-0.227 + 0.036 i$	$-0.045 - 0.017 i$
$\alpha_8^{\mathcal{R}}$	$0.021 - 0.050 i$	$-0.024 + 0.040 i$	$0.161 + 0.022 i$	$-0.134 - 0.050 i$
$\alpha_9^{\mathcal{R}}$	$-0.102 + 0.191 i$	$-0.027 + 0.043 i$	$0.268 - 0.003 i$	$-0.049 - 0.018 i$
$\alpha_{10}^{\mathcal{R}}$	$-0.168 + 0.310 i$	$0.037 - 0.060 i$	$-0.283 + 0.019 i$	$-0.030 - 0.011 i$
$\alpha_{11}^{\mathcal{R}}$	$-0.058 + 0.102 i$	$0.020 - 0.033 i$	$0.090 - 0.005 i$	$-0.099 - 0.037 i$
$\alpha_{12}^{\mathcal{R}}$	$0.055 - 0.096 i$	$-0.018 + 0.029 i$	$0.119 + 0.010 i$	$-0.141 - 0.053 i$
$\alpha_{13}^{\mathcal{R}}$	$-0.006 + 0.002 i$	$-0.024 + 0.040 i$	$-0.008 + 0.022 i$	$-0.103 - 0.039 i$
$\alpha_{14}^{\mathcal{R}}$	$0.056 - 0.102 i$	$0.028 - 0.046 i$	$0.236 - 0.024 i$	$-0.078 - 0.029 i$
$\alpha_{15}^{\mathcal{R}}$	$0.295 - 0.547 i$	$0.019 - 0.031 i$	$-0.495 + 0.041 i$	$-0.148 - 0.055 i$
$\alpha_{16}^{\mathcal{R}}$	$-0.205 + 0.373 i$	$-0.018 + 0.029 i$	$-0.305 + 0.025 i$	$-0.151 - 0.056 i$

Table B.1: Harmonic coefficients of the optimal control pulses $\eta_{0''}^{(1)}(t)$, $\eta_{1''}^{(1)}(t)$ and $\eta_{\mathcal{R}}^{(2)}(t)$ defined by Eq. (4.1), Eq. (4.2) and Eq. (4.5) for the time-binned cavity-responses depicted in Fig. 4.4(a), Fig. 4.4(b), Fig. 4.5(a) and Fig. 4.5(b).

	Fig. 4.9(a)	Fig. 4.10
$\alpha_1^{0''}$	$0.551 - 0.132 i$	$0.121 + 0.093 i$
$\alpha_2^{0''}$	$1.219 - 0.120 i$	$1.228 + 0.637 i$
$\alpha_3^{0''}$	$-0.028 - 0.019 i$	$0.039 - 0.002 i$
$\alpha_4^{0''}$	$0.928 + 0.069 i$	$0.173 + 0.089 i$
$\alpha_5^{0''}$	$0.435 - 0.036 i$	$-0.009 - 0.014 i$
$\alpha_6^{0''}$	$0.592 + 0.049 i$	$0.104 + 0.057 i$
$\alpha_7^{0''}$	$0.765 - 0.029 i$	$-0.009 - 0.011 i$
$\alpha_8^{0''}$	$0.422 + 0.037 i$	$0.077 + 0.039 i$
$\alpha_1^{1''}$	$1.820 + 0.065 i$	$-0.915 - 0.467 i$
$\alpha_2^{1''}$	$0.099 + 0.004 i$	$0.055 + 0.001 i$
$\alpha_3^{1''}$	$0.558 + 0.053 i$	$0.744 + 0.378 i$
$\alpha_4^{1''}$	$-0.105 - 0.039 i$	$0.177 + 0.091 i$
$\alpha_5^{1''}$	$0.456 + 0.033 i$	$0.323 + 0.168 i$
$\alpha_6^{1''}$	$0.159 - 0.027 i$	$0.093 + 0.052 i$
$\alpha_7^{1''}$	$0.308 + 0.024 i$	$0.209 + 0.112 i$
$\alpha_8^{1''}$	$0.129 - 0.020 i$	$0.066 + 0.037 i$
$\alpha_1^{\mathcal{R}}$	$0.506 + 0.004 i$	$-0.033 - 0.018 i$
$\alpha_2^{\mathcal{R}}$	$-0.357 + 0.153 i$	$0.101 + 0.052 i$
$\alpha_3^{\mathcal{R}}$	$-0.568 + 0.010 i$	$-0.103 - 0.057 i$
$\alpha_4^{\mathcal{R}}$	$-0.237 + 0.028 i$	$0.135 + 0.071 i$
$\alpha_5^{\mathcal{R}}$	$-0.288 + 0.008 i$	$-0.083 - 0.047 i$
$\alpha_6^{\mathcal{R}}$	$-0.060 + 0.062 i$	$0.043 + 0.022 i$
$\alpha_7^{\mathcal{R}}$	$0.135 - 0.033 i$	$-0.055 - 0.028 i$
$\alpha_8^{\mathcal{R}}$	$-0.054 - 0.008 i$	$-0.020 - 0.008 i$
$\alpha_9^{\mathcal{R}}$	$0.014 + 0.019 i$	$-0.051 - 0.027 i$
$\alpha_{10}^{\mathcal{R}}$	$0.085 + 0.008 i$	$-0.001 + 0.001 i$
$\alpha_{11}^{\mathcal{R}}$	$-0.175 - 0.010 i$	$-0.064 - 0.032 i$
$\alpha_{12}^{\mathcal{R}}$	$-0.184 + 0.045 i$	$-0.045 - 0.021 i$
$\alpha_{13}^{\mathcal{R}}$	$0.059 - 0.031 i$	$-0.026 - 0.011 i$
$\alpha_{14}^{\mathcal{R}}$	$-0.106 + 0.051 i$	$-0.103 - 0.051 i$
$\alpha_{15}^{\mathcal{R}}$	$-0.017 - 0.035 i$	$-0.009 - 0.000 i$
$\alpha_{16}^{\mathcal{R}}$	$0.086 + 0.013 i$	$0.002 + 0.004 i$

Table B.2: Harmonic coefficients of the optimal control pulses $\eta_{s_0''}^{(1)}(t)$, $\eta_{s_1''}^{(1)}(t)$ and $\eta_{\mathcal{R}}^{(2)}(t)$ defined by Eq. (4.1), Eq. (4.2) and Eq. (4.5) for the time-binned cavity-responses depicted in Fig. 4.9(a) and Fig. 4.10.

Appendix C

Refocusing of Cavity-Amplitudes and Spin-Waves

C.1 Concept, Results and Discussion

Based on the discussion of the time-binned cavity-responses of [Sec. 4.1](#) we here investigate the capability of a single storage pulse $\eta_S^{(2')}(t)$ being applied in between the writing interval $[T_1, T_2]$ and the readout interval $[T_{3'}, T_{4'}] = [T_2 + \Delta T_S, T_3 + \Delta T_S]$, which is delayed by a storage time ΔT_S . The primed quantities denote the adjusted time-divisions because of the intermediate storage pulse; [Fig. C.1](#) schematically depicts this modified time-divisions.

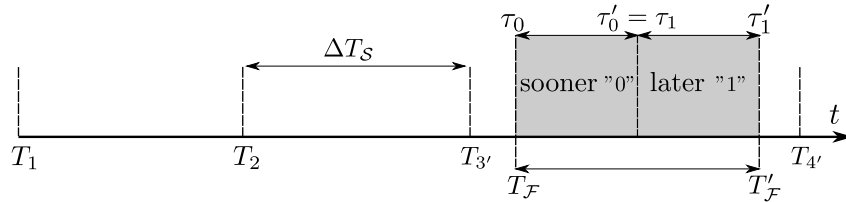


Figure C.1: Time-divisions of the optimization scheme for the refocusing of time-binned cavity-responses sketched in [Fig. 4.1](#). The writing interval $[T_1, T_2]$ is followed by the storage interval $[T_2, T_{3'}]$. The other time-divisions are the same as depicted in [Fig. 4.3](#) but delayed by the storage time ΔT_S .

This protocol aims to restore a snapshot of the configuration of the coupled system at the end of the writing interval T_2 to restore it at the end of the storage interval $T_{3'} = T_2 + \Delta T_S$, independently of which pulse $\eta_{n_0}^{(1)}(t)$ or $\eta_{n_1}^{(1)}(t)$ has initially been applied. Subsequently, the delayed readout pulse $\eta_{\mathcal{R}}^{(3')}(t) \equiv \eta_{\mathcal{R}}^{(2)}(t - \Delta T_S)$ is applied, which corresponds to the two writing pulses $\eta_{n_0}^{(1)}(t)$ and $\eta_{n_1}^{(1)}(t)$ by means of the time-binned optimization procedure of [Sec. 4.1.1](#). The cavity-response to this delayed readout pulse should be equivalent to the time-binned cavity-response as if the readout pulse $\eta_{\mathcal{R}}^{(2)}(t)$ is directly applied after the writing interval. To achieve this behavior, we have to consider both, the cavity-amplitudes $A_{n_i}^{(1)}(T_2)$ as well as the

spin-wave amplitudes $B_{i',k}^{(1)}(T_2)$ defined by Eq. (2.11) for both states " i " = " 0 ", " 1 " at time T_2 (vertical dashed cut in Fig. 4.4(a) and Fig. 4.4(b)) and restore the respective configuration at $T_2 + \Delta T_S$. The analytical and numerical treatment of this protocol is carried out in detail in Appendix C.2 and Appendix C.3. We here only define the storage pulse analogous to Eq. (3.1) as

$$\eta_S^{(2')}(t) = \sum_{q=1}^{N_{2'}} \alpha_q^S \sin(q \omega_0^S (t - T_2)), \quad (\text{C.1})$$

with the fundamental frequency ω_0^S and the $N_{2'}$ harmonic coefficients α_q^S . Fig. C.2(a) presents the results for the cavity-amplitudes $A_{i'}^{(n)}(t)$ and $A_{i'}^{(n)}(t)$, probed with the predefined writing pulses $\eta_{i'}^{(1)}(t)$ and $\eta_{i'}^{(1)}(t)$ in the first interval ($n = 1$), the optimized storage pulse $\eta_S^{(2')}(t)$ in the second interval ($n = 2'$) and the delayed, predefined readout pulse $\beta \eta_{\mathcal{R}}^{(3')}(t)$ in the third interval ($n = 3'$). The predefined writing pulses and readout pulse are taken from Fig. 4.4(a). The parameter β accounts for a potential total damping and a global phase-shift of the reconstructed cavity-amplitudes and spin-wave amplitudes at the end of the storage interval compared to their initial values and is included in the functional evaluation of $\eta_S^{(2')}(t)$ (see Eq. (C.5) and Eq. (C.6) for details). The storage pulse presented in Fig. C.2(a) contains $N_{2'} = 16$ harmonic components, which are listed in Tbl. C.1, has a fundamental frequency of $\omega_0^S = \Omega_R/2$ and its pulse power is limited by $\mathcal{P}^{(2')} < \mathcal{P}^{(1)}/2$, where $\mathcal{P}^{(1)}$ is the power of the writing pulses. The storage interval of $\Delta T_S = 102.8$ ns is the same as for the delayed readout-time in Fig. 4.5(a). Further, in Fig. C.2(b) we give a detailed presentation of the restored cavity-amplitudes in the delayed functional interval $[T_{\mathcal{F}} + \Delta T_S, T_{\mathcal{F}}' + \Delta T_S]$ (gray area in Fig. C.2(a)) and compare them to their respective original shape $\beta A_{i'}^{(2)}(t)$ and $\beta A_{i'}^{(2)}(t)$ (gray area in Fig. 4.4(a)). Besides a considerable decrease in amplitude of the restored time-binned responses by a factor of $\beta = 0.3 + i0.03$ compared to Fig. 4.4(a), the relative amplitudes and phases are restored with good accuracy. Further we can see in the last line of Fig. C.2(b) that the time-binned nature of the cavity-responses is preserved quite well, although the two basis states slightly begin to overlap owing to decoherence processes. It should be noted that in the evaluation of $\eta_{i'}^{(1)}(t)$, $\eta_{i'}^{(1)}(t)$ and $\eta_{\mathcal{R}}^{(2)}(t)$ depicted in Fig. 4.4(a) we constrain the cavity-amplitudes for both states to vanish at the end of the writing interval $A_{i'}^{(1)}(T_2) = 0$ and $A_{i'}^{(1)}(T_2) = 0$. Thus, at this moment of time T_2 the complete information about the writing pulses is hidden in the spin ensemble and the restored states in Fig. C.2 are solely based on the spin-wave-amplitudes $B_{i',k}^{(1)}(T_2)$ and $B_{i',k}^{(1)}(T_2)$. This is in contrast to Fig. 4.5(a), where we also see a cavity content at $t = T_2$. However, we can already learn from Eq. (4.6) and Eq. (4.7), that the respective information-carrying part of the cavity-amplitude $\tilde{A}_{i'}^{(n>1)}(t)$ after the writing interval ($n = 1$) can not be manipulated by a readout-pulse or a storage pulse for any state " i " = " 0 ", " 1 " in the

linear regime. The partial readout amplitude $\tilde{A}_{\mathcal{R}}^{(n>1)}(t)$ (and equivalently the storage amplitude $\tilde{A}_{\mathcal{S}}^{(n>1)}(t)$ defined in Eq. (C.2) and Eq. (C.10)) evolve separately from $\tilde{A}_{i'}^{(n>1)}(t)$. Both the storage and the readout part interfere with $\tilde{A}_{i'}^{(3')}(t)$ leading to an optimized time-binned response in the respective time-interval but they can not refocus or enhance the memory-part. This is where the damping of the amplitudes in Fig. C.2 comes from, which thus limits the applicability of this procedure.

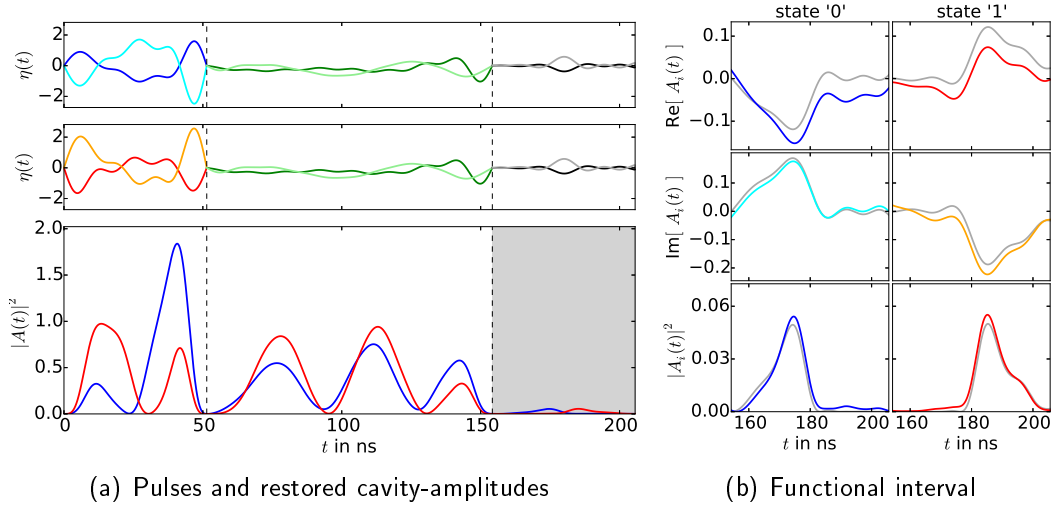


Figure C.2: (a) is the same as Fig. 4.4(a) but with a rescaled and delayed readout pulse $\beta \eta_{\mathcal{R}}^{(2)}(t - \Delta T_S)$ and an unique intermediate storage pulse $\eta_S^{(2')}(t)$ given by Eq. (C.1) shown in the upper two rows (real-part: green, imaginary-part: light green) applied between the dashed vertical cuts, respectively. Panel (b) shows the time-binned responses $A_{i'}^{(3')}(t)$ defined by Eq. (C.10) in the functional interval (gray area in (a)) for "i" = "0", "1" in detail. The real part (first row), the imaginary part (second row) and the absolute value squared (third row) for state "0" (real-part: blue, imaginary-part: cyan) and state "1" (real-part: red, imaginary-part: orange) are compared to the rescaled reference amplitudes $\beta A_{i'}^{(2)}(t)$ from Fig. 4.4(a) (gray lines in (b)), respectively.

C.2 Functional Analysis in Storage Interval

To restore a snapshot of the state of the coupled system from the end of the writing interval T_2 at the end of the storage interval $T_{3'} = T_2 + \Delta T_S$ regardless of which pulse $\eta_{i'}^{(1)}(t)$ or $\eta_{i''}^{(1)}(t)$ has initially been applied, we have to consider the cavity-amplitudes and the spin-wave amplitudes for both states "i" = "0", "1", respectively. Analogous to Eq. (4.6) and Eq. (4.7) the cavity-amplitudes in the

storage interval take the form

$$A_{n,i''}^{(2')}(t) = \tilde{A}_{n,i''}^{(2')}(t) + \underbrace{\sum_{q=1}^{N_{2'}} \alpha_q^S a_q^{(2')}(t)}_{\tilde{A}_S^{(2')}(t)} \quad (\text{C.2})$$

for " $i'' = 0, 1$ ". The partial cavity-amplitudes $\tilde{A}_{n,i''}^{(2')}(t)$ are defined in Eq. (4.6) and Eq. (4.7) and continue the evolution of the respective cavity-amplitude of the first interval $A_{n,i''}^{(1)}(t)$ defined by Eq. (4.3) and Eq. (4.4). The partial storage amplitude $\tilde{A}_S^{(2')}(t)$ is similar to the partial readout amplitude $\tilde{A}_R^{(2)}(t)$ defined in Eq. (4.6) and Eq. (4.7), where the functions $a_q^{(2')}(t)$ are defined by Eq. (3.14). The spin-wave amplitudes $B_{n,i'',k}^{(1)}(t)$ and $B_{n,i'',k}^{(2')}(t)$ of the first and the second time interval are uniquely determined by the cavity-amplitudes $A_{n,i''}^{(1)}(t)$ and $A_{n,i''}^{(2')}(t)$ for both states " $i'' = 0, 1$ ", respectively. Following Eq. (2.11) we find

$$B_{n,i'',k}^{(1)}(t) = -g_k^* \int_{T_1}^t d\tau A_{n,i''}^{(1)}(\tau) e^{-[\gamma+i\Delta_k]\cdot(t-\tau)} \quad (\text{C.3})$$

$$B_{n,i'',k}^{(2')}(t) = B_{n,i'',k}^{(1)}(T_2) e^{-[\gamma+i\Delta_k]\cdot(t-T_2)} - g_k^* \int_{T_2}^t d\tau A_{n,i''}^{(2')}(\tau) e^{-[\gamma+i\Delta_k]\cdot(t-\tau)}, \quad (\text{C.4})$$

where g_k is the coupling strength of the k^{th} spin to the cavity-mode, respectively. In Sec. C.4 we show how to numerically evaluate g_k from the continuous spin density $\rho(\omega)$. To restore the cavity-amplitudes $A_{n,i''}^{(1)}(T_2)$ of both states " $i'' = 0, 1$ " we define the functional

$$\mathcal{M}_{n,i''} \left[\eta_S^{(2)}, \beta; \Delta T_S \right] = \left| \beta A_{n,i''}^{(1)}(T_2) - A_{n,i''}^{(2')}(T_2 + \Delta T_S) \right|, \quad (\text{C.5})$$

where we introduced the additional variational coefficient β . This parameter accounts for a potential global phase-shift and a total damping of the cavity-amplitude during the storage interval. To minimize the deviation of all N spin-wave amplitudes at the beginning T_2 and at the end of the storage interval $T_2 + \Delta T_S$, we define the least-mean-square functional

$$\mathcal{L}_{\chi^2} \left[\eta_S^{(2)}, \beta; \Delta T_S \right] = \sum_{i=0,1} \sum_{k=1}^N \left| \beta B_{n,i'',k}^{(1)}(T_2) - B_{n,i'',k}^{(2')}(T_2 + \Delta T_S) \right|^2 \rightarrow \min \quad (\text{C.6})$$

simultaneously for both basis states " 0 " and " 1 ". $B_{n,i'',k}^{(1)}(T_2)$ is an invariant function of the transition frequencies ω_k and is prepared by the respective writing pulse

$\eta_{i''}^{(1)}(t)$. The individual spin-waves $B_{i'',k}^{(2')}(T_2 + \Delta T_S)$ can be controlled by the storage pulse $\eta_S^{(2')}(t)$ to a certain degree. In order to avoid unphysical solutions of the storage pulse it is sufficient to define an upper boundary of its power by

$$\mathcal{M}_U \left[\eta_S^{(2')} \right] := \sum_{q=1}^{N_2} |\alpha_q^{(2,S)}|^2 < \mathcal{P}^{(2')}/2 \quad (\text{C.7})$$

according to [Eq. \(3.25\)](#). A potential trivial solution should also not be excluded. Further we define an upper and a lower boundary for the phase-parameter β

$$\beta_{\min} \leq |\beta| \leq \beta_{\max}. \quad (\text{C.8})$$

C.3 Functional Analysis in Delayed Readout Interval

However, minimizing [Eq. \(C.6\)](#) under the constraints given by [Eq. \(C.5\)](#), [Eq. \(C.7\)](#) and [Eq. \(C.8\)](#) proved to be numerically unstable. We therefore include the delayed readout section $[T_{3'}, T_{4'}]$ into the optimization procedure. At this point, we should be very careful with the parameter β . After the optimization procedure for the time-binned cavity-responses "0" and "1" the writing pulses $\eta_{0''}^{(1)}(t)$ and $\eta_{1''}^{(1)}(t)$ and the reading pulse $\eta_{\mathcal{R}}^{(2)}(t)$ exhibit a definite phase and power relation. In [Eq. \(C.5\)](#) and [Eq. \(C.6\)](#) we see that the cavity-amplitudes $A_{i''}^{(2')}(T_2 + \Delta T_S) = \beta A_{i''}^{(1)}(T_2)$ and the spin-wave amplitudes $B_{i'',k}^{(2')}(T_2 + \Delta T_S) = \beta B_{i'',k}^{(1)}(T_2)$ after the storage interval may reconstruct the initial states "i" = "0", "1" up to the complex valued factor β . Due to linearity we can think of $\beta A_{i''}^{(1)}(T_2)$ and $\beta B_{i'',k}^{(1)}(T_2)$ to be prepared with the scaled writing pulse $\beta \cdot \eta_{i''}^{(1)}(t)$. Thus the delayed readout pulse

$$\eta_{\mathcal{R}}^{(3')}(t) \equiv \beta \eta_{\mathcal{R}}^{(2)}(t - \Delta T_S) \quad (\text{C.9})$$

has to be rescaled accordingly. With a straight forward approach to [Sec. 3.1.3](#) and [Sec. A.1](#) the cavity-amplitude in the delayed readout interval takes the form

$$A_{i''}^{(3')}(t) = \tilde{A}_{i''}^{(3')}(t) + \underbrace{\sum_{q=1}^{N_2} \alpha_q^S \psi_q^{(3)}(t)}_{\tilde{A}_S^{(3')}(t)} + \tilde{A}_{\mathcal{R}}^{(3')}(t), \quad (\text{C.10})$$

where the undriven partial amplitudes $\tilde{A}_{i''}^{(3')}(t)$ continue the evolution of $\tilde{A}_{i''}^{(2')}(t)$ from the storage interval defined in [Eq. \(C.2\)](#), which, in turn, solely carries the information about the respective writing pulse $\eta_{i''}^{(1)}(t)$ from the first time interval.

In fact, $\tilde{A}_{i''}^{(3')}(t)$ is already solved by $\tilde{A}_{i''}^{(2)}(t)$ defined in Eq. (4.6) and Eq. (4.7) by expanding the time-divisions of the former readout interval $[T_2, T_3] \rightarrow [T_2, T_3 + \Delta T_S]$. The $N_{2'}$ functions $\psi_q^{(3)}(t)$ are described by the set of undriven Volterra integral equations defined by Eq. (3.13), continuing the evolution of $a_q^{(2)}(t)$ defined in Eq. (C.2), respectively. The common last term $\tilde{A}_{\mathcal{R}}^{(3')}(t) \equiv \beta \tilde{A}_{\mathcal{R}}^{(2)}(t - \Delta T_S)$ denotes the delayed readout part of the cavity-amplitudes defined by Eq. (4.6) and Eq. (4.7) scaled by β ; the time-argument needs to be shifted by ΔT_S according to the delayed readout. In order to address the quality of the restored cavity-amplitudes $A_{i''}^{(3')}(t)$ in the delayed functional interval $[T_{\mathcal{F}} + \Delta T_S, T'_{\mathcal{F}} + \Delta T_S]$ with respect to the original time-binned responses $A_{i''}^{(2)}(t)$, we introduce the fidelity objective functional

$$\mathcal{L}_{\text{Fid}}^{i''} \left[\eta_S^{(2')}, \beta; \Delta T_S \right] = 1 - \frac{\left| \int_{T_{\mathcal{F}} + \Delta T_S}^{T'_{\mathcal{F}} + \Delta T_S} dt A_{i''}^{(3')}(t) \cdot \left(\beta A_{i''}^{(2)}(t - \Delta T_S) \right)^* \right|}{\int_{T_{\mathcal{F}} + \Delta T_S}^{T'_{\mathcal{F}} + \Delta T_S} dt \left| \beta A_{i''}^{(2)}(t - \Delta T_S) \right|^2} \quad (\text{C.11})$$

to be minimized for both states " $i'' = 0$ ", " $i'' = 1$ ". The fidelity is insensitive to regions where the original time-binned cavity-amplitudes $A_{i''}^{(2)}(t)$ are negligible small. This is why we additionally minimize the overlap of the cavity-amplitudes in the delayed reading section

$$\mathcal{L}_{\text{Olap}} \left[\eta_S^{(2')}, \beta; \Delta T_S \right] = \left| \int_{T_{\mathcal{F}} + \Delta T_S}^{T'_{\mathcal{F}} + \Delta T_S} dt A_{i''=0}^{(3')}(t) \cdot \left(A_{i''=1}^{(3')}(t) \right)^* \right| \rightarrow \min. \quad (\text{C.12})$$

Eq. (C.11) and Eq. (C.12) can both be treated by the methods of Sec. B.4. The full functional for the storage procedure is composed of the quadratic deviation functional $\mathcal{L}_{\chi^2}[\eta_S^{(2')}, \beta; \Delta T_S]$ and the overlap functional $\mathcal{L}_{\text{Olap}}[\eta_S^{(2')}, \beta; \Delta T_S]$ constrained with $\mathcal{M}_{i''}[\eta_S^{(2')}, \beta; \Delta T_S]$, $\mathcal{M}_{\mathcal{U}}[\eta_S^{(2')}]$ and $\beta_{\min} \leq |\beta| \leq \beta_{\max}$. Similar to Sec. 4.1.1 the constrained functional of the storage procedure is minimized by numerical variation of the harmonic coefficients α_q^S of the storage pulse $\eta_S^{(2')}(t)$ and the scaling factor β , for which we used the *python* library *scipy.optimize*.

C.4 Coupling Strength of Individual Spins

In our numerical calculation we approximate all integrals with the trapezoid formula, hence our numerical "exact" solutions are restricted to small but finite frequency steps $\Delta\omega$. If we want to evaluate Eq. (C.3) or Eq. (C.4) we have to know, how the coupling coefficients g_k of the individual spins depend on the frequency grid $\Delta\omega$ and on the spin distribution function $\rho(\omega)$ defined by Eq. (2.9). We first

integrate $\rho(\omega)$ over one "numerical spin" of transition frequency ω_k in the interval $\omega_k \pm \Delta\omega/2$

$$\begin{aligned} \int_{\omega_k - \Delta\omega/2}^{\omega_k + \Delta\omega/2} d\omega \rho(\omega) &= \frac{1}{\Omega^2} \int_{\omega_k - \Delta\omega/2}^{\omega_k + \Delta\omega/2} d\omega \sum_{l=1}^N |g_l|^2 \delta(\omega - \omega_l) \\ &= \frac{1}{\Omega^2} \sum_{l=1}^N |g_l|^2 \delta_{lk} \\ \Delta\omega \cdot \rho(\omega_k) &\approx \frac{1}{\Omega^2} |g_k|^2, \end{aligned} \quad (\text{C.13})$$

which we approximate with $\Delta\omega \cdot \rho(\omega_k)$. Eq. (C.13) can be rewritten as $g_k = \Omega \sqrt{\Delta\omega \cdot \rho(\omega_k)}$ assuming a positive and read-valued coupling strength $|g_k| = g_k$. We then perform the summation over all spin degrees of freedom $\sum_{k=1}^N \Delta\omega \cdot \rho(\omega_k)$ and with $\Omega^2 = \sum_{k=1}^N |g_k|^2$ we find $\Delta\omega = (\sum_{k=1}^N \rho(\omega_k))^{-1}$ for the step-size and consequently for the coupling strength

$$g_k = \Omega \sqrt{\frac{\rho(\omega_k)}{\sum_{l=1}^N \rho(\omega_l)}}. \quad (\text{C.14})$$

C.5 Numerical Results of Storage Coefficients

Tbl. C.1 lists the harmonic coefficients of the optimized storage pulse $\eta_S^{(2')}(t)$ defined by Eq. (C.1), which is depicted in Fig. C.2.

α_1^S		-0.212 - 0.025 i		α_9^S		0.164 - 0.055 i
α_2^S		-0.088 + 0.049 i		α_{10}^S		-0.144 + 0.033 i
α_3^S		-0.646 + 0.139 i		α_{11}^S		0.133 - 0.045 i
α_4^S		-0.579 + 0.056 i		α_{12}^S		-0.116 + 0.028 i
α_5^S		0.270 - 0.108 i		α_{13}^S		0.112 - 0.038 i
α_6^S		-0.290 + 0.053 i		α_{14}^S		-0.098 + 0.024 i
α_7^S		0.211 - 0.070 i		α_{15}^S		0.097 - 0.033 i
α_8^S		-0.192 + 0.041 i		α_{16}^S		-0.084 + 0.021 i

Table C.1: Harmonic coefficients of the optimized storage pulse $\eta_S^{(2')}(t)$ defined by Eq. (C.1) for the restored time-binned cavity-responses depicted in Fig. C.2. The parameter $\beta = 0.33 + i0.025$.

Bibliography

- [1] Y. Kaluzny, P. Goy, M. Gross, J. M. Raimond, and S. Haroche, “Observation of self-induced rabi oscillations in two-level atoms excited inside a resonant cavity: The ringing regime of superradiance,” *Phys. Rev. Lett.*, vol. 51, pp. 1175–1178, Sep 1983.
- [2] F. You, J. Q.; Nori, “Superconducting circuits and quantum information,” *Physics Today*, vol. 58, 2005.
- [3] Z.-L. Xiang, S. Ashhab, J. Q. You, and F. Nori, “Hybrid quantum circuits: Superconducting circuits interacting with other quantum systems,” *Rev. Mod. Phys.*, vol. 85, pp. 623–653, Apr 2013.
- [4] Simon, C., Afzelius, M., Appel, J., Boyer de la Giroday, A., Dewhurst, S. J., Gisin, N., Hu, C. Y., Jelezko, F., Kröll, S., Müller, J. H., Nunn, J., Polzik, E. S., Rarity, J. G., De Riedmatten, H., Rosenfeld, W., Shields, A. J., Sköld, N., Stevenson, R. M., Thew, R., Walmsley, I. A., Weber, M. C., Weinfurter, H., Wrachtrup, J., and Young, R. J., “Quantum memories,” *Eur. Phys. J. D*, vol. 58, no. 1, pp. 1–22, 2010.
- [5] R. H. Dicke, “Coherence in spontaneous radiation processes,” *Phys. Rev.*, vol. 93, pp. 99–110, Jan 1954.
- [6] Y. Kubo, F. R. Ong, P. Bertet, D. Vion, V. Jacques, D. Zheng, A. Dréau, J.-F. Roch, A. Auffeves, F. Jelezko, J. Wrachtrup, M. F. Barthe, P. Bergonzo, and D. Esteve, “Strong coupling of a spin ensemble to a superconducting resonator,” *Phys. Rev. Lett.*, vol. 105, p. 140502, Sep 2010.
- [7] R. Amsüss, C. Koller, T. Nöbauer, S. Putz, S. Rotter, K. Sandner, S. Schneider, M. Schramböck, G. Steinhauser, H. Ritsch, J. Schmiedmayer, and J. Majer, “Cavity qed with magnetically coupled collective spin states,” *Phys. Rev. Lett.*, vol. 107, p. 060502, Aug 2011.
- [8] K. Sandner, H. Ritsch, R. Amsüss, C. Koller, T. Nöbauer, S. Putz, J. Schmiedmayer, and J. Majer, “Strong magnetic coupling of an inhomogeneous nitrogen-vacancy ensemble to a cavity,” *Phys. Rev. A*, vol. 85, p. 053806, May 2012.

-
- [9] J. H. Wesenberg, Z. Kurucz, and K. Mølmer, “Dynamics of the collective modes of an inhomogeneous spin ensemble in a cavity,” *Phys. Rev. A*, vol. 83, p. 023826, Feb 2011.
- [10] Z. Kurucz, J. H. Wesenberg, and K. Mølmer, “Spectroscopic properties of inhomogeneously broadened spin ensembles in a cavity,” *Phys. Rev. A*, vol. 83, p. 053852, May 2011.
- [11] X. Zhu, S. Saito, A. Kemp, K. Kakuyanagi, S.-i. Karimoto, H. Nakano, W. J. Munro, Y. Tokura, M. S. Everitt, K. Nemoto, M. Kasu, N. Mizuochi, and K. Semba, “Coherent coupling of a superconducting flux qubit to an electron spin ensemble in diamond,” *Nature*, vol. 478, pp. 221–224, Oct. 2011.
- [12] Y. Kubo, C. Grezes, A. Dewes, T. Umeda, J. Isoya, H. Sumiya, N. Morishita, H. Abe, S. Onoda, T. Ohshima, V. Jacques, A. Dréau, J.-F. Roch, I. Diniz, A. Auffèves, D. Vion, D. Esteve, and P. Bertet, “Hybrid quantum circuit with a superconducting qubit coupled to a spin ensemble,” *Phys. Rev. Lett.*, vol. 107, p. 220501, Nov 2011.
- [13] Y. Kubo, I. Diniz, A. Dewes, V. Jacques, A. Dréau, J.-F. Roch, A. Auffèves, D. Vion, D. Esteve, and P. Bertet, “Storage and retrieval of a microwave field in a spin ensemble,” *Phys. Rev. A*, vol. 85, p. 012333, Jan 2012.
- [14] Z.-L. Xiang, X.-Y. Lü, T.-F. Li, J. Q. You, and F. Nori, “Hybrid quantum circuit consisting of a superconducting flux qubit coupled to a spin ensemble and a transmission-line resonator,” *Phys. Rev. B*, vol. 87, p. 144516, Apr 2013.
- [15] D. G. England, K. A. G. Fisher, J.-P. W. MacLean, P. J. Bustard, R. Lausten, K. J. Resch, and B. J. Sussman, “Storage and retrieval of thz-bandwidth single photons using a room-temperature diamond quantum memory,” *Phys. Rev. Lett.*, vol. 114, p. 053602, Feb 2015.
- [16] V. M. Acosta, E. Bauch, M. P. Ledbetter, C. Santori, K.-M. C. Fu, P. E. Barclay, R. G. Beausoleil, H. Linget, J. F. Roch, F. Treussart, S. Chemerisov, W. Gawlik, and D. Budker, “Diamonds with a high density of nitrogen-vacancy centers for magnetometry applications,” *Phys. Rev. B*, vol. 80, p. 115202, Sep 2009.
- [17] I. Diniz, S. Portolan, R. Ferreira, J. M. Gérard, P. Bertet, and A. Auffèves, “Strongly coupling a cavity to inhomogeneous ensembles of emitters: Potential for long-lived solid-state quantum memories,” *Phys. Rev. A*, vol. 84, p. 063810, Dec 2011.
- [18] M. O. Scully, “Correlated spontaneous emission on the volga,” *Laser Physics*, vol. 17, 05 2007.

-
- [19] A. A. Svidzinsky, J.-T. Chang, and M. O. Scully, “Dynamical evolution of correlated spontaneous emission of a single photon from a uniformly excited cloud of n atoms,” *Phys. Rev. Lett.*, vol. 100, p. 160504, Apr 2008.
- [20] K. Henschel, J. Majer, J. Schmiedmayer, and H. Ritsch, “Cavity qed with an ultracold ensemble on a chip: Prospects for strong magnetic coupling at finite temperatures,” *Phys. Rev. A*, vol. 82, p. 033810, Sep 2010.
- [21] R. Houdré, R. P. Stanley, and M. Ilegems, “Vacuum-field rabi splitting in the presence of inhomogeneous broadening: Resolution of a homogeneous linewidth in an inhomogeneously broadened system,” *Phys. Rev. A*, vol. 53, pp. 2711–2715, Apr 1996.
- [22] M. Scully and M. Zubairy, *Quantum Optics*. Cambridge University Press, 1997.
- [23] S. Putz, D. O. Krimer, R. Amsuss, A. Valookaran, T. Nobauer, J. Schmiedmayer, S. Rotter, and J. Majer, “Protecting a spin ensemble against decoherence in the strong-coupling regime of cavity qed,” *Nat Phys*, vol. 10, pp. 720–724, Oct. 2014.
- [24] D. O. Krimer, S. Putz, J. Majer, and S. Rotter, “Non-markovian dynamics of a single-mode cavity strongly coupled to an inhomogeneously broadened spin ensemble,” *Phys. Rev. A*, vol. 90, p. 043852, Oct 2014.
- [25] D. O. Krimer, B. Hartl, and S. Rotter, “Hybrid quantum systems with collectively coupled spin states: Suppression of decoherence through spectral hole burning,” *Phys. Rev. Lett.*, vol. 115, p. 033601, Jul 2015.
- [26] D. D’Alessandro, *Introduction to Quantum Control and Dynamics*. Chapman & Hall/CRC Applied Mathematics & Nonlinear Science, CRC Press, 2007.
- [27] C. Brif, R. Chakrabarti, and H. Rabitz, “Control of quantum phenomena: past, present and future,” *New Journal of Physics*, vol. 12, no. 7, p. 075008, 2010.
- [28] B. Bartels and F. Mintert, “Smooth optimal control with floquet theory,” *Phys. Rev. A*, vol. 88, p. 052315, Nov 2013.
- [29] T. Nöbauer, A. Angerer, B. Bartels, M. Trupke, S. Rotter, J. Schmiedmayer, F. Mintert, and J. Majer, “Smooth optimal quantum control for robust solid-state spin magnetometry,” *Phys. Rev. Lett.*, vol. 115, p. 190801, Nov 2015.
- [30] H. Primakoff and T. Holstein, “Many-body interactions in atomic and nuclear systems,” *Phys. Rev.*, vol. 55, pp. 1218–1234, Jun 1939.

-
- [31] O. Romero-Isart and J. J. García-Ripoll, “Quantum ratchets for quantum communication with optical superlattices,” *Physical Review A*, vol. 76, 11 2007.
- [32] P. Doria, T. Calarco, and S. Montangero, “Optimal control technique for many-body quantum dynamics,” *Physical Review Letters*, vol. 106, 5 2011.
- [33] I. Novikova, N. B. Phillips, and A. V. Gorshkov, “Optimal light storage with full pulse-shape control,” *Phys. Rev. A*, vol. 78, p. 021802, Aug 2008.
- [34] J. Brendel, N. Gisin, W. Tittel, and H. Zbinden, “Pulsed energy-time entangled twin-photon source for quantum communication,” *Phys. Rev. Lett.*, vol. 82, pp. 2594–2597, Mar 1999.
- [35] M. U. Staudt, S. R. Hastings-Simon, M. Nilsson, M. Afzelius, V. Scarani, R. Ricken, H. Suche, W. Sohler, W. Tittel, and N. Gisin, “Fidelity of an optical memory based on stimulated photon echoes,” *Phys. Rev. Lett.*, vol. 98, p. 113601, Mar 2007.
- [36] H. de Riedmatten, M. Afzelius, M. U. Staudt, C. Simon, and N. Gisin, “A solid-state light-matter interface at the single-photon level,” *Nature*, vol. 456, pp. 773–777, Dec. 2008.
- [37] H. Jayakumar, A. Predojević, T. Kauten, T. Huber, G. S. Solomon, and G. Weihs, “Time-bin entangled photons from a quantum dot,” *Nat Commun*, vol. 5, pp. –, June 2014.
- [38] P. C. Humphreys, B. J. Metcalf, J. B. Spring, M. Moore, X.-M. Jin, M. Barbieri, W. S. Kolthammer, and I. A. Walmsley, “Linear optical quantum computing in a single spatial mode,” *Phys. Rev. Lett.*, vol. 111, p. 150501, Oct 2013.
- [39] N. Gisin, S. A. Moiseev, and C. Simon, “Storage and retrieval of time-bin qubits with photon-echo-based quantum memories,” *Phys. Rev. A*, vol. 76, p. 014302, Jul 2007.
- [40] M. A. Nielsen and I. L. Chuang, *Quantum Computation and Quantum Information: 10th Anniversary Edition*. New York, NY, USA: Cambridge University Press, 10th ed., 2011.
- [41] C. W. Gardiner and M. J. Collett, “Input and output in damped quantum systems: Quantum stochastic differential equations and the master equation,” *Phys. Rev. A*, vol. 31, pp. 3761–3774, Jun 1985.
- [42] M. Tavis and F. W. Cummings, “Exact solution for an n -molecule—radiation-field hamiltonian,” *Phys. Rev.*, vol. 170, pp. 379–384, Jun 1968.

-
- [43] B. M. Garraway, “The dicke model in quantum optics: Dicke model revisited,” *Philosophical Transactions Mathematical Physical & Engineering Sciences*, vol. 369, 2011.
- [44] C. Gardiner, *Handbook of stochastic methods for physics, chemistry, and the natural sciences*. Springer series in synergetics, Springer-Verlag, 1985.
- [45] C. W. Gardiner, M. J. Collett, and A. S. Parkins, “Input and output in damped quantum systems. ii. methods in non-white-noise situations and application to inhibition of atomic phase decays,” *J. Opt. Soc. Am. B*, vol. 4, pp. 1683–1699, Oct 1987.
- [46] L. Childress, M. V. Gurudev Dutt, J. M. Taylor, A. S. Zibrov, F. Jelezko, J. Wrachtrup, P. R. Hemmer, and M. D. Lukin, “Coherent dynamics of coupled electron and nuclear spin qubits in diamond,” *Science*, vol. 314, no. 5797, pp. 281–285, 2006.
- [47] B. Kraus, W. Tittel, N. Gisin, M. Nilsson, S. Kröll, and J. I. Cirac, “Quantum memory for nonstationary light fields based on controlled reversible inhomogeneous broadening,” *Phys. Rev. A*, vol. 73, p. 020302, Feb 2006.
- [48] N. Sangouard, C. Simon, H. de Riedmatten, and N. Gisin, “Quantum repeaters based on atomic ensembles and linear optics,” *Rev. Mod. Phys.*, vol. 83, pp. 33–80, Mar 2011.
- [49] N. Gisin, G. Ribordy, W. Tittel, and H. Zbinden, “Quantum cryptography,” *Rev. Mod. Phys.*, vol. 74, pp. 145–195, Mar 2002.
- [50] A. V. Gorshkov, A. André, M. Fleischhauer, A. S. Sørensen, and M. D. Lukin, “Universal approach to optimal photon storage in atomic media,” *Phys. Rev. Lett.*, vol. 98, p. 123601, Mar 2007.
- [51] N. B. Phillips, A. V. Gorshkov, and I. Novikova, “Optimal light storage in atomic vapor,” *Phys. Rev. A*, vol. 78, p. 023801, Aug 2008.
- [52] U. Andersen, G. Leuchs, and C. Silberhorn, “Continuous-variable quantum information processing,” *Laser & Photonics Reviews*, vol. 4, no. 3, pp. 337–354, 2010.
- [53] S. Putz, A. Angerer, D. O. Krimer, R. Glattauer, W. J. Munro, S. Rotter, J. Schmiedmayer, and J. Majer, “Engineering long-lived collective dark states in spin ensembles,” 2015.